

TEMPORAL AND SPATIAL TWO-MEDIUM
VOID DISTRIBUTIONS

by

GARY DANIEL ZAKAIB, B.Sc.

A thesis
submitted to the Faculty of Graduate Studies
in partial fulfillment of the requirements
for the degree of Master of Engineering

McMaster University
Hamilton, Ontario, Canada
April, 1976

MASTER OF ENGINEERING (1976)
(Chemical Engineering)

McMASTER UNIVERSITY,
HAMILTON, ONTARIO.

TITLE: Temporal and Spatial Two-Medium Void Distributions
by Radiation Diagnostics

AUTHOR: Gary D. Zakaib, B.Sc. (Queen's University, Kingston
Ontario)

SUPERVISORS: Dr. J. Vlachopoulos and Dr. A. A. Harms

NO. OF PAGES: i- x, 1-124

SCOPE AND CONTENT:

This thesis deals with two aspects of discrete time interval neutron diagnostics for application to two-phase systems. Part I resulted from an investigation on the effect of gating period on statistical distributions arising from discrete sampling period measurements of idealized two-phase situations; this portion of the work also afforded the opportunity to become accustomed to the procedures and problems associated with void fraction studies employing penetrating radiation. Part II receives a slightly larger emphasis and deals with the application of contemporary computational methods to the reconstruction in two dimensions of the time-averaged void distribution of a dual density system. Each part is accompanied by its own references, notation, and appendices. They are related as briefly described in Sec. II. 7.2 . Details of these parts now follow under separate head-

ABSTRACT

Two specific aspects of penetrating radiation diagnostics for application to two-phase flow systems were investigated. In Part I, discrete time interval attenuation measurements of a neutron beam from a research reactor were used to study the effect of the gating (measurement) period on the resulting void probability density distributions. Three idealized two-phase situations were investigated - discrete bubble, slug, and annular flow, for 0.01-10.0 s gating periods. The slug flow condition was readily characterized by a dual maxima PDD for gating intervals below the dominant slug period. In all cases the PDD variance increased with decreasing gating periods and was found to be of use for trend description and regime discrimination.

Part II endeavours to reconstruct in two dimensions, the time-averaged void distribution of a dual density system from radiation attenuation measurements. The procedure employed made use of three contemporary algebraic reconstruction methods. Projection data was obtained from a digitized computer model in the first set of tests and later from traverses of a neutron beam across a voided lucite model. With a fixed, large beam size, decoupling of overlapped measurements was needed to permit resolution of fine detail. Extension to the dynamic two-phase flow situation was considered and it was shown that the void variance within a subdivided measurement interval can provide an estimate of the dynamic void bias effect.

Keywords: two-phase flow, radiation diagnostics, void distributions, 2-D algebraic reconstruction

ACKNOWLEDGEMENTS

The work described herein was co-supervised by Dr. J. Vlachopoulos of the Department of Chemical Engineering and Dr. A.A. Harms of the Department of Engineering Physics. The research was supported by operating grants from the National Research Council of Canada. The author is grateful to McMaster University for financial assistance.

Abstract	iii
Acknowledgements	iv
Contents	v
Figures.	vii
Tables	ix
Glossary	x

PART I : The Effect of Gating Period on Neutron Diagnosis of Void Distributions

I.1	INTRODUCTION.	2
I.2	BACKGROUND	
I.2.1	Motivation.	5
I.2.2	Literature Review	5
I.3	APPARATUS	11
I.4	PROCEDURE	14
I.5	RESULTS	16
I.6	DISCUSSION.	24
I.7	CONCLUSION AND RECOMMENDATIONS.	30
	NOTATION.	32
	LITERATURE CITATIONS.	33
	APPENDICES	
A.1	Computer program description.	36
A.2	Tabular summary of statistics for principal test conditions	38
A.3	Flow patterns in vertical two-phase flow.	39

PART II : Algebraic Reconstruction of Two-Dimensional Void Distributions from Radiation Attenuation Measurements

II.1	INTRODUCTION.	41
II.2	BACKGROUND	
II.2.1	Literature review	44
II.2.2	Features.	47
II.2.3	Limitations	48
II.3	THEORY.	50
II.4	APPARATUS	63
II.5	PROCEDURES.	64
II.6	RESULTS	71
II.7	DISCUSSION	
II.7.1	General	89
II.7.2	Extension to the dynamic case	94
II.8	CONCLUSION.	99
II.9	RECOMMENDATIONS	101
	NOTATION.	103
	LITERATURE CITATIONS.	105
	APPENDICES	
A.1	Test model and positioning stand for real projection data	108
A.2	Description of program listings	109
A.3	Main program listings	114
A.4	Additional program segments	121
A.5	Subroutines	123

FIGURES

Part I

I.1	Void and transmittance histograms for slug flow....	6
I.2	Vapour structures in saturated nucleate boiling....	6
I.3	Physical arrangement for discrete bubble tests.....	12
I.4	Void histograms for discrete bubbling.....	17
I.5	Void histograms for small slug flow.....	19
I.6	Void histogram for large slug flow.....	20
I.7	Void histogram for annular flow condition.....	20
I.8	Comparison of transmission ratio and void fraction distributions under slug flow conditions.....	21
I.9	Plot of PDD variance against gating period for various flow conditions	23
I.10	Frequency diagram of successive count rates for large slug flow	26
A.3	Flow patterns in vertical two-phase flow.....	39

Part II

II.1	Reconstruction matrix of coordinate axes.....	51
II.2	Basis of routine SMOOTH	51
II.3	Two-phase model for pseudo-projection data in digitized form	65
II.4	Sketch of REAL model positioning mechanism when source and detector are immobile	66
II.5	Ten gray-level overprinting characters	68
II.6	Two-phase model for pseudo-projection data.....	69
II.7	Discrepancy parameter vs. number of iterations for various algorithms and conditions	72
II.8	ART2 reconstruction in digitized form and via PIX..	73

II.9	SIRT reconstruction in digitized form	74
II.10	LESQ reconstruction in digitized form	75
II.11	Average and variance of discrepancy between reconstruction region of size $N \times N$ and digitized model.	78
II.12	Effect of SMOOTH and FORCE on a discrepancy- variance plot	79
II.13	Effect of SMOOTH on a coarse increment SIRT reconstruction.	81
II.14	Effect of FORCE on reconstruction of Fig. 13A . . .	81
II.15	ART2 reconstruction of REAL model	83
II.16	SIRT reconstruction of REAL model	84
II.17	ART2 reconstruction of REAL model using trans- mitted count rate differencing to determine ray sums.	85
II.18	ART2 reconstruction of REAL model using ray sums calculated by back substitution from different directions.	86
II.19	ART2 reconstruction of REAL model with smaller beam increment and gating period.	88
A.1	Photographs of REAL test model and positioning stand	108

TABLES

Part I

A.2	Tabular summary of statistics for principal test conditions.	38
-----	--	----

Part II

II.1	Efficiency comparison of major algorithms tested. . .	77
------	---	----

GLOSSARY

Epithermal neutrons -- neutrons having an energy in the range immediately above the thermal range, roughly between 0.2 and 100 electron volts.

Gating period -- the preset time interval over which the emerging radiation beam is sampled and the counts are compiled.

Maxwellian distribution -- a function giving the number of neutrons in thermal equilibrium whose velocities lie within a given infinitesimal range of values, assuming that the neutrons obey classical mechanics and do not interact.

Proportional detector -- a radiation counter tube operated at voltages high enough to produce ionization by collision and adjusted so the total ionization per count is proportional to the ionization produced by the initial ionizing event.

Radiation diagnostics -- methods and analytical interpretation involved in identifying two-phase flow conditions from radiation attenuation measurements.

Reactivity -- a parameter giving the deviation from criticality of a nuclear chain reacting medium such that positive values correspond to a supercritical state and negative values to a subcritical state.

Subchannel code -- for thermohydraulic analyses in rod bundle geometries, these computer codes were developed to include the effects which determine cross-flow and turbulent mixing between subchannels that further complicates prediction of local coolant conditions. Mass, momentum, and energy are considered transported across imaginary interfaces separating adjacent subchannels. The result is a prediction of subchannel flow and enthalpy at each axial channel position.

Two-phase flow -- movement of two phases (commonly liquid and gas) through a pipe or closed conduit. The thermohydraulic connotation generally refers to the motion of steam and water in a boiling channel.

PART I

THE EFFECT OF GATING PERIOD ON
NEUTRON DIAGNOSIS OF
VOID DISTRIBUTIONS

I.1 INTRODUCTION

Boiling heat transfer is perhaps one of the most effective means of energy transfer known to man, with observed energy fluxes as high as that on the surface of the sun. The resultant applications, such as those found in aerospace technology, chemical processing units, and nuclear reactors, has stimulated wide-spread interest in two-phase phenomena. Specifically with regard to nuclear reactors, the economic advantage of higher specific power output is forcing a trend toward permitting boiling in the coolant channel as in some present CANDU designs.

When vapour is generated in a liquid filled system, the phases partition themselves into a number of possible geometric arrangements or regimes. Typical of these flow regimes are three idealized cases as illustrated in the figures of Appendix A.3: 1) bubble flow where discrete vapour bubbles are homogeneously distributed in a liquid continuum, 2) slug flow where the two phases segregate into liquid slugs and elongated vapour bubbles and 3) annular flow where a continuous gas core has forced the liquid phase into a thin film on the channel walls. Forms of these three idealized regimes are subject to investigation in this work.

In discussions of two-phase systems, the single parameter most commonly encountered is the void fraction - the relative volume of vapour and liquid phases at a given position

in the system. This important engineering parameter appears in correlations of heat transfer, boiling hydrodynamics, and flow regimes. In addition to thermal studies, the time-varying void distribution is of fundamental importance in nuclear safety and control studies. In design applications, the void fraction is used to calculate the mean density which in turn is needed for estimating frictional, accelerational, and hydrostatic pressure drops in two-phase systems.

Many methods have been proposed to study void fraction. However, visual techniques and fragile probes become inadequate at the pressures and temperatures appropriate to many systems of interest. In this work we are interested in an attenuated beam of penetrating radiation (X-rays, gamma rays, electrons or neutrons) as a diagnostic tool. These methods avoid contamination of the medium and disruption of the flow regime under study. Specifically, neutrons from a reactor beamport were employed here because their attenuation characteristics permit good void resolution for the system size of interest.

Previous work employing neutron attenuation has concentrated on obtaining an accurate estimate of the time-averaged void fraction (Harms et al, 1971). However, as attested by any two-phase experimentalist, the void fluctuations cannot be ignored. In addition, it has been found (Hancox et al, 1972) that these temporal variations can induce a significant bias in the void measurement. To reduce this measurement bias, Hancox et al (1972) proposed a discrete sampling period technique and suggested that the gating interval be "... much smaller⁴ than the

dominant void fluctuation period". The fundamental purposes of this work therefore, examine the consequences of this technique and are two-fold: 1) to employ statistical distributions resulting from discrete time interval neutron diagnostics to distinguish two-phase regimes (bubble, slug, or annular) and 2) to investigate the effect of the gating (measurement) period on these distributions for the different regimes under study. Also the concept of a characteristic period of the fluctuation is introduced and discussed.

Following a discussion of the background and pertinent literature in this area, the experimental apparatus and computational procedures are described. Results of experimental data, primarily in the form of figures, are presented and discussed. Principal conclusions are summarized and a description of the program used to analyse transmission measurements is included in the appendices.

Part I will then have considered the time-varying nature of the voids by means of statistical distributions. With the temporal effects thus examined, Part II of the thesis then goes on to consider the importance of the spatial distribution of the voids within a reactor channel and shows how radiation diagnostics may be applied for this purpose.

I.2 BACKGROUND

I.2.1 Motivation

While investigating the transmission error due to the inherent void fluctuations, Hancox et al (1972) found that the measured value of the void fraction, hereafter to be represented by α , depended not only on flow regime but also on the gating period used in the "churn" flow regime. Figure I.1 reproduces their results for slug flow. We note that the distribution shape is dependent on the gating period. It was the desire to elucidate this effect that motivated this portion of the work. A survey of the relevant literature in this area is presented in Part B of the literature review.

Initially, however, it was sought to employ discrete-time interval technique to pool boiling which itself exhibits "regimes". Using neutron diagnostics, it is often difficult to obtain good statistics for small measurement periods. Therefore, to allow a reasonable gating period, ΔT , the preferred situation occurs when the liquid velocity is zero - in essence, a batch two-phase system. This then suggests pool boiling as a convenient starting point. Aspects of interest for this application will be outlined in Part A of the literature review below. Subsequently, extension to the slug and annular flow situations will be made.

I.2.2 Literature Review

Part A Duke and Schrock (1961) were among the earliest to

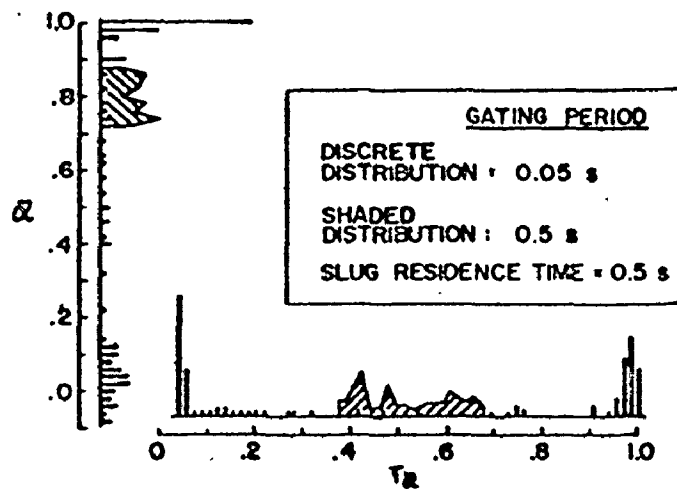


Figure I.1 Void and transmittance histograms for slug flow ($\bar{\alpha} = 0.5$). From Hancox, et al (1972). Two distributions at different gating periods are represented on each scale. One distribution is indicated by a set of single lines while the other uses shaded areas.

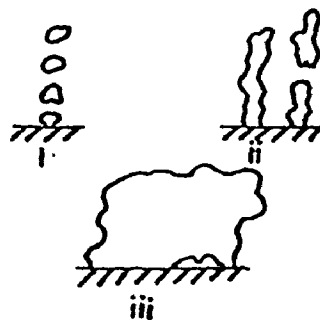


Figure I.2 Vapour structures in saturated nucleate boiling.

- i) Discrete bubbling
- ii) Vapour columns
- iii) Vapour mushroom

measure void volumes in nucleate pool boiling, employing a bellows dilatometer as well as photography. Their principal conclusion was that void volume increased with heat flux while it decreased with increases in both pressure and subcooling. In a photographic study, Gaertner (1965) described three or four heat transfer regions in saturated nucleate boiling, each with characteristic vapour structures. The three principal structures are sketched in Figure I.2 and the obvious differences suggest the possibility of unique void distributions if discrete time neutron diagnostics were applied to such systems. Rallis and Jawurek (1964) and Cole (1967) show how the product of the mean bubble frequency and mean bubble volume at departure enter into many analyses of nucleate boiling and also into the expression for latent heat transport. In absence of simpler methods, the possibility of applying neutron diagnostics in determining these quantities merits consideration.

Zuber (1963) examined both the fluid dynamic and heat transfer processes in nucleate pool boiling from a horizontal surface. The fluid dynamic problem was analysed by first considering flow regimes induced by single bubbles. Also described were previous investigations of both characteristic bubble diameters and frequencies of bubble emission by statistical distribution. Flow regimes of vapour removal from a single nucleating centre were found to change from isolated bubbles at low vapour rates to swirling vapour columns and patches. These regimes were considered to be analogous to the formation of gas bubbles at orifices. This assertion was

employed in the first set of tests as are outlined in Section I.4 . Zuber also presented equations giving the vapour volumetric fraction as a function of quantities reported in the literature and later employed them in the formulation of the heat transfer problem.

Part B We return now to the theory and background of radiation diagnostics. To determine the void fraction from transmission measurements, Harms et al (1971) suggest an iterative solution of

$$T\alpha = T_0 B(x(1-\alpha)) e^{-\mu x(1-\alpha)} \quad (I.1)$$

for the void fraction, α , where T_0 is the transmitted count rate in the empty channel ($\alpha=1$), $T\alpha$ is the measured count rate of the system, x is the overall thickness of the attenuation medium, and μ is a linear attenuation parameter. The symbol B is a predetermined functional representation for the build-up factor which becomes particularly important for relatively thick medium measurements. With this method, voids in the range .03-.7 were determined to within $\pm 6.5\%$ in "one-shot" measurements. Each void fraction obtained from Eq. I.1 is assumed constant over the gating interval ΔT . For N such measurements, with N large, the standard definitions for the mean and sample variance of the resulting void distributions are

$$\bar{\alpha} = \frac{1}{N} \sum_{n=1}^N \alpha_n \quad , \quad (I.2)$$

and

$$\sigma_{\alpha}^2 = \frac{1}{N-1} \sum_{n=1}^N (\alpha_n - \bar{\alpha})^2 \quad (I.3)$$

However, as a representation of void dynamics, these expressions may involve errors due to the variation of α over ΔT and due to additional effects of source fluctuations at the time T_0 and T_{α} were measured. These points are discussed further in Sections I.7 and II.7.2. In a relevant analytical study, Barrett (1974) in fact examines the discretized time interval method with respect to the magnitude of the systematic error introduced by the finiteness of the gating period in the interpretation of $\bar{\alpha}$ and σ_{α}^2 . The resulting expressions require large N and $\overline{T\alpha_n} > 1$ and care must also be taken so that ΔT is not reduced such that the condition $1/(\overline{T\alpha_n})^2 \ll 1$, no longer holds. Barrett also concludes that the static void assumption will be most in error under the following conditions: a) for $\lambda(=\mu x)$ large, b) when α is not constant over ΔT , c) when the vertical flow speed is not small, and d) when the void changes over the whole channel cross-section, as with slug flow. For small bubbles, fine sprays and annular flows with low ripple noise the error can be ignored. The compromise between counting errors and systematic errors is also discussed.

Two sample void distributions for bubble and slug flow are presented by Hancox and Harms (1971) who conclude that the distribution of the α_n provides a unique characterization of the voided flow conditions. They suggested one immediate use

is to provide upper and lower bounds of the void fraction for reactor response evaluations. Additional work on the dynamic bias effect was done by Harms and Laratta (1973) who studied specific void variations, $\alpha(t)$ and Harms & Forrest (1971) who obtained more general analytic results. Younis et al (1973) discussed the bias due to source fluctuations which can become important for low void measurements and highly attenuated beams. In this study the idea of utilizing statistical distributions to describe the dynamic behaviour of two-phase systems is employed. This approach is in line with the current trend in the two-phase literature. For example, Chu & Dukler (1975), examine comprehensively annular flow films by describing probability and spectral density functions of wavy films.

In experiments similar to this work, Jones & Zuber (1974 and 1975) employed an X-ray photometer to obtain void probability density functions (PDF) in a fluctuating air-water system. They felt that the PDF method represents a uniquely objective method for flow pattern discrimination. Many of their observations were in fact independently confirmed in this study. Among them is the following definition:

"Slug flow is that localized condition characterized by the appearance of two separate and statistically significant localized maxima in the PDF . . ."

Other information available from the PDF data are film thicknesses, void fraction in slugs, and slug and bubble residence time fractions. However, the effect of gating period on the probability density distributions was not considered and it is this area that is developed in this study.

I.3 APPARATUS

The principal pieces of apparatus employed to fulfill the objectives of this portion of the work are the following:

A cast acrylic container with aluminum "neutron windows" built in the side to perform the first series of tests on discrete bubbling. Internal dimensions - 18 cm deep x 7 cm long x 1.3 cm wide. The size ($x = 1.40$ cm at the neutron windows) was chosen to permit adequate statistics under low void conditions while not interfering with the rising bubble stream. Figure I.3 is a sketch of the physical setup which was used.

Stainless steel capillary orifice, 3.2 mm O.D., 1.3 mm I.D. at the opening. Flowrator flowmeter and needle valve to measure flowrates in the range 0.2 - 32.0 cc/s.

Commercial three-speed tape recorder to measure bubble frequencies acoustically. This was accomplished by calibrating the recorder against a time signal and using the noise of the bubbles erupting from the orifice to measure the frequency. A stroboscope was also used for verification but was found to be less accurate.

A vertical, clear lucite, two-phase loop, 0.75 inches (1.8 cm) I.D., with thin stainless steel test sections for the neutron beam. This apparatus was used previously for transient void measurements in the air-water system. It was employed

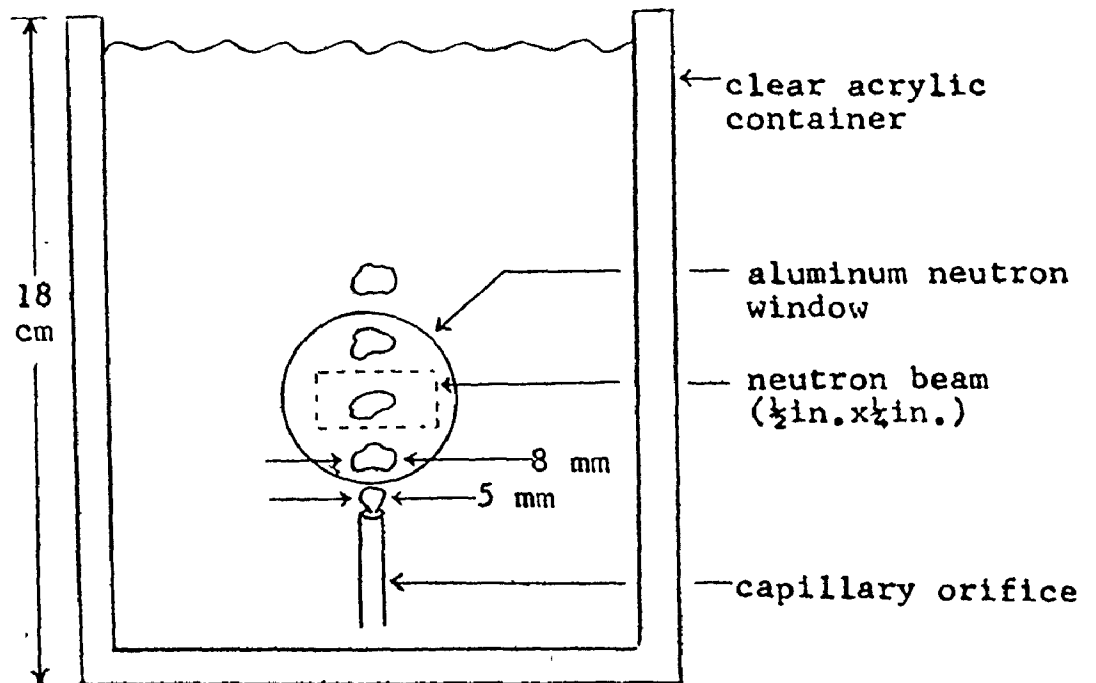


Figure I.3 Sketch of physical arrangement
for discrete bubble tests.

here for the Series 2 and 3 test runs under slug and annular conditions.

Neutron counting apparatus - standard 2.56 cm diameter BF_3 proportional detector encased in a cadmium sleeve with a 0.5 in. x 0.25 in. (1.27 cm x 0.64 cm) opening, digital rate-meter, and magnetic tape interface. Gating periods are available in the range 10^{-3} to 10^{+3} seconds.

The neutron source was a beamport of the McMaster University 2 MW(t) swimming pool type nuclear reactor. Opening size and shape matched that of the cadmium sleeve. The unattenuated beam gave a count rate of approximately 3×10^5 c/s with the above configuration.

I.4 PROCEDURES

This section describes the steps taken during the course of the investigation. The first two parts outline initial considerations and computational procedures. The third part then summarizes experimental procedures and test conditions of important runs.

Initial steps involved obtaining experience in the use of the detection hardware and two-phase loop. In addition, the neutronic properties of several fluids were investigated for possible use. Although water was finally chosen for all runs, freon-113 ($\text{CCl}_2\text{F}-\text{CClF}_2$) was also used in pre-run tests to determine the linear attenuation parameter and build-up data. For this purpose, Harms et al (1971) was followed

$$\mu = \lim_{x \rightarrow 0} \frac{\ln(T_0/T_x)}{x} , \quad (I.4)$$

and

$$B(x) = (T_x/T_0) e^{\mu x} , \quad (I.5)$$

where T_x represents the transmitted count rate for a medium of thickness x . Aluminum containers of known width were available for this purpose.

A computer program was constructed to analyse the neutron transmission data. Briefly, the transmission ratio

statistics are first compiled by a library routine and then the data is plotted in the form of a histogram. Eq. I.1 is employed next to compute void fractions which are also compiled and plotted. A more detailed description of the program is provided in Appendix A.1.

Although a large number of tests were performed under a wide variety of conditions, the runs may be divided into three broad classifications. Emphasis will be placed on results of runs designed to show specific trends under identical flow conditions. i) The Discrete Bubble runs were performed by injecting a metered air flow through a single orifice in the acrylic container. The arrangement is illustrated in Fig. I.3 which also describes typical bubble diameters encountered. ii) The simulated Slug flow conditions were created by injecting air into a static column of liquid in the two-phase loop. The result was classical dome-type flows. Conditions with both small and large bubbles (~ 10 -20 cm range) were investigated. iii) In the third category, Annular flow conditions required maximum vapour flow rates to the two-phase loop. The liquid flowrate was minimal; only enough to maintain a continuous liquid film on the tube wall. The characteristic void period was measured acoustically in the discrete bubble regime and by a calibrated stopwatch in the slug regime.

I.5 RESULTS

In the pre-run tests the experimentally determined linear attenuation parameter for water with this apparatus and neutron spectrum was found to be 4.83 cm^{-1} . From the few measurements made with freon-113, the parameter was found to be 1.35 cm^{-1} . Freon was not employed in future runs however because its high volatility required a closed system. Results of the least squares fit of the build-up data may be found in Appendix A.1. The acoustic method for bubble frequency determination, as described in Sec. I.3, was found to be very satisfactory. Repeatability of these results was consistently less than 9% over the entire region of interest and this was largely due to the variability of the bubble emission. Although the variation in the slug period from bubble to bubble was large, the measured average frequency varied to within about $\pm 8\%$.

It was found that the results for this portion of the work could be most readily interpreted in the form of void histograms, both the transmittance ratio and void statistics of all important runs are again summarized in Table A.2. In general it was found that the statistics became meaningless if the gating period was so small that zeros and other small digit numbers appear in the counting data. Also, better resolution of the PDD's was obtained if the beam width perpendicular to the flow direction was small.

The first set of histograms in Fig. I.4 describes the

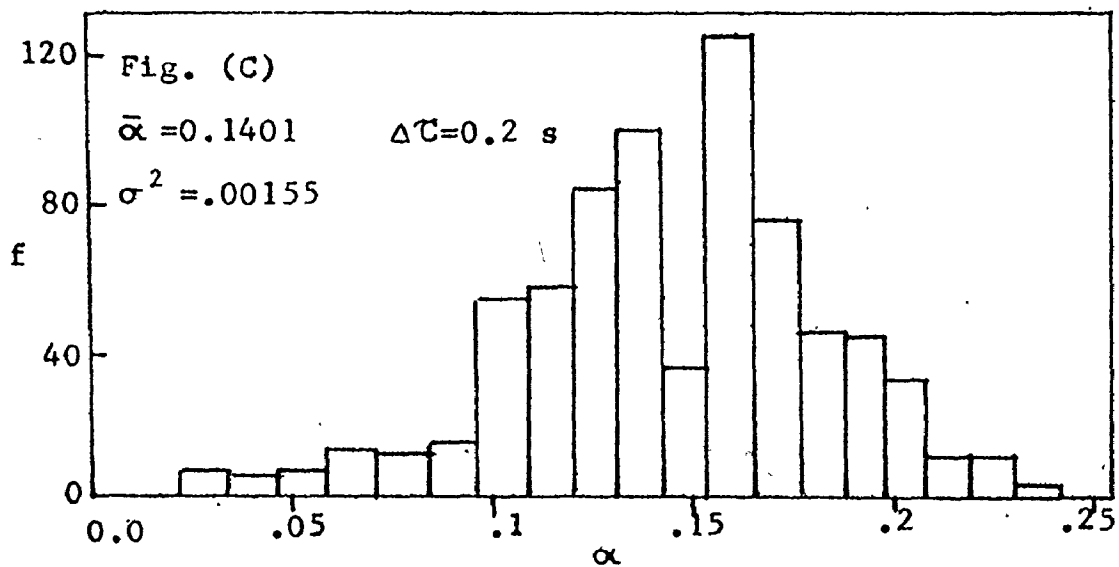
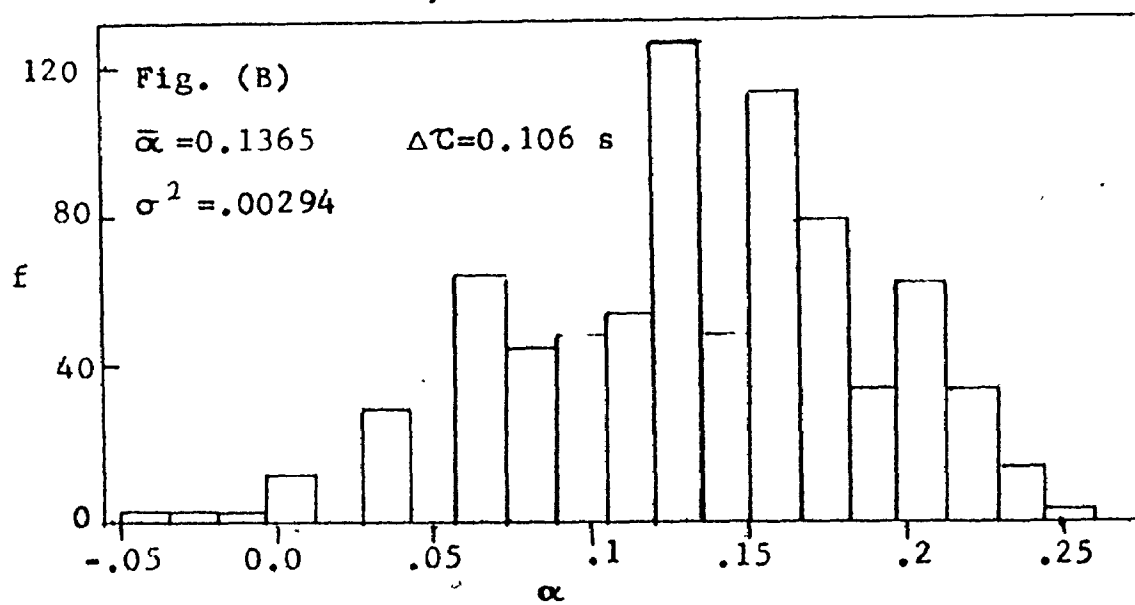
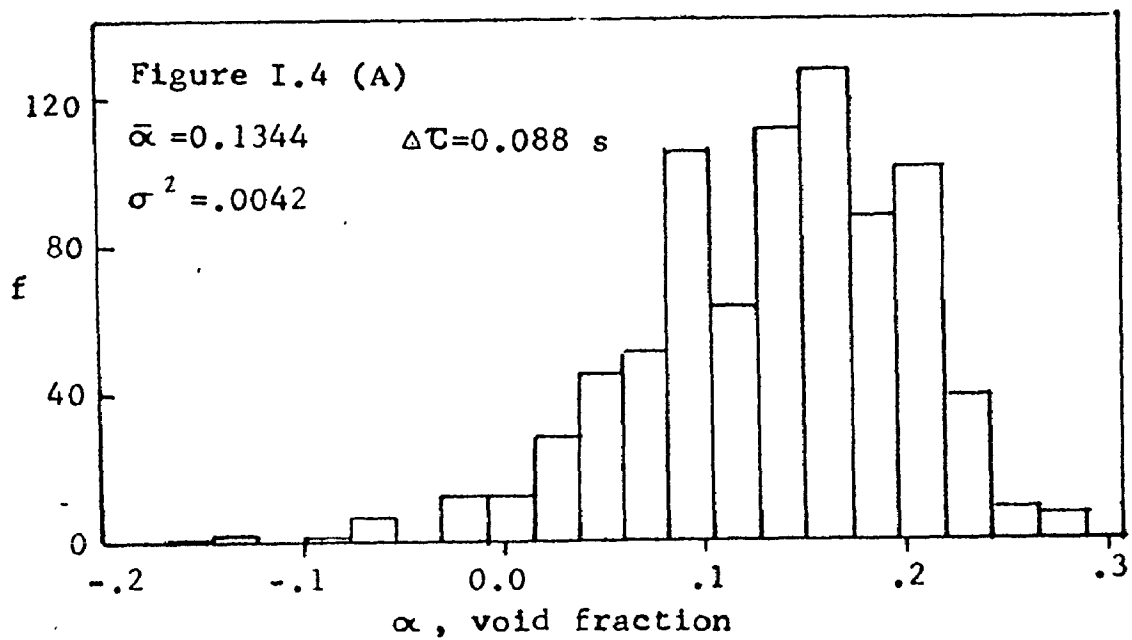


Fig. I.4 A,B,C Void histograms for discrete bubbling ($R_V = .105$ s)
Vapour flowrate = 1.21 cc/s

void PDD for the discrete bubble regime. The gating period in Fig. I.4A is slightly less than the void period, in Fig. I.4B about the same, and in Fig. I.4C slightly greater. All three distributions appear similar in shape; however, a noticeable change in the range of the abscissa, α , is to be noted. This effect is quantified by the variance of the distribution, σ^2 . Average void fractions were found to increase slightly with increased gating period. Fig. I.5 shows three histograms for the small slug flow conditions. General observations are identical with discrete bubble regime except that a distinct change in the shape of the distribution was noted and the change in the variance is even more marked. A bimodal distribution is distinct at the lower ΔT , changing to a single mode distribution when ΔT exceeds the dominant slug period. Even more interesting is Fig. I.6 which represents large slug flow with the gating period significantly less than the void period. Two separate distributions are clearly visible centered about maxima at low and high void fractions. The wide range of void readings, from -0.6 to +0.9, is noteworthy. Lastly, the annular flow condition is represented in Fig. I.7. All annular distributions, regardless of ΔT , exhibited the same tight, negatively skewed distribution.

Figure I.8 is presented to permit a quick comparison between the transmission ratio and void distributions. These distributions are related through Eq. I.1 where $TR = T\alpha/T_0$. Slug flow conditions were presented because of the variety of distribution types present. In comparison, the bubble flow

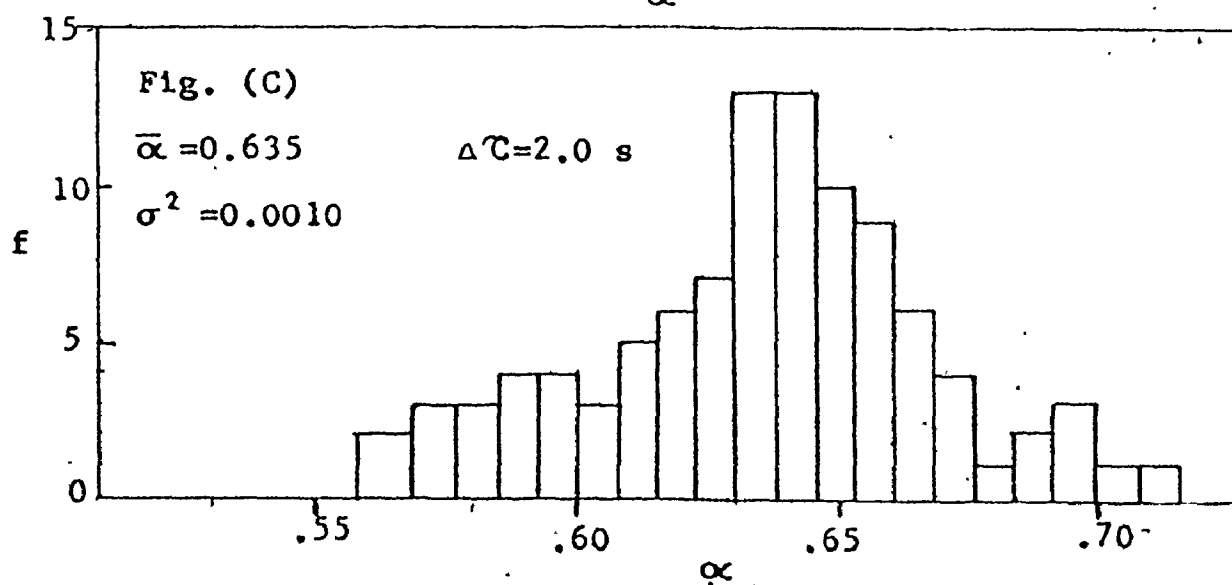
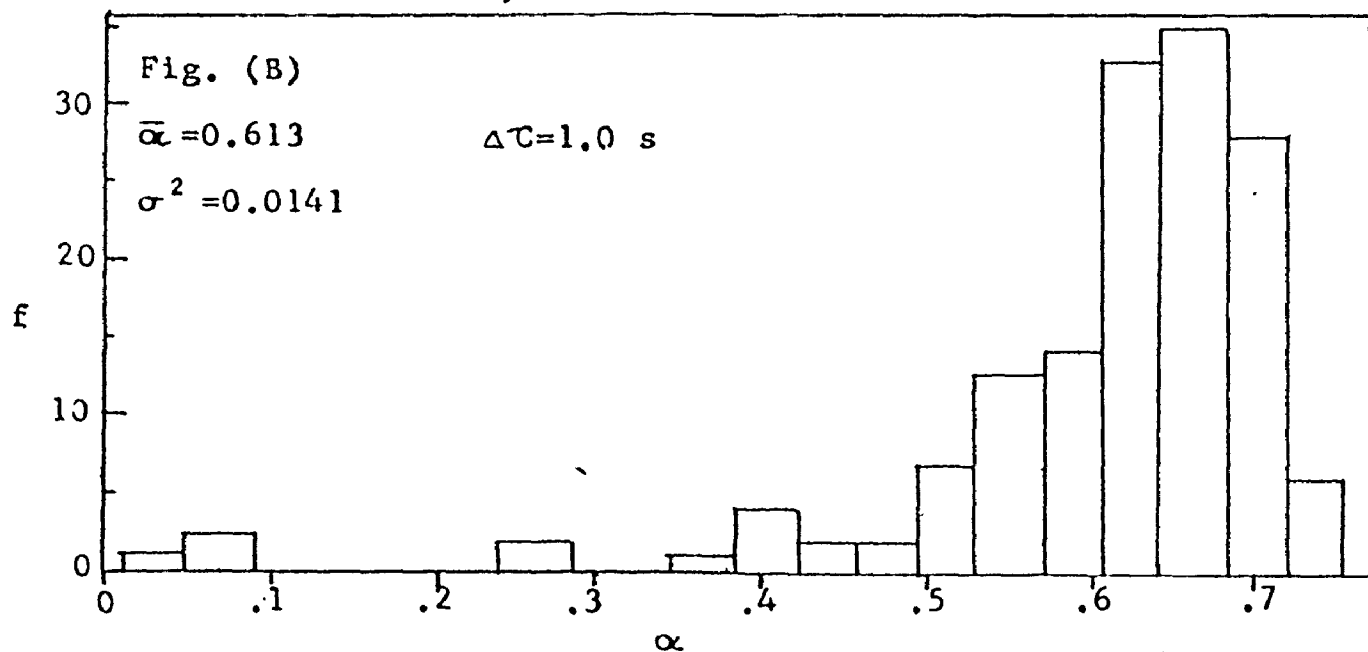
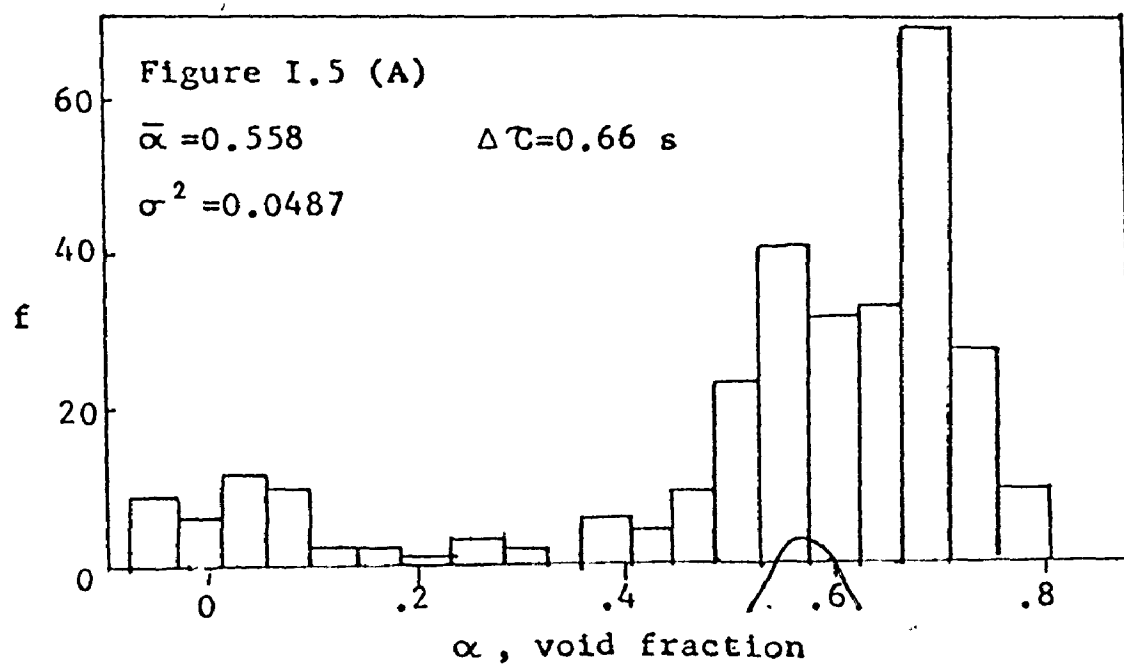


Fig. I.5 A,B,C Void histograms for small slug flow ($P_V = 0.72 \text{ s}$)

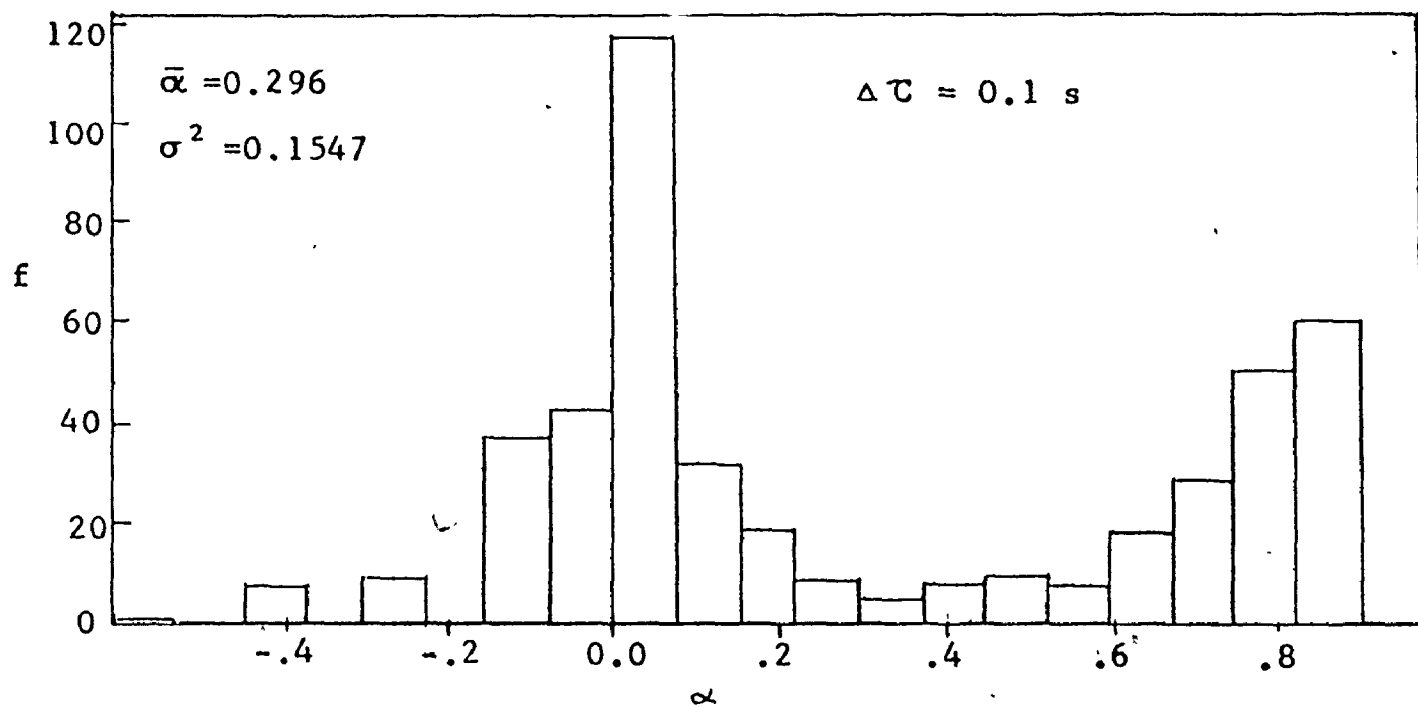


Figure I.6 Void histogram for large slug flow ($P_V=0.84 \text{ s}$).

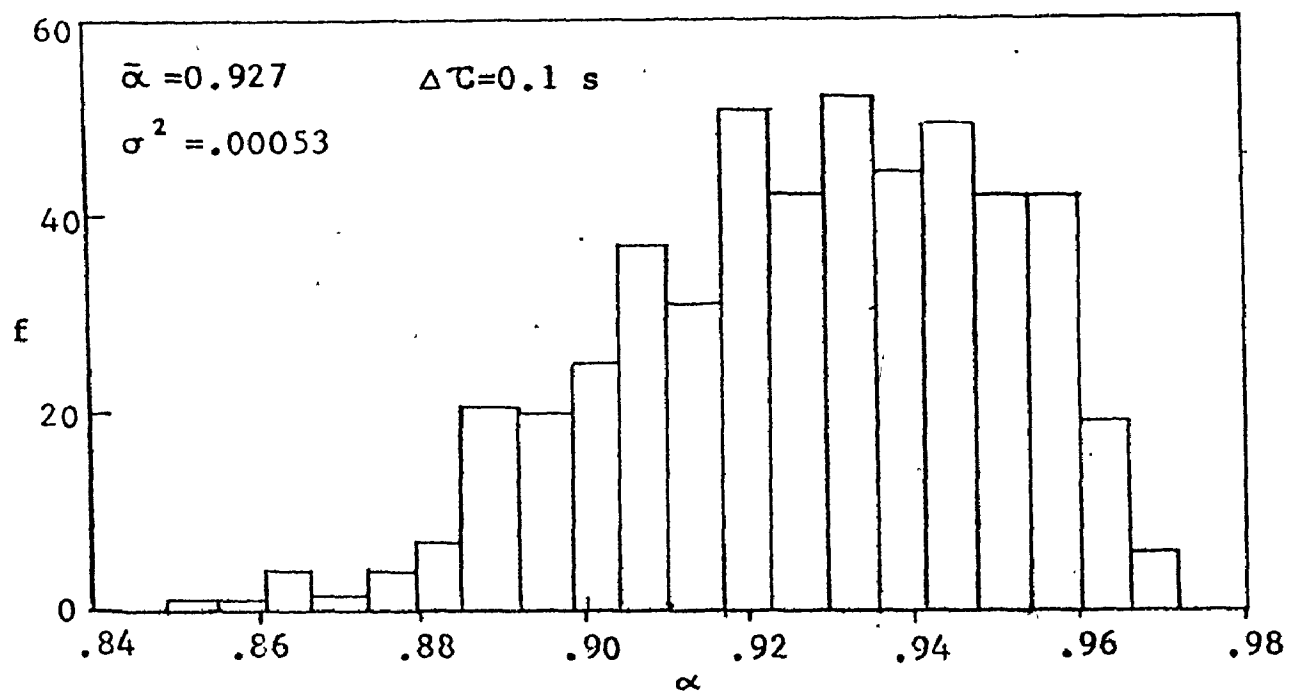


Figure I.7 Void histogram for annular flow condition.

Figure I.8

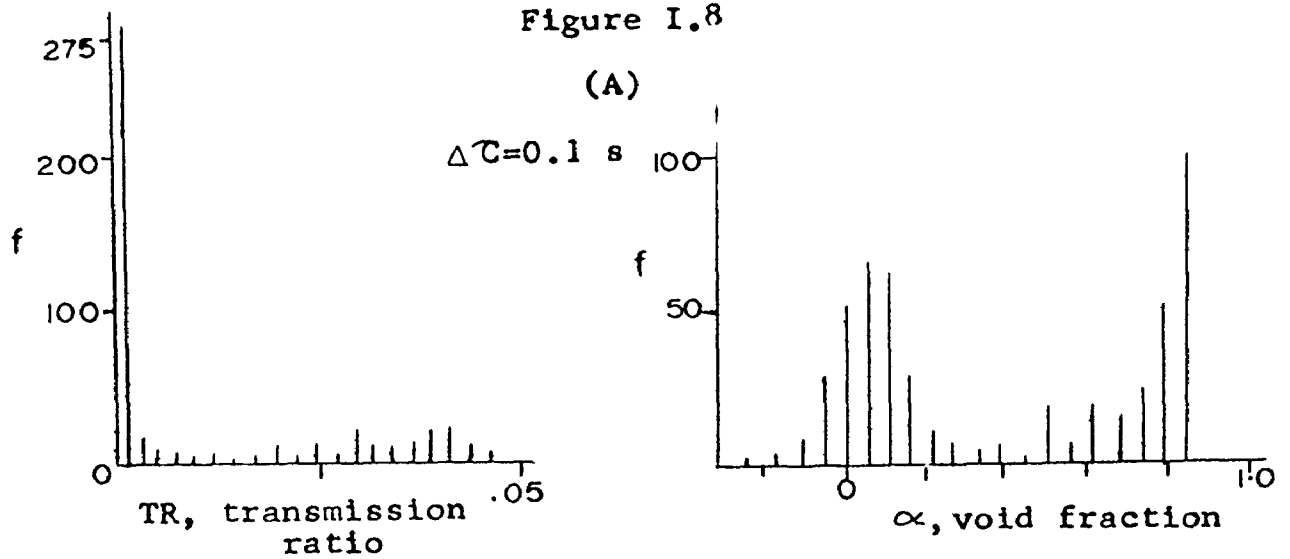


Fig. (B)

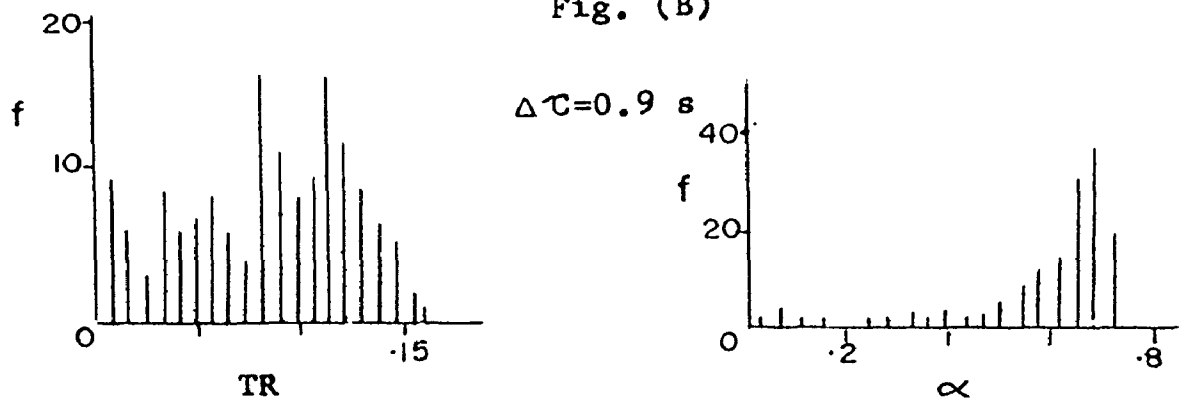


Fig. (C)

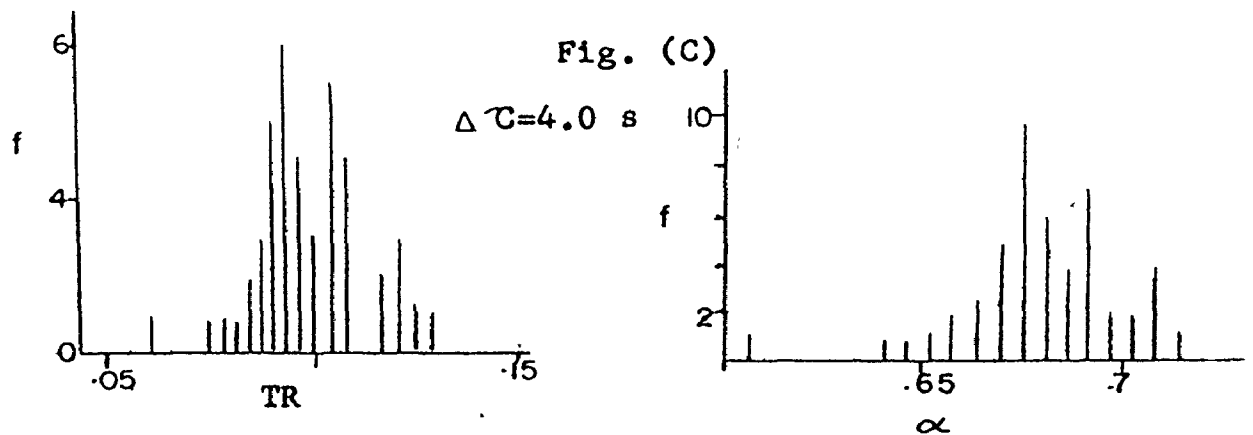


Figure I.8 - A,B,C Histogram pairs illustrating the differences between transmission ratio and void fraction distributions under slug flow conditions ($P_v = 1.0 \text{ s}$).

conditions yielded normal-type distributions for both TR and α . Annular conditions exhibited slightly negative skewed distributions, also for both TR and α . The skewness appeared more distinct for low gating periods.

Figure I.9 perhaps best summarizes the results of all the void distributions. Here the PDD variance is plotted against the gating period for the three flow conditions. The range of variance was so great however, that a log-log scale was required to include all the data. All curves show an increase in variance with a decrease in gating period. In addition, the discrete bubble and slug flow curves exhibit an abrupt change in slope when the gating period equals the characteristic period of the fluctuation.

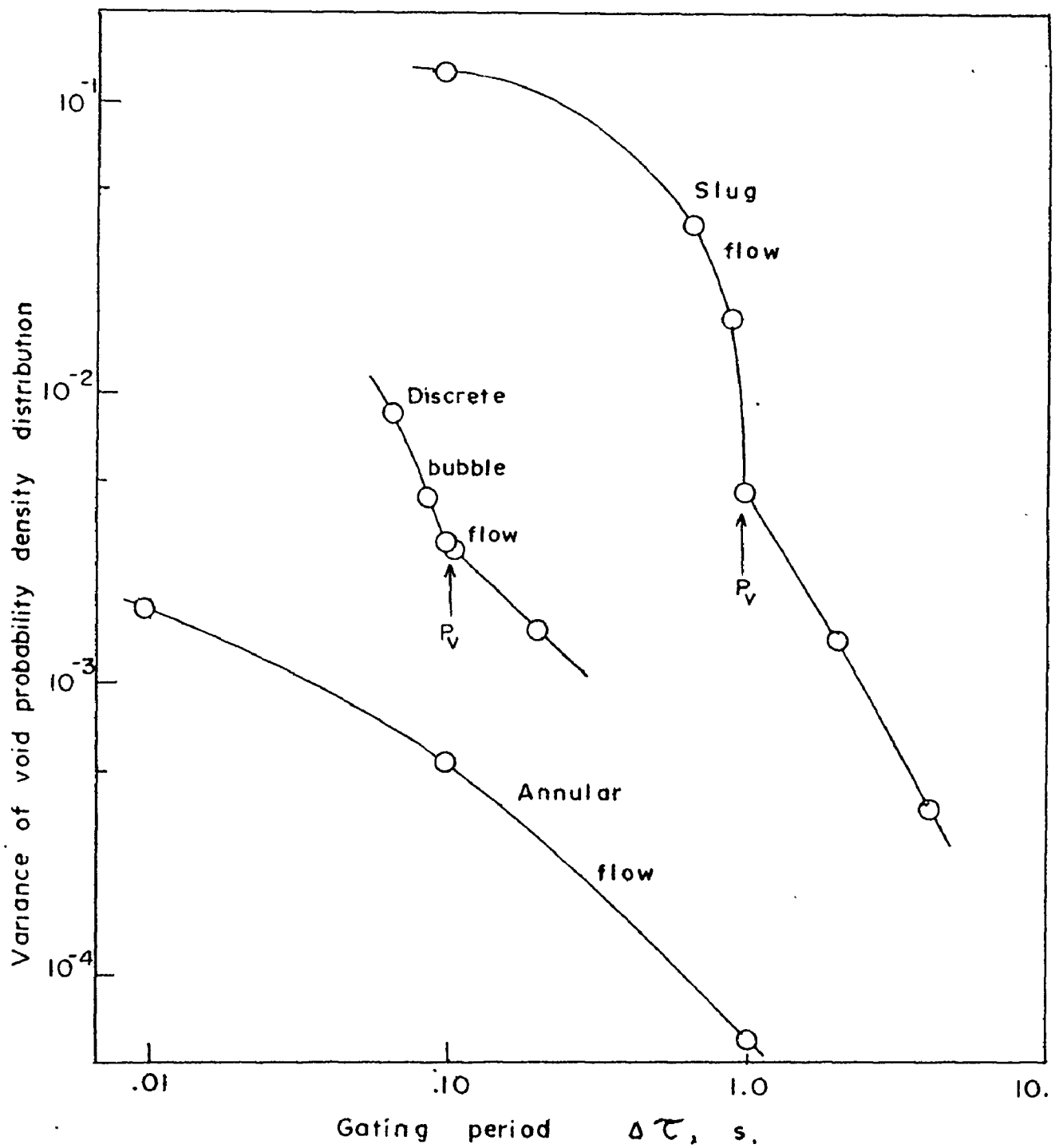


Figure I.9 Plot of PDD variance against gating period for various flow conditions.

Bubble flow - $P_V=0.105$ s, $\bar{\alpha}=0.14$ @ 0.1 s $\Delta\tau$

Slug flow - $P_V=0.99$ s, $\bar{\alpha}=0.61$ @ 0.9 s $\Delta\tau$

Annular flow - $\bar{\alpha}=0.93$ @ 0.1 s $\Delta\tau$

I.6 DISCUSSION

At first glance, the results of the discrete bubble runs as presented in Fig. I.4 appear disappointing in that no readily discernible difference in the PDD's is visible. However, of interest is the remarkable change in the variance of the distributions over a small range of ΔT . This change is significantly greater than that which can be attributed to the statistical nature of the source. Thus it must be concluded that the temporal variance of the voids is important under these conditions. The presence of void fractions less than zero is not due to computational or experimental error but is a result of source fluctuations. The increase in α with ΔT is due to transmission augmentation by the void fluctuations as described in Harms and Forrest (1971).

The result of the slug flow tests, Fig. I.5, finally do show the desired effect. In Fig. I.5A, two statistically significant maxima are visible. One is centered near zero void fraction and represents the slug passage while the other at higher α represents the bubble phase. As the gating period goes slightly beyond P_V , the distribution around $\alpha = 0$ disappears. The presence of the low void data that still linger may be attributed to the random nature of the void variation about the characteristic frequency. For ΔT sufficiently greater than P_V , the low void fraction tail disappears and a tight uniform distribution is the result. On the basis of these findings we conclude that the single mode appearance of the distributions

in the discrete bubble case, is due to a merging of the bimodal structure at the low void fractions measured.

In Fig. I.6, the dual mode effect is emphasized even more. From this type of PDD a considerable amount of information is available on the detailed flow conditions. For example, the relative areas of the two distributions represent the slug residence time ratio. However, Jones & Zuber (1974) state that although ratios are obtainable, "the lengths are indeterminant using only the PDF since there are an infinite combination of lengths which will give identical ratios". If the flow velocity and characteristic frequency are somehow available, the bubble and slug lengths are determinable by a cell model.

However, these quantities may be directly determined if the original or transformed data on a known time basis is re-examined. Fig. I.10 shows a sample of the input count rate data corresponding to the conditions of Fig. I.6. To illustrate the method, a sample calculation with a specified void period will be performed.

From Fig. I.6 we judge that $\alpha = 0.4$ is the cut-off point to distinguish the bubble from the slug portion. This translates to a raw count rate of 57 and the data as represented in Fig. I.10 are now re-examined for the interval between the bubbles using this criteria. From Fig. I.10 a series of values such as (2,3,3,3,3,4,3,5,4 . . .) is generated. The average interval over an arbitrary subset of the data was determined as 3.45 periods. Although the gating period was 0.1 second, the important quantity here is the overall measurement period,

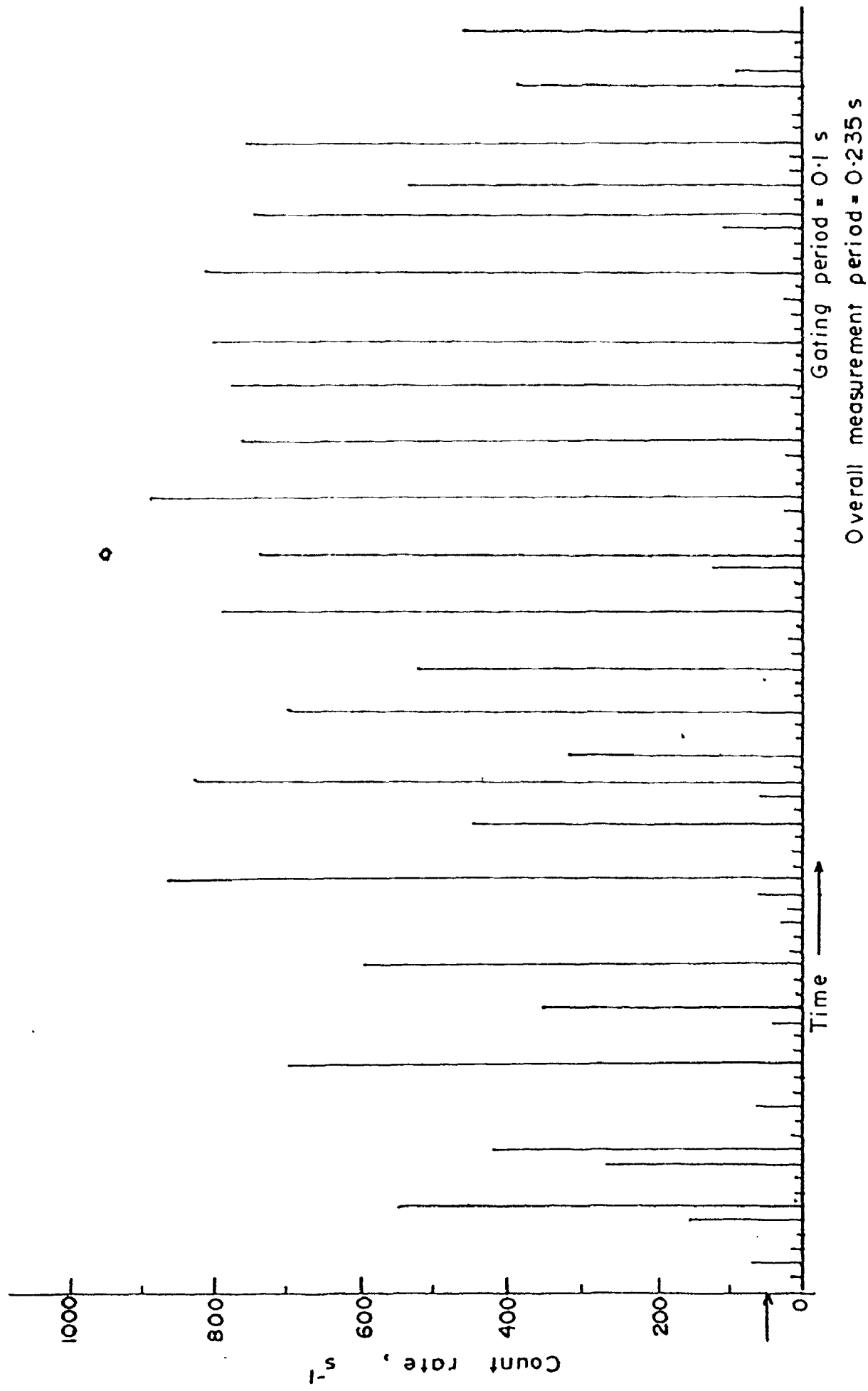


Figure I. 10 Frequency diagram of successive count rates for large slug flow ($P_v = 0.84$ s)
 (Arrow at left corresponds to count judged to distinguish bubble and slug portions)

0.235 s., which accounts also for the time delay in the pulse counting apparatus and mechanical tape system. Thus

$$\begin{aligned} P_v &= 3.45 \text{ periods} \times 0.235 \text{ s./period} \\ &= 0.81 \text{ s.} \end{aligned}$$

Within experimental error, this value compares well with the period determined independently by stopwatch of 0.84 s. Clearly the average bubble and slug residence times are also available from this data by computing the average number of successive periods in each phase.

Lastly, in the annular flow case, Fig. I.7, we observe even at a low gating period, a uniform single mode distribution. The distribution appears to be slightly negatively skewed as does the higher void distribution in slug flow. This effect might be explained by the exponential nature of the data transformation. From this PDD, a measurement of the film thickness is possible (Jones & Zuber, 1975) but only if a) the film is assumed uniformly distributed around the wall, (ie.- vertical or very high velocity horizontal flow) and b) the liquid entrained in the gas core may be ignored. Then the film thickness, δ_x , may be determined from

$$\alpha \Big|_{\max \text{ PDD}} = 1 - \frac{2 \delta_x}{x}, \quad (\text{I.6})$$

where α is the maxima of the distribution and x is the channel diameter. Equation I.6 may also be applied to the bubble portion of slug flow where α_{\max} is taken from the higher void

fraction distribution.

Now if the annular and bubble distributions are compared to that for slug flow at low ΔT , Fig. I.6, one would observe that the slug distribution appears to have the combined characteristics of both. This observation was also made by Jones and Zuber (1975) who concluded that slug flow is a transitional combination of bubbly and annular flows.

The plot of PDD variance against gating period, Fig. I.9, conveniently summarizes the desired effects on one graph. The large range of variance between flow conditions at a given gating period, even up to 2 orders of magnitude, suggests its utility as an important parameter for regime discrimination. All curves exhibit negative slopes, however the more interesting feature is the slope change in the discrete bubble and slug curves. The abruptness of the change may be attributed to the idealized cases employed and in more randomly fluctuating situations a more gradual change might be anticipated. Also, for the case of small, homogeneously distributed bubbles, one would expect a smooth curve lying closer to the annular conditions. In addition the position and slope of the annular curve itself might be expected to change if the flow conditions exhibited large periodic roll waves and a more detailed time basis was used.

Lastly, although statistics are becoming poor, it is difficult to disregard the trend in the slug flow curve at low gating periods. More possibly, the curve is approaching a

limiting variance, as might the bubble and annular curves at a low enough ΔT . This appears more plausible if we consider N measurements of a limiting dynamic case: $\alpha_n = 0, 1, 0, 1, 0, 1, \dots$. Then $(\alpha_n - \bar{\alpha}) = 0.5 = \text{constant}$, and

$$\sigma^2 = \frac{1}{N-1} \sum_{n=1}^N (\alpha_n - \bar{\alpha})^2 = \frac{1}{N-1} \cdot N \cdot (0.5)^2 \\ \approx 0.25$$

Thus our value of 0.13 at 0.1 s. ΔT is not too distant from this value. It would also be instructive to investigate the limiting behaviour of the curves at higher gating periods. We note that discrete test points at 10 s. imply a continuance of the linear trend.

I.7 CONCLUSION AND RECOMMENDATIONS

The basic conclusions resulting from the work have been developed in the discussion of the results. The following list summarizes the principal findings and developments and indicates possible directions for further work.

Freon shows promise as a medium for neutron diagnostics. When compared with water, the measured cross-section of Freon-113 implies that for a given statistical accuracy, 3.6 times the size of channel may be used. Coincidentally, its low boiling point, 47°C , and latent heat, .065 that of water, make it an ideal fluid for heat transfer studies.

Void probability density distributions are valuable in diagnosing two-phase conditions. However, a knowledge of the time basis used is needed since the gating period employed in discrete-time interrogation can significantly effect these distributions. The variance of the void PDD is in itself a descriptive trend indicator and is of use in flow pattern discrimination. Also, the fitting of known distribution forms to experimentally derived void distributions, may be of use in computer simulations involving two-phase systems.

The slug flow condition is the most readily determined by the discrete time interval method. Characteristic of the slug distribution is the appearance of two distinct maxima when the gating period is lowered below the dominant slug period. Other information available from this data is the film thickness

and bubble and slug void fractions and residence times.

For best bimodal detection the beam width should preferably be smaller than the void in size. This must be weighed against the advantage of a larger beam size to accumulate a superior statistical sampling. Also the utility of distribution statistics becomes questionable when zeros and other small digit numbers appear in the counting data. This places an effective lower gating limit on a given apparatus dependent on the source strength.

The measured variance is composed of two main contributions: a) variation due to void fluctuations and b) statistical variance at the source and in the measured count rate at the time of measurement. Thus it would be of interest to use a statistical analysis such as Barrett's (1974) to subtract out the variance effects of the source. This is discussed further in Section II.7.2 .

In light of the current findings, discrete time interval radiation diagnostics may also find potential applications ranging from pool boiling systems to the detection of channeling in fluidized bed reactors.

NOTATION

Symbols

B	representation of build-up polynomial
f	frequency of occurrence, number/interval
P_v	characteristic void period, s
T	transmitted count rate, counts/s
TR	transmission ratio, T_α / T_0
x	distance between containment walls, cm
α	void fraction, dimensionless
δ	film thickness, cm
σ^2	sample variance of probability density distribution
μ	linear attenuation coefficient, total cross-section, cm^{-1}
ΔT	gating period, s

Subscripts

x	through medium of thickness x
α	system measurement corresponding to void fraction α
o	reference measurement in empty container, $\alpha = 1$

Overscripts

-	(overbar) time-averaged value
---	-------------------------------

LITERATURE CITATIONS (Part I)

1. Barrett, P.R., "Systematic Errors in Discrete-Time Interval Transmission Method for the Estimation of Void Statistics in Boiling Channels", Nucl. Eng. Des., 30, 316 (1974).
2. Chu, K. J., and Dukler, A.E., "Statistical Characterization of Thin, Wavy Films", A.I.Ch.E Journal, 21, #3, 583 (1975).
3. Cole, R., "Bubble Frequencies and Departure Volumes at Subatmospheric Pressures", A.I.Ch.E. Journal, Vol. 13, No. 4, 779 (1967).
4. Duke, E. E., and Schrock, V. I., "Void Volume, Site Density and Bubble Size for Subcooled Nucleate Pool Boiling", Proc. Heat Transf. and Fl. Mech. Inst., 130 (1961).
5. Gaertner, R. F., "Photographic Study of Nucleate Pool Boiling on a Horizontal Surface", J. Ht. Transfer, P.17, Feb. 1965.
6. Hancox, W. T., and Harms, A. A., "Discrete-Time Neutron Interrogation of Liquid Flow Systems", Trans. Am. Nucl. Soc., 14, 699 (1971).
7. Hancox, W. T., et al, "Void Determination in Two-Phase Systems Employing Neutron Transmission", A.I.Ch.E. - A.S.M.E. Heat Transfer Conference, Denver, Colo., August 6 - 9, 1972.
8. Harms, A. A., et al, "Measurement of Time-Averaged Voids by Neutron Diagnostics", J. Appl. Physics, 42, #10, 4080 (1971).
9. Harms, A. A., and Forrest, C. F., "Dynamic Effects in Radiation Diagnosis of Fluctuating Voids", Nucl. Sci. Eng., 46, 408 (1971).
10. Harms, A. A., and Laratta, F., "The Dynamic Bias in Radiation Interrogation of Two-Phase Flow", Int. J. Heat Mass Transfer, 16, 1459 (1973).
11. Jones, O. C. Jr., and Zuber, N., "Statistical Methods for Measurement and Analysis in Two-Phase Flow", Proc. 5th Int. Heat Transfer Conf., Vol. IV, P. 200, Tokyo, Japan, 1974.

12. Jones, O.C. Jr., and Zuber, N., "The Interrelation Between Void Fraction Fluctuations and Flow Patterns in Two-Phase Flow", Int. J. Multiphase Flow, 2, 273 (1975).
13. Rallis, C.J., and Jawurek, H.H., "Latent Heat Transport in Saturated Nucleate Boiling", Int. J. Heat Mass Transfer, 7, 1051 (1964).
14. Younis, M.H., et al, "Source Fluctuation Effects in Radiation Diagnosis of Voided Fluidic Systems", Nucl. Eng. Des., 24, 145 (1973).
15. Zuber, N., "Nucleate Boiling. The Region of Isolated Bubbles and the Similarity with Natural Convection", Int. J. Heat Mass Transfer, 6, 53 (1963).

PART I
APPENDICES

- A.1 Data analysis program description.
- A.2 Tabular summary of statistics for
principal test conditions.
- A.3 Flow patterns in vertical two-phase
flow.

A.1 COMPUTER PROGRAM DESCRIPTION

A computer program was constructed to compile and analyze the neutron transmission data. Except for the subroutine converting the transmission ratios to void fractions, the program is rather conventional and therefore will not be listed. However a brief description is warranted.

The program is capable of accumulating up to 999 measurements per probability density distribution. The number of records and reference transmittance, T_0 , are read in first along with the number of measurements and gating period for each record. T_0 is pre-measured over a long time interval and all counts are corrected to a one second basis. The first 2/3 of the main program is simply for reading the count rates from the magnetic tape. For each record, the statistics of the transmission ratio readings (average and variance according to Eqs. I.2 and I.3) are then compiled by a library routine. An additional subroutine is employed to plot a histogram of this data with a specified number of subdivisions (usually 20). The transmission data are next converted to void fractions according to Eq. I.1 by an iterative technique in subroutine ALPHA (listed below). Function BUILD represents a least squares fit to the data obtained from pre-run tests (Eq. I.5). Following a tally of the void fraction statistics, another histogram is plotted.

```

C
C
C
C
SUBROUTINE ALPHA (X,SIGMA,TR,A)
THIS SUBROUTINE CONVERTS THE TRANSMITTANCE RATIO,TR, TO
THE VOID FRACTION, A.
INPUT PARAMETERS ALSO REQUIRED =
-CHANNEL THICKNESS,X, IN CM.
-TOTAL CROSS SECTION, SIGMA, IN CM.**-1.
-TRANSMITTANCE RATIO, TR=TA/T0

N=1
A=A2=0.0
IF( TR.GE.(BUILD(X)*EXP(-SIGMA*X))) GO TO 1
A=A2=-1.0
N=0
GO TO 5
1  XA=X*(1.0-A)
   F= TR- BUILD(XA)*EXP(- SIGMA*XA)
   IF (ABS(F).LE. C.00005) GO TO 6
   IF (F) 5,6,7
7  A2=A
   GO TO 8
5  N=N+1
   A=A2+ 1.0/10.**N
   GO TO 1
6  CONTINUE
   RETURN
   END

```

```

FUNCTION BUILD(XA)
BUILD =1.00 +.4848*XA-2.7903*XA**2.0+6.9359*XA**3.-5.012
5 XA**4.+ 2.1654*XA**5.0
IF (XA.LT.0.0) BUILD =1.0
RETURN
END

```

Flow conditions (Gas flow, cc/s)	Char. void period, P_v , s	Gating period, ΔT , s	Transmission ratio		Void fraction		Cross reference
			Avg.	Variance	Avg.	Variance	
Discrete bubble (~1.2)	0.105	0.066	.00734	7.03×10^{-6}	0.1161	8.64×10^{-3}	Fig. I.4 and I.9
		0.088	.00765	3.94×10^{-6}	0.1344	4.19×10^{-3}	
		0.10	.00759	2.86×10^{-6}	0.1356	3.06×10^{-3}	
		0.106	.00763	2.88×10^{-6}	0.1365	2.94×10^{-3}	
		0.20	.00765	1.61×10^{-6}	0.1401	1.55×10^{-3}	
Slug (~20-30)	0.72	0.66	.07594	2.75×10^{-3}	0.5575	4.88×10^{-2}	Fig. I.5
		1.0	.07547	1.12×10^{-3}	0.6125	1.41×10^{-2}	
		2.0	.07418	2.37×10^{-4}	0.6352	1.00×10^{-3}	
		0.1	.07678	1.42×10^{-2}	0.2957	1.55×10^{-1}	
		0.99	.1277	2.73×10^{-2}	0.4239	1.25×10^{-1}	
		0.66	.1178	4.84×10^{-3}	0.6367	3.87×10^{-2}	Fig. I.9
		0.90	.08768	1.75×10^{-3}	0.6263	1.80×10^{-2}	
		1.0	.1368	2.02×10^{-3}	0.7164	4.58×10^{-3}	
		2.0	.1065	5.54×10^{-4}	0.6882	1.41×10^{-3}	
		4.0	.0994	1.52×10^{-4}	0.6814	3.76×10^{-4}	
Annular (high)	--	0.01	.6131	2.45×10^{-2}	0.9266	1.75×10^{-3}	Fig. I.7 and I.9
		0.10	.6000	9.77×10^{-3}	0.9272	5.27×10^{-4}	
		1.00	.6410	1.28×10^{-3}	0.9377	5.98×10^{-5}	

Table A.2 Tabular Summary of Statistics for Principal Test Conditions

A.3

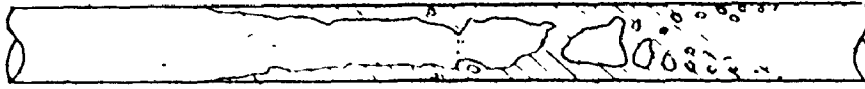


Fig. A.3.2 Flow patterns in
vertical evaporator
tube.



annular



slug



bubbly

Fig. A.3.1 Flow patterns in vertical
co-current flow.

PART II

ALGEBRAIC RECONSTRUCTION OF
TWO-DIMENSIONAL VOID DISTRIBUTIONS
FROM RADIATION ATTENUATION MEASUREMENTS

II. 1 INTRODUCTION

In recent years, a number of innovative computational methods have come to the foreground in the fields of biology and nuclear medicine. These methods are capable of reconstructing a three-dimensional image of an object such as a human brain, solely from projection measurements that are either emitted or transmitted. Here we investigate its potential application to two-phase flow systems wherein a two-dimensional representation of the time-averaged density distribution is determined.


A prime example of the importance of two-phase phenomena is in current generation nuclear reactors where higher efficiencies require release of sufficient energy into the coolant that steam voids are created. The distribution of these voids in the reactor channel is critical in any detailed control or safety analysis and is of particular interest to two-phase investigators. This interest is largely motivated by the urgent need to accurately predict the Critical Heat Flux (CHF) phenomena wherein high vapour generation in the vicinity of a fuel element creates an abrupt increase in the heat transfer rate resulting in a costly loss of fuel integrity. To be sure, CHF, is a prominent restriction on reactor design and figures prominently in any economic analysis. In addition, investigators are aware that future void-reactivity models and advanced subchannel codes will require information on the spatial, that is axial and radial, distribution of the voids. Problems with dual-phase phenomena are not restricted solely to the reactor

core. Indeed, in 1972, steam generators and condensers were the largest single cause of reactor downtime in the U.S. and major steam generator manufacturers often regard information about thermal and hydraulic conditions as proprietary. These items serve to illustrate the importance of two-phase phenomena and spatial void distributions.

As an important engineering parameter, we find the void fraction prevalent in many important design correlations. It has been demonstrated (Harms et al, 1971) that nuclear radiation can be an accurate, non-disruptive method for determining the void fraction in two-phase systems. Consequently, neutrons from a reactor beamport were employed as the diagnostic tool for this work. One must however appreciate that the void measurement is necessarily an average value along the path of the radiation. However, Evangelesti (1969) showed that a series of gamma ray measurements made in a traverse of the channel gave a superior void fraction value than that obtained by a "one-shot" technique. If we extend this idea to one more dimension, it might be expected that data from a series of traverses could be combined to obtain even more information on the internal two-phase structure. The mathematical framework is now available to permit reconstruction of a digital "picture" of the density distribution inside a voided channel.

The background for this work will be developed in Sec. II.2 which will include a review of pertinent literature and an outline of the special features and problems that are associated with applying the available algorithms to neutron

transmission measurements of a voided system. In the literature survey, we will review the status of void fraction investigations and will supply a brief history of the reconstruction methods. The theory behind these algorithms will then be summarized along with extensions thereof that were developed for the present application. The reconstruction tests of a digitized model and a real model by computer program are described next. Details of the programs are relegated to the appendices. A static voided model provides an intermediate step just short of the actual two-phase flow situation which is discussed later. The results of the test runs follow primarily in graphical and pictorial form. Interesting aspects of these results are then critically discussed followed by the conclusion and recommendations indicating directions of further progress in this area.



II.2 BACKGROUND

II.2.1 Literature Review

Kjaerheim (1972) stressed the importance of Critical Heat Flux (CHF) predictions as outlined in the introduction. Principally because of this, heat transfer must be considered the limiting factor in water-cooled nuclear reactors. In order to improve burnout predictions, he concludes it will be necessary to be able to describe local coolant conditions.

In one of the very few summaries on the subject, Lahey and Schraub (1969) review the scarce data that is available on multirod void fraction. This is primarily because of the experimental difficulties involved. Although a highlighted gamma scan study does show some interesting trends, Lahey and Schraub still find that, "these data are not directly useful in subchannel models since the track of the gamma beam passes through different type subchannels and only the average reading is obtained". Lahey and Schraub also conclude that subchannel analyses of local conditions is prerequisite for any CHF prediction that claims to be accurate.

Many studies now assume that the void fraction can be given by a simple power law distribution. This was in fact the form used by Zuber and Findlay (1965) in their well known void-quality model. However, Lahey and Schraub have pointed out that this assumption is only good as a first approximation to the radial void distribution. In addition, it is well known that voids in the coolant and moderator can significantly effect reactor criticality. Future progress in void-reactivity models,

as mentioned by Garland (1975), will require both axial and radial void profiles.

Many methods have been put forward for measuring the void fraction in test channels but only a few are applicable for studying local conditions. The most prominent for detailed measurements has been the resistance probe. However, in addition to disrupting the flow structure, probes are also limited in high pressure and temperature applications. Thus non-disruptive radiation diagnostics has often been employed as in this study. To determine the time-averaged void fraction, the method of Harms et al (1971) has been used. The presently described techniques, of course, must neglect the temporal distribution of the two phases in favour of knowledge of the spatial void distribution.

It appears that the only radiation methods that might be considered as alternatives to the method presented herein are: 1) stereoscopic X-radiography 2) placing radioactive sources inside heater rods and 3) simultaneous measurement of scattered gamma rays at 90° to the beam path (Zielke et al, 1975).

The tremendous range of application of the reconstruction methods serve to underline their importance. As far back as 1917, an Austrian mathematician, J. Radon, was able to prove that reconstruction of a 2 or 3-dimensional object from its projections was possible; but only if an infinite number from all possible angles were available could the object be exactly recreated! Thus although theorized early in this century,

these methods must be considered a product of the computer age; for it was not until the advent of high speed digital computers did anyone believe that such problems were anything but insoluble.

Among the methods now available are direct matrix techniques, summation, back-projection, Fourier transformation, and direct algebraic methods. References for these methods may be found in Budinger and Gullberg (1974). However only direct algebraic methods are considered ~~here~~, primarily because of their ease of augmentation and their inherent flexibility.

The main method employed herein is the Algebraic Reconstruction Technique (ART). ART was first introduced by Gordon et al (1970) who sought to reconstruct a 250 Å⁰ ribosome using electron microscopy. In a significant improvement over the time consuming Fourier method, it was claimed that five projections in a $\pm 30^\circ$ span were sufficient to reconstruct a 50 x 50 picture. Soon after the work of Gordon et al, Gilbert (1971) proposed the Simultaneous Iterative Reconstruction Technique (SIRT). This algorithm uses data from all projections at once to improve the reconstruction at each iteration. This adapts the procedure more readily to noisy data. Gilbert also compared the SIRT and ART algorithm on both real data and pseudo-projection data from a digitized model. The ART algorithm, along with improved versions, is reviewed again in a more comprehensive treatment by Herman et al (1973). The importance of constraints, weighted data, and ray width are discussed. These aspects will be discussed in Section II.3 when

the algorithms are presented. Herman et al also prove the convergence properties of the ART algorithms by matrix algebra. Budinger and Gullberg (1974) list and review the mathematics of most of the major reconstruction methods, and find the iterative least-squares technique, herein called LESQ, best for their nuclear medicine emission imaging. A general review of all algorithms available is also given by Gordon and Herman (1974).

Most recently, Gordon et al (1975) give a history of the reconstruction methods and describe the application of the ART algorithm to the determination of human cross-sectional X-ray pictures. Similar techniques are employed in England's EMI brain scanner. Compared to this scanner, where about 160 ray sums from 180 angles are compiled, the data for this study is crude but at least is within reach of established scanning apparatuses.

II.2.2 Features

This section highlights some of the advantages and distinguishing features that are encountered in using neutron diagnostics in algebraic reconstruction methods:

1. As described in Sec. II.2.1, previous void fraction measurements in multirod geometries have not been very useful due to the averaging effects along the beam path; this limitation is overcome by these methods of algebraic reconstruction which are capable of providing data needed for subchannel codes.

2. A reference transmission reading is required for the void fraction calculation. By first performing a duplicate set of measurements once on the empty channel, one can in effect "subtract out" internal structures such as fuel rods, tube walls, etc.
3. Because the situation is represented in digital form, this makes it amenable to a wide variety of computer techniques such as noise reduction, computer contrasting, boundary enhancement, image deblurring, etc.
4. The methods, which create a two-dimensional image from a series of 1-dimensional readings, can be extended to three dimensions if required. This would be accomplished, as for the 3-dimensional biological applications, by stacking together the planar representations.
5. The reconstruction algorithms are so general that not only wave and particle forms of nuclear radiation may be used, but also X-rays, ultrasonics, electronics, optics, magnetism, and microwaves await only the ingenious application.

II.2.3 Limitations

The following special problems and restrictions must also be appreciated for the desired application:

1. Neutron transmission data is likely to contain noise especially at low measurement intervals. Some algorithms are better than others when noise is present.
2. The requirement for good counting statistics means

that the radiation beam size will likely have to be much larger than the size of the regions of interest. To overcome this shortcoming, overlapping measurements were taken in this work and it was attempted to decouple the ray sums numerically.

3. Obvious limitations are the mechanical accuracy of the positioning system and the ability to sustain steady state conditions over the total data gathering period. Not only is the selection of the measurement period itself important but the validity of constant time-averaged conditions from measurement to measurement and projection to projection must be considered.
4. When the gating period is sufficiently long to permit good statistics, a built-in void bias due to the fluctuations of the voids, may become significant. (See Sec. I.2.2 B). This error must either be tolerated or preferably compensated for as will be discussed in Sec. II.7.2 .
5. The accuracy of the void measurement is not reliable at very high or very low values and this must be kept in mind when interpreting results. Also values of $\alpha < 0$ or $\alpha > 1$ can occur because of the statistical nature of the beam intensity. Both of these effects are undesirable in the reconstruction algorithms.
6. The entire system must be reconstructed even if it is only the conditions within one subchannel region which is of interest.

II.3 THEORY

To obtain a digital reconstruction of an object it is necessary to subdivide the square region enclosing the object into $N \times N$ smaller squares. The centre of these squares then represent the points (i,j) of the reconstruction. The matrix of points is now placed on the positive x-y coordinate axes as illustrated in Fig. II.1 . A ray is the region of the matrix lying between two parallel lines. The first ray ($k=1$) is defined to pass through point $(1,1)$ for negative angles, as in Fig. II.1, and through $(N,1)$ for positive angles. From geometry, the required equation describing the top and bottom lines of the k^{th} ray for the angle θ is

$$y_{\text{top}} = x \tan \theta - \delta \tan \theta + 1 + \frac{(k-1)B_{\text{INC}}+B_W}{\cos \theta}, \quad (\text{II.1})$$

and

$$y_{\text{bot}} = x \tan \theta - \delta \tan \theta + 1 + \frac{(k-1)B_{\text{INC}}}{\cos \theta} \quad (\text{II.2})$$

for $0^\circ < \theta < 90^\circ$,

given $\delta = 1$ for $0^\circ < \theta < +90^\circ$,

$\delta = N$ for $-90^\circ < \theta < 0^\circ$,

where B_W is the beam width and B_{INC} is the beam increment distance, both in units of the reconstruction mesh, u . In previous works, it was assumed that $B_W=B_{\text{INC}}=1$ u . The above descriptions permit greater flexibility as will be seen.

If the point (i,j) lies within ray k or on the bottom line defining the ray, then the value of the square centered at (i,j) is considered to contribute to the k^{th} ray sum. On

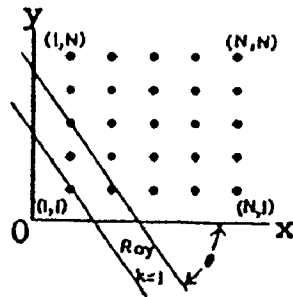


Figure II.1 Reconstruction matrix
on coordinate axes.

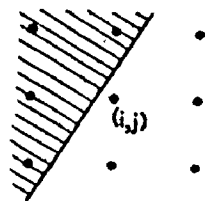


Figure II.2 Basis of subroutine
SMOOTH.

the other hand, if greater accuracy is required, we can compute the exact fraction of the square that the ray k intersects. This then yields the "weighted" projection data described by Herman et al (1973). This operation however, will involve about twice as many points for each ray, sum computation and also multiplication of weighting factors at each point. Herman et al conclude that the small improvement gained in accuracy "does not seem to be worth the additional cost". The unweighted approach has therefore been used in this work.

Herman et al (1973) also found that the choice of ray width can have a significant effect on the performance of their algorithm. For a uniform picture a beam width of $1 u$ would reflect a disproportionate number of square centers in adjacent rays. This phenomena has been termed "streaking". The streaking effect is particularly bad near 45° and a variable size beam width given by

$$B_W(\theta) = (|\cos\theta| + |\sin\theta|) u , \quad (II.3)$$

was suggested to overcome it (Herman et al, 1973). This problem was minimized in this study by selecting beam widths larger than $1 u$ and not a simple multiple of u .

All methods require an estimate of the sum of densities from each point in the ray. Although the ray density may be derived directly from the void fraction, it is more convenient to define a dimensionless two-phase density parameter to correspond with the literature discussions. This

parameter may be defined from basic principals analogous to the void fraction α (Harms and Laratta, 1973), however it is more descriptive to begin with the common description of the mixture density in a voided channel (Davis, 1974). For constant temperature and pressure

$$\rho_m = \rho_g \alpha + \rho_l(1 - \alpha) \quad , \quad (II.4)$$

where the subscripts indicate the dimensional mixture, gas, and liquid densities. We now choose to form a dimensionless parameter by normalizing the mixture density with respect to the liquid density,

$$\rho \equiv \frac{\rho_m}{\rho_l} = \frac{\rho_g}{\rho_l} \alpha + (1 - \alpha) \quad . \quad (II.5)$$

A common valid assumption in radiation diagnostics when $\rho_g \ll \rho_l$ is to neglect attenuation in the voids. Eq. II.5 then becomes simply

$$\rho = 1 - \alpha \quad . \quad (II.6)$$

Thus the density measurement along a given path will conveniently be described in the interval $0 \leq \rho \leq 1$. Coincidentally, ρ is roughly equivalent to the density of the air-water system in cgs units.

The determination of ρ from attenuation measurements is now determined according to Harms et al (1971),

$$T_{\alpha} = T_o B(X\rho) e^{-\mu X\rho} , \quad (II.7)$$

where T_{α} and T_o are the system and reference transmitted count rates and B represents the build-up correction factor, μ is the linear attenuation coefficient or removal cross-section (cm^{-1}) and X is the effective linear distance that the beam intersects the matrix. If the beam width is other than unity then,

$$X = \frac{\text{Area of beam intersecting object (matrix)}}{B_W} u ,$$

which is then converted to cm. by the reconstruction scale. The true measured ray sum of width B_W is then given by

$$T_{k(\theta)} = \rho_{k(\theta)} \cdot X_{k(\theta)} \cdot B_W . \quad (II.8)$$

The beam area used in neutron diagnostics must be large enough to accumulate statistically adequate count samples. Because of the fixed beam width which is too large to provide sufficient details in the reconstruction, overlapping measurements were taken. The effective ray sums $S_{k(\theta)}$ of width B_{INC} may be calculated from the measured ray sums. This situation may be described in matrix form for the case $B_R=B_W/B_{INC}=5$ by

$$\begin{vmatrix} 11111 & & & & \\ 11111 & & & & \\ 11111 & 0 & & & \\ 11111 & & & & \\ & \cdot & & & \\ & \cdot & & & \\ & \cdot & 11111 & & \\ 0 & & 1111 & & \\ & & 111 & & \\ & & 11 & & \\ & & 1 & & \end{vmatrix} \times \begin{vmatrix} S_1 \\ S_2 \\ S_3 \\ \cdot \\ \cdot \\ \cdot \\ S_{k_{\max}} \end{vmatrix} = \begin{vmatrix} T_1 \\ T_2 \\ T_3 \\ \cdot \\ \cdot \\ \cdot \\ T_{k_{\max}} \end{vmatrix}, \quad (II.9)$$

where the dimension of the coefficient matrix is $k_{\max} \times k_{\max}$. k_{\max} is the total number of rays required at each angle and is determined by compiling ray sums, $(k=1,2,\dots,k_{\max})$ until a sum is encountered that contains no further points on the $N \times N$ matrix. It may also be determined from (Gordon et al, 1970)

$$k_{\max}(\theta) = \left[\frac{(N-1)}{B_{\text{INC}}} \cdot (\sin|\theta| + \cos \theta) \right] + 2, \quad (II.10)$$

where B_{INC} now represents the effective beam width and the square brackets imply truncation to the next lowest integer. It is also useful to define B_{DIF} , the difference in B_W and B_{INC} in units of B_{INC}

$$B_{\text{DIF}} = \frac{(B_W - B_{\text{INC}})}{B_{\text{INC}}} = B_R - 1. \quad (II.11)$$

For pseudo-projection data, the system of Eq. II.9 can be solved exactly by back substitution starting with $S_{k_{\max}} = T_{k_{\max}}$.

However, B_{DIF} additional measurements are possible in addition to Eq. II.9 similar to the last B_{DIF} . The first 4 rows of the coefficient matrix then become

$$\begin{vmatrix} 1 \\ 11 \underline{0} \\ 111 \\ 1111 \\ \text{etc.} \end{vmatrix}$$

for the case $B_R=5$. These additional data will overdetermine the system and are important in real data tests where noise is present in the measured sums, T_k . The solution procedures for real data are dealt with further in Sec. II.6. If, for example, because of the possible errors we decide to solve this overdetermined system by a least squares criteria, $(\underline{A}^T \underline{A}) \underline{x} = \underline{A}^T \underline{b}$, then Eq. II.9 becomes

$$\begin{vmatrix} 54321 \\ 454321 \underline{0} \\ 3454321 \\ 23454321 \\ 123454321 \\ 123454321 \\ \cdot \\ \cdot \\ \underline{0} \\ 123454 \\ 12345 \end{vmatrix} \times \begin{vmatrix} S_1 \\ S_2 \\ \cdot \\ \cdot \\ \cdot \\ \cdot \\ S_{k_{max}} \end{vmatrix} = \begin{vmatrix} T_1+T_2+\dots+T_5 \\ T_2+T_3+\dots+T_6 \\ \cdot \\ \cdot \\ \cdot \\ \cdot \\ T_{k_{max}}+\dots+T_{k_{max}+B_{DIF}} \end{vmatrix} \quad (II.12)$$

Note in the above discussion, that for overlapping measurements we require B_W to be an integer multiple of B_{INC} .

Algorithms

The first algorithm to be introduced is the additive ART2 algorithm of Gordon et al (1970), where A represents the reconstruction matrix of point values of ρ and \tilde{A} is an auxil-

iary estimator. Thus for pseudo-projection data we have

$$\tilde{A}^{q+1}(i,j) = \tilde{A}^q(i,j) + \frac{P_k(\theta) - R_k^q(\theta)}{N_k(\theta)} , \quad (II.13)$$

with constraints

$$A^q(i,j) = \begin{cases} 0 & \text{if } \tilde{A}^q(i,j) < 0 \\ \tilde{A}^q(i,j) & \text{if } 0 \leq \tilde{A}^q(i,j) \leq 1 \\ 1 & \text{if } \tilde{A}^q(i,j) > 1 \end{cases}$$

where

q = iteration number,

R^q = ray sum computed from the reconstruction for ray k at angle θ , q^{th} iteration ,

P = ray sum computed from pseudo-projection data; that is, from digital model ,

N = number of points contained in k^{th} ray at angle θ .

The above expression has "fully constrained" ρ in the range of 0 to 1. If only non-zero ρ values were prohibited, the algorithm is then termed "partly constrained". Best results from this work indicate that $A^0(i,j)$, the initial condition, should be set to the average ρ value obtained from input data. Thus from any projection

$$\tilde{A}^0(i,j) = A^0(i,j) = \frac{\sum_{k=1}^{K_{\text{max}}} (T_k/B_R)}{N \times N} . \quad (II.14)$$

For real data where the effective beam width is not unity, the following modification is suggested

$$\tilde{A}^{q+1}(i,j) = \tilde{A}^q(i,j) + \frac{S_k(\theta)}{X_k(\theta) \cdot B_{INC}} - \frac{R_k^q(\theta)}{N_k(\theta)}, \quad (II.15)$$

with constraints as above and $S_k(\theta)$ determined from the real data measurements $T_k(\theta)$ of Eq. II.8 . Now $X_k(\theta) \cdot B_{INC}$ represents the effective area that corresponds to the ray sum measurement $S_k(\theta)$ and $N_k(\theta)$, although defined the same, may be considered as an estimate of the corresponding area in the reconstruction.

The additive SIRT algorithm of Gilbert (1972) is somewhat similar. For real data of effective beam width B_{INC} ,

$$A^{q+1}(i,j) = A^q(i,j) + \frac{\sum_{\theta} S_k(\theta)}{\sum_{\theta} X_k(\theta) \cdot B_{INC}} - \frac{\sum_{\theta} R_k^q(\theta)}{\sum_{\theta} N_k(\theta)}, \quad (II.16)$$

where if

$$A^q(i,j) < 0, \quad A^q(i,j) = 0,$$

$$\text{and } A^0(i,j) = \text{average } \rho \text{ (Eq. II.14)}.$$

Here the summations indicated are over all angles where the point (i,j) belongs to the $k(\theta)^{th}$ ray. The multiplicative form of this algorithm is

$$A^{q+1}(i,j) = A^q(i,j) \cdot \frac{\sum_{\theta} S_k(\theta)}{\sum_{\theta} X_k(\theta) \cdot B_{INC}} \cdot \frac{\sum_{\theta} R_k^q(\theta)}{\sum_{\theta} N_k(\theta)} \quad (II.17)$$

and an analogous multiplicative algorithm exists for the ART method. The additive algorithms exhibit generally better performance and are better suited to transmission data (Gordon,

1974). An additional version of ART, ART3 (Gordon, 1974), is designed for noisy data since it accepts a solution within a certain tolerance, ϵ , which avoids the troubles caused by trying to satisfy inconsistent real data.

The final method is the iterative least squares technique of Goiten (1971) and Budinger and Gullberg (1974), called LESQ here. Logically when errors may be present in the measurements, this method requires an estimate of the A matrix by a minimum to a least squares function

$$\sum_{\theta} \sum_k \frac{(S_k(\theta) - R_k^q(\theta))^2}{\sigma_k^2(\theta)},$$

where $\sigma_k^2(\theta)$ is the variance in the measurement of $S_k(\theta)$.

This criteria then yields the LESQ algorithm

$$A^{q+1}(i,j) = A^q(i,j) + d \Delta^q A(i,j), \quad (\text{II.18})$$

where for unity weighting factors,

$$\Delta^q A(i,j) = \left\{ \sum_{\theta} \frac{S_k(\theta) - R_k^q(\theta)}{\sigma_k^2(\theta)} \right\} / \sum_{\theta} \left(\frac{1}{\sigma_k(\theta)} \right)^2$$

Here, d is a required damping factor and when determined by a least squares sense is given by

$$d = \frac{\sum_{\theta} \sum_k (S_{k(\theta)} - R_{k(\theta)}^q) \left[\sum_{(i,j) \in k(\theta)} \Delta^q A(i,j) \right] / \sigma_{k(\theta)}^2}{\sum_{\theta} \sum_k \left[\sum_{(i,j) \in k(\theta)} \Delta^q A(i,j) \right]^2 / \sigma_{k(\theta)}^2}$$

Once these algorithms are implemented, it is desirable to have some way to gauge the progress of the reconstruction at each iteration. The following two commonly encountered parameters are of use in this respect. The discrepancy, δ , may be thought of as the root mean square Euclidean "distance" between the reconstruction and the original, normalized by the standard deviation of the original. It is defined by

$$\delta^q = \left[\frac{\sum (A^i(i,j) - A^q(i,j))^2}{\sum (A^i(i,j) - A^0(i,j))^2} \right]^{\frac{1}{2}}, \quad (\text{II.19})$$

where $A^i(i,j)$ contains the known values from the model and $A^0(i,j) = \text{Avg.}$ from Eq. II.14. From the above definition we can interpret $\delta = 1$ as meaning that no progress has been made while $\delta = 0$ represents the ideal case when the object has been exactly recreated.

The variance, V , is an estimate of the non-uniformity of the picture and is defined by

$$V^q = \frac{\sum (A^q(i,j) - \text{Avg})^2}{N^2}. \quad (\text{II.20})$$

As suggested by Herman et al (1973), the change in the variance provides a method for stopping the iterative process. If

$$v^{q+1} - v^q < v^q/100 ,$$

that is, when the change in variance is less than 1% of the previous value, the process is terminated. Since the variance doesn't require data from a known model to compute it, it may be used for real projection data tests as well.

Although the large variety of computer enhancing techniques that are available in the literature were not employed in this work, the following three ideas to improve the reconstructions were tried.

1. In a reconstructed picture the density variation from point to point may be substantial, as discussed in Sec. II.6, but it is often the average value for a given region which is of interest. In an attempt to improve the uniformity within the observed regions of the reconstruction, the routine SMOOTH was created. For a 2-D representation, each internal point (i,j) is surrounded by 8 neighbours. Any region boundary if large compared to the point spacing must still leave at least four points in the same region (See Fig. II.2). Quite simply then, SMOOTH searches for the 4 points closest in value to (i,j) and then reassigns (i,j) the average value of these 5 points. A listing of SMOOTH is provided in Appendix A.5 and its effect is discussed in Sections II.6 and II.7 .

2. In two-phase systems, values for ρ of 0 or 1 may be prevalent and this fact should be taken advantage of. The technique, herein designated as FORCE, is a single step

which is implemented after allowing a couple of iterations. Then if a point has progressed a given distance from the average value it started at, it is assigned the appropriate value 0 or 1 according to the direction it was heading. The regular iteration process is then continued to ensure that the reconstruction satisfies the projection data. It is hoped that this single step forcing the points to their final value, could improve the progress of the iterative procedure. An example of the implementation of FORCE within the SIRT algorithm is given in Appendix A.4.4 and its effect is discussed in Sections II.6 and II.7 .

3. In this application, information is often available on the system geometry and it can be employed in the algorithms. For example, any density value outside the known dimensions of the test channel wall is set to zero. The results of adding the constraint of known geometry are illustrated in Sec. II.6 .

II.4 APPARATUS

The principal pieces of apparatus employed in the experimental portions of this work are as follows:

A lucite model was constructed for the real-projection tests to simulate a static two-phase situation. Lucite, a clear plastic, was chosen because its total cross-section is very similar to that of water (Hancox et al, 1972). The model is 0.8 inches (2.03 cm) in diameter and can be oriented in any of 15 position angles on its base. The base is equipped with a vernier positioner and is mounted on a rigid stand. This apparatus is pictured in Figure A.1 ,

Neutrons from a beamport of the McMaster University 2 MW(t) swimming pool type nuclear reactor were employed as the radiation. The energy spectrum is largely Maxwellian with an epithermal component.

The beam intensity was measured with a standard BF_3 detector with attendant pulse counting electronics and a magnetic tape system for data storage. A cadmium sleeve gaped down to 0.25 in. wide by 0.5 in. deep (1.27cm by 0.635 cm) was placed over the detector. Thus the beam width for this study was fixed at 0.25 in. (0.635 cm). With this configuration, the unattenuated count rate was $\sim 3 \times 10^5$ c/s.

II.5 PROCEDURES

The following description chronologically outlines the steps taken to fulfill the study objectives.

In the first part of the investigation, a program was developed to perfect the geometrical expressions and test the available reconstruction algorithms. This program, henceforth called PSEUDO, considers Fig. II.3 as a 19×19 digital model to simulate a hypothetical time-averaged density distribution. The horizontal elongation of Fig. II.3 is a printer limitation. The initial tests performed with PSEUDO used overlapping rays whereas all subsequent tests decouple the individual ray sums from the overlapping measurements. Algorithms tried were ART2, ART3, SIRT, and LESQ, with later emphasis on ART2 and SIRT. The effectiveness of the algorithms was compared and additional tests were performed on the pseudo-projection data to study the behaviour of SMOOTH and FORCE. Details of all main programs and subroutines may be found in the appendices.

It was next decided that reconstruction of a real model should be attempted using actual neutron attenuation measurements. Thus a lucite model with known internal features was constructed as described in Sec. II.4 . The positioning of this apparatus with the source and detector fixed is illustrated in Fig. II.4 . Note that for negative angles the first ray starts at the point (1,1) while for positive angles it is the point (N,1) of the reconstruction matrix. We interject

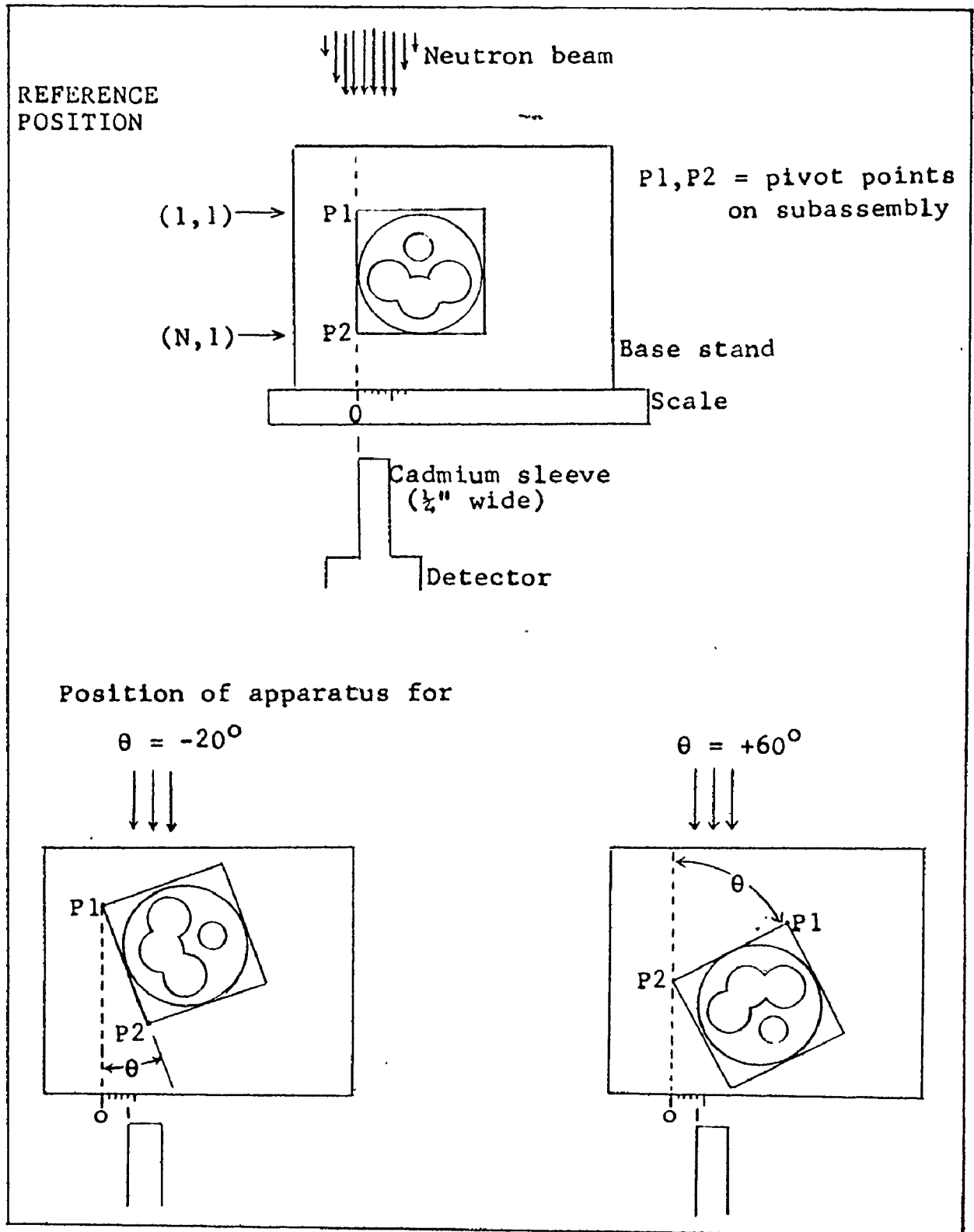


Figure II.4 Sketch of model positioning mechanism when source and detector are immobile.

to note that for the application to a two-phase flow system, the test channel would of course, be fixed; the gamma or X-ray source and detector would then have to be appropriately positioned about the test section. Next, the linear attenuation parameter of lucite, μ , and the build-up expression $B(Xp)$, had to be determined. This was accomplished using the method described by Harms et al (1971) in Eqs. 1.4 and 1.5 with known lucite thicknesses. In addition, it was decided that the model was to be reconstructed on a 40 x 40 mesh this time. Hence 40 u = 0.8 inches, 1 u = 0.02 inches (.0508 cm) was the scale of the reconstruction. Two sets of conditions were employed: i) $B_{INC}=2.5$, $\Delta T=20. s$ to obtain good data for a coarse increment, ii) $B_{INC}=1.25$, $\Delta T=2.0 s$ to see how the algorithms would perform on noisy data with a finer increment. However, outputting these results digitally would be cumbersome and difficult to interpret. Thus half-tone output via lineprinter was employed. Subroutine PIX, described in Appendix A.5.1, was created for this purpose. Ten gray levels were deemed satisfactory for our purposes since only a method for rapid evaluation of the reconstructions was desired and most radiation measurements are accurate to within about 10% anyway. The characters which were finally decided upon are displayed in Fig. II.5 which may be used as a key for interpreting subsequent figures. Note that the interval, $0 \leq p \leq 0.1$, is represented by a blank. Figure II.6 compares the original hand-drawn version of the PSEUDO model with the output of PIX. These should also be compared to the digitized version already

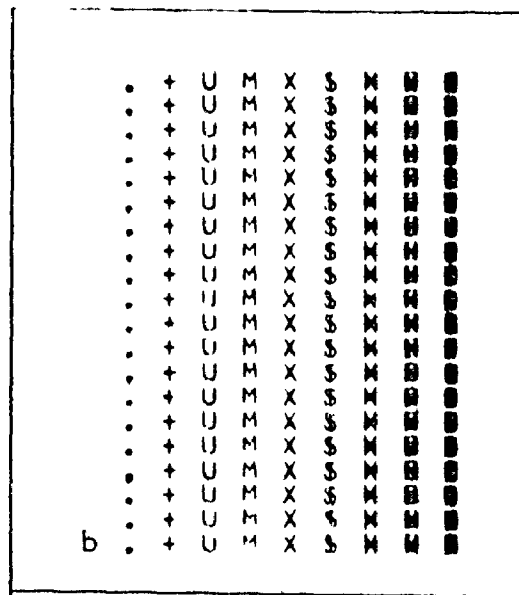


Figure II.5 Ten gray-level overprinting characters.

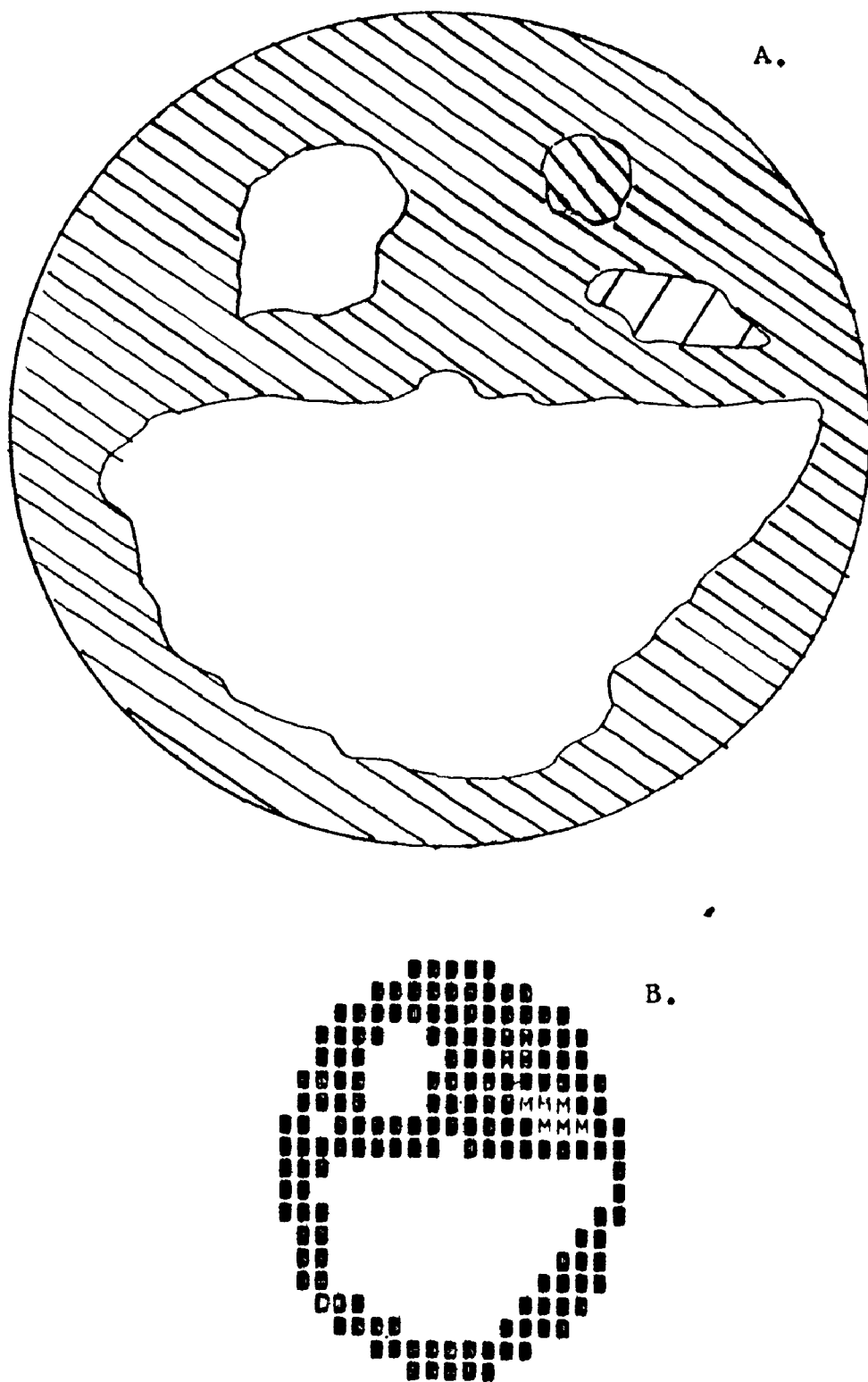


Fig. II.6 Two-phase model for pseudo-projection data

A. as originally drawn,
B. as represented by overprinting routine PIX.

presented in Fig. II.3 . The oval shape of the PIX output, rather than the correct circular shape, is due to the fixed print space height being greater than the print space width. For any precise evaluation of a reconstruction, the numerical values in the array must of course be displayed on a square grid. Details of the computer program used to compile the real projection data and reconstruct the model, henceforth called REAL, may be found in Appendix A.3.2 . Many portions are in common with the PSEUDO program. However, for the REAL tests, many different methods were tried other than direct back substitution to compute the individual ray sums - among them iterative techniques with relaxation, weighted least squares, and transmitted count rate differencing.

Although application to an actual two-phase flow situation was not performed here, extension to the dynamic case is discussed using portions of analyses already available in the literature.

A handwritten mark, possibly a signature or initials, consisting of a large loop followed by a vertical line and a small hook at the bottom.

II.6 RESULTS

In all, approximately twenty sets of tests were performed on pseudo-projection data. Selected important cases are compared in Fig. II.7 which indicates the progress of the reconstruction at each iteration. The ordinate is the discrepancy parameter, δ , and it will be recalled that a lower value for δ means a more accurate reconstruction. Curves A to D demonstrate the effect of the beam increment, in units of u , but do not employ the decoupling of the measured ray sums as all subsequent tests do. In all cases the number of projections, M , is 10. By way of comparison, if $M=5$ curve D would be located just below where A is now. Also if ART3 ($B_{INC}=2$, $\epsilon=.001 \times N_k(\theta)$) were placed on this plot, its curve would lie just below B. In all cases studied, fully constrained applicable algorithms performed better than unconstrained or partly constrained forms. Results also indicate that it is preferable to start the iteration process with the matrix A set equal to the average value rather than a null matrix.

Figures II.8, II.9, and II.10 present digitally the results of the ART2, SIRT, and LESQ algorithms respectively. The conditions of these reconstructions are included along with their discrepancy and variance parameters. In addition, Fig. II.8 also shows the ART reconstruction via the overprinting routine in an insert. One further comparison of the

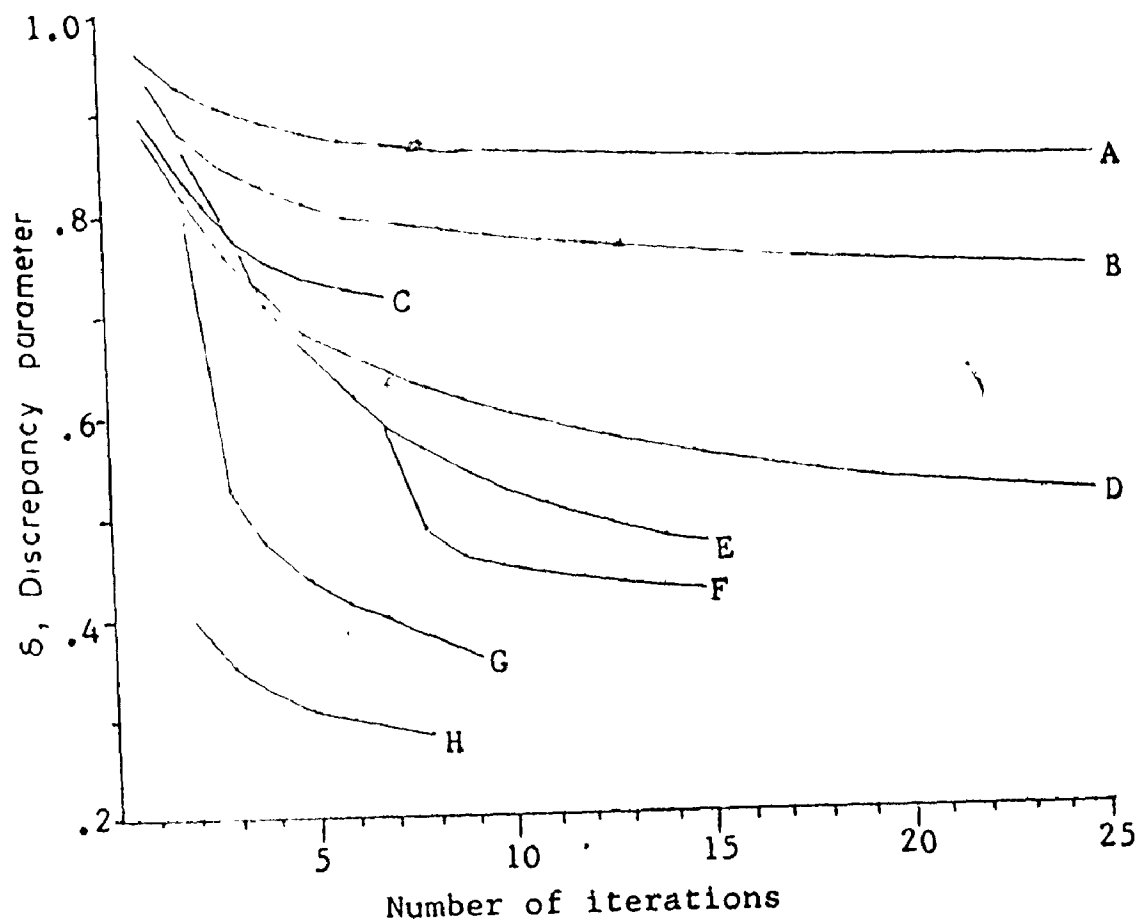


Fig. II.7 Discrepancy parameter, δ , vs. number of iterations for various algorithms and conditions. Ten projections used in all cases.

- A. ART2, BINC=BW, BW=6.35, overlap but no differencing of ray sums
- B. ART2, BINC=5, same as A
- C. ART2, BINC=2, same as A
- D. ART2, BINC=1, same as A
- E. Add. SIRT, BINC=1, BW=4
- F. Mult. SIRT, same as E, FORCE applied at it'n #7
- G. LESQ, BINC=1, BW=4, $\sigma^2 = .0001 \times N_{k(e)}^2$
- H. ART2, BINC=1, BW=4

[illegible]

M=10
B_{INC}=1
B_W=4

$$\delta = .258 \quad v = .204$$

Figure II.8 ART2 reconstruction in digitized form and via PIX (insert)

MATRIX AFTER 15 ITERATIONS

0.00	0.00	.06	.14	.11	.28	.26	.78	.95	1.09	.92	.70	.70	0.00	0.00	0.00	.22	0.00	0.00
0.00	.26	0.00	.24	.54	.59	.71	.79	1.05	.74	.80	.95	1.05	.85	.23	.27	0.00	0.00	.01
0.00	.41	.16	.49	1.03	.82	.94	.59	.95	.90	.99	1.15	1.05	.95	.61	.63	.22	.04	0.00
.18	.14	.57	.82	.81	.78	.22	.33	.82	1.04	1.01	.82	.71	.95	.80	.90	.69	.31	.05
.24	.18	.67	.84	.86	.25	.25	.30	.65	.82	.89	.98	1.01	.87	.80	.84	.91	.55	.15
0.00	.73	1.02	1.00	.86	.34	.14	.26	.72	.94	.85	1.03	.97	1.11	1.00	.80	.74	.76	.25
.66	.78	1.19	1.03	.80	.54	.20	.46	.76	.83	.91	1.05	1.04	.57	.52	.71	.89	.60	.63
.63	.65	.79	.84	.57	.64	.79	.71	.93	.88	1.11	1.01	.85	.62	.74	.73	.52	.96	1.10
.88	1.03	1.10	.87	.76	.77	.94	.96	.72	.51	.82	.87	.83	.85	.85	.97	1.00	.93	.39
1.07	.80	.71	.22	.27	0.00	.14	.11	.06	.02	.21	.05	.12	.10	.10	.26	.17	.16	.98
.92	.93	.40	.10	0.00	0.00	.17	0.00	0.00	0.00	.13	.06	.07	.01	.13	0.00	.09	.09	.70
.51	.78	.59	.14	.19	0.00	0.00	0.00	.06	.01	0.00	0.00	0.00	0.00	.02	.17	.35	.57	.80
.53	.94	.72	.16	.04	.16	0.00	0.00	.11	.07	.02	.06	0.00	0.00	.17	.10	.74	.90	.35
.20	.62	.62	.31	.19	.10	0.00	0.00	0.00	0.00	.01	0.00	.06	.13	.18	.65	.86	.83	.06
0.00	.83	.81	.44	.06	0.00	.02	.03	.01	0.00	0.00	0.00	.19	.62	.56	.74	.77	.76	.12
0.00	.27	.82	.61	.55	.25	.25	.15	.15	0.00	0.00	.10	.45	.60	.80	.88	.72	.36	0.00
0.00	.11	.24	.94	.65	.56	.67	.45	.18	.33	.11	.30	.66	.87	.86	.82	.18	.10	.06
0.00	.17	.41	.04	.18	.73	.88	.70	.75	.90	1.00	.70	.43	.76	.49	.18	.00	0.00	0.00
.25	.10	0.00	0.00	.18	.33	.00	.66	.76	1.06	.85	.89	.23	.15	.18	.30	.13	.01	0.00

Figure II.9 SIRT reconstruction in digitized form.

M=10
BINC=1
BW=4

$\delta=.458$ $V=.138$

0.00	0.00	0.00	0.00	0.00	0.00	.21	.85	.88	1.00	.83	.57	.76	.20	0.00	.02	0.00	.04	.07	.18
0.00	.07	0.00	.06	.39	.68	.93	1.00	.96	1.00	.98	.80	1.00	.93	.76	.03	0.00	0.00	.04	
0.00	0.00	.04	.44	.87	.52	.97	.80	1.00	1.00	1.00	.99	.75	.97	.99	.59	.19	0.00	0.00	
0.00	.07	.54	1.00	.96	.93	.39	.32	.86	.90	.99	.99	.98	.63	.88	.95	.52	0.00	.02	
0.00	.29	.99	1.00	.93	.21	.12	.28	.44	.93	.98	.99	.98	.72	.89	.86	.92	.56	.10	
.09	.55	.99	1.00	.64	.22	.20	0.00	.65	.89	.90	.96	1.00	.99	.99	.99	.98	.72	.20	
.67	.94	.99	.72	.87	.27	.12	.62	.95	.97	.98	.99	1.00	.97	.97	.92	.99	.99	.45	
.75	1.00	.74	.98	.81	.63	.76	.98	.90	.78	.97	.98	.94	.88	.65	.78	.97	.98	.45	
00	.86	1.00	.71	.37	.84	.63	.66	.61	.34	.59	.56	.41	.53	.40	.30	.29	.90	.66	
88	.73	.85	.25	0.00	.30	.35	.27	.21	.07	.37	.26	.08	.35	.16	.12	.30	.57	.84	
93	.97	.32	.36	0.00	.19	.11	0.00	.00	.13	0.00	0.00	.17	.01	0.00	.13	.11	.39	.68	
.83	.76	.40	.18	0.00	0.00	0.00	.04	0.00	0.00	0.00	0.00	0.00	.01	.24	.20	.64	.43	.99	
.13	1.00	.74	0.00	0.00	0.00	.09	.13	0.00	.01	0.00	0.00	0.00	0.00	.22	.45	.65	.25		
.28	1.00	.92	.19	0.00	0.00	0.00	0.00	0.00	0.00	0.00	0.00	0.00	0.00	.50	.78	1.00	.80	.97	
.03	.28	.88	.69	0.00	0.00	0.00	.11	.02	0.00	0.00	0.00	0.00	.55	.55	.99	.87	.76	0.00	
0.00	.13	.95	.97	.98	.13	.40	0.00	.14	.08	.07	0.00	.50	.51	.99	.83	.87	.09	0.00	
.11	0.00	0.00	.81	.83	.60	.85	.25	.26	.43	.32	.32	.47	.98	.65	.90	.04	.06	0.00	
.01	.13	.23	0.00	.02	.85	.65	.92	.75	.64	1.00	.61	.99	.56	.30	0.00	.00	.09	0.00	
.01	0.00	.07	.19	.16	.13	.73	.57	.99	.83	.97	.84	.50	0.00	0.00	0.00	0.00	.14	.18	

Figure II.10 Least squares (LESQ) reconstruction in digitized form.

$$\delta = .503 \quad v = .204$$
$$S = \mathbb{N}$$
$$B_{TVC} = 1$$
$$B_W = 4$$

$$\sigma_{k(\theta)}^2 = 0.1 \times N^2 k(\theta)$$

algorithms investigated is provided in Table II.1 . Included with the minimum δ values resulting from each algorithm is an estimate of the computer time per iteration. However, due to some time limit defaults, only estimates of the total computer time used was available. Thus these ranges of times that were encountered should only be considered relatively.

In the application to a two-phase system, one might be concerned with the density in a specific subchannel region, and the confidence one may have in the reconstruction to supply this. Figure II.11 attempts to consider this problem by using $\bar{\rho}$ calculated for all N by N regions in a reconstruction. This value is then compared to the known value from the model. The absolute value of this difference averaged over all regions is then plotted against the region size. The variance of this absolute difference from region to region is also plotted but on a log scale. An ART2 reconstruction ($\delta=0.23$) is employed in Fig. II.11 and although the results are not general, the observed trends are of interest.

The last PSEUDO tests were designed to evaluate the SMOOTH and FORCE techniques described in Sec. II.3 . Figure II.12 shows a plot of the discrepancy vs. the variance for five selected tests to examine their effectiveness. The dotted lines indicate the implementation of single steps while the solid lines are the true iteration courses. In all instances where SMOOTH was applied, it was applied twice in succession at the end of the iteration process. We recall also that a decrease in variance not only can mean a smoother reconstruction, but loss of detail as well! The result of applying

Table II.1 Efficiency comparison of major algorithms tested. $M=10, B_{INC}=1, B_W=4$ in all cases.

<u>Algorithm</u>	<u>Special conditions</u>	<u>δ_{\min} @ it'n no.</u>	<u>Est. total computer time / it'n, s.</u>
ART2	overlap but no differencing of ray sums	0.469@25	0.99-1.22
ART3	$B_{INC}=2$ $\epsilon = .005 \times N_{k(\theta)}$	0.699@15	1.32-1.97
ART2	storing array $k(i,j,M)$ henceforth	0.268@8	1.35-2.04
SIRT	add. or mult.	0.458@15	0.90-1.64
LESQ	$\sigma^2 = .0001 \times N_{k(\theta)}^2$	0.379@8	9.5-12.9

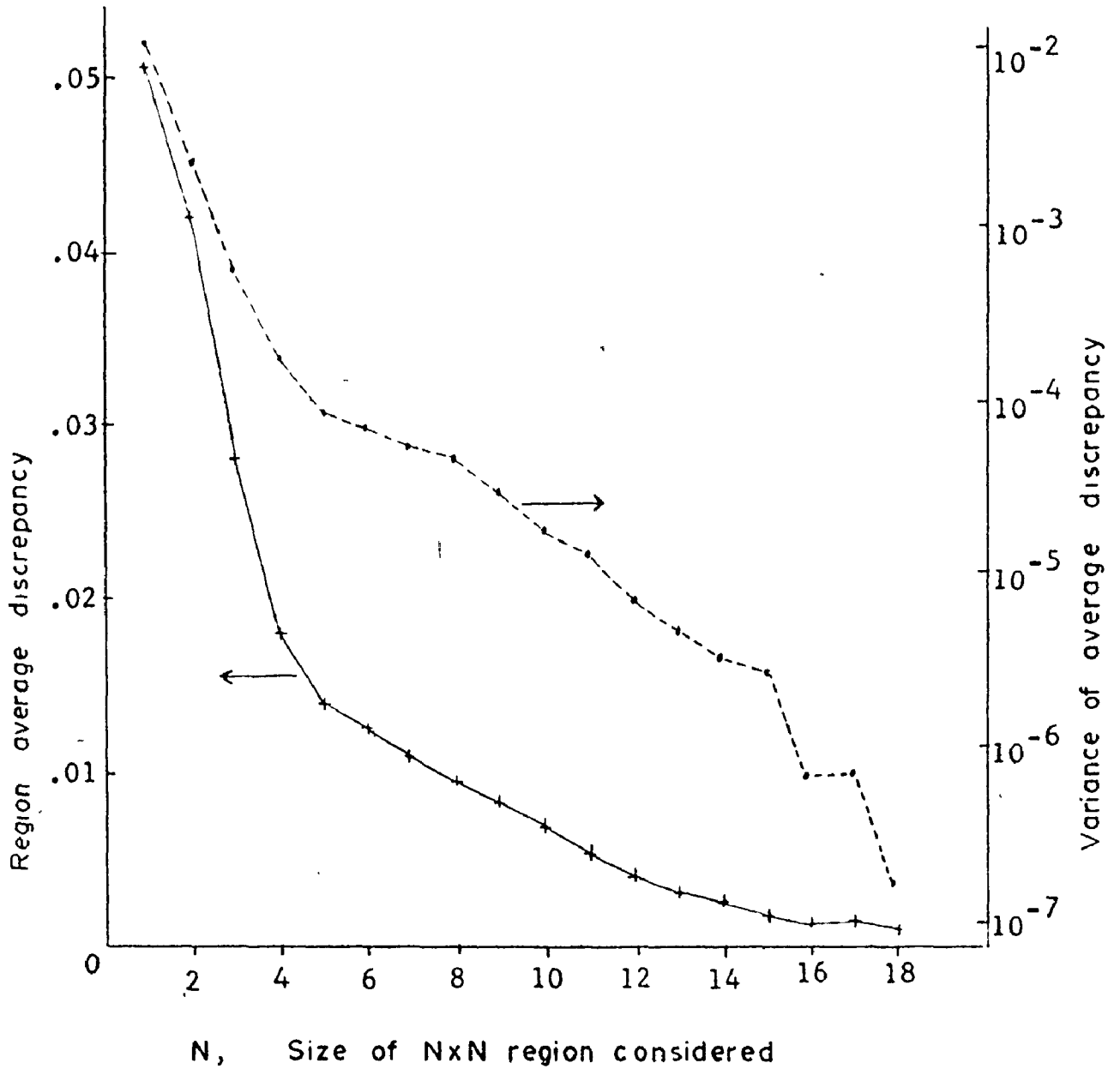


Figure II.11 Average and variance of discrepancy (absolute value) between reconstruction region of size (NxN) and digitized model. For ART2, $\delta=0.23$, reconstruction.

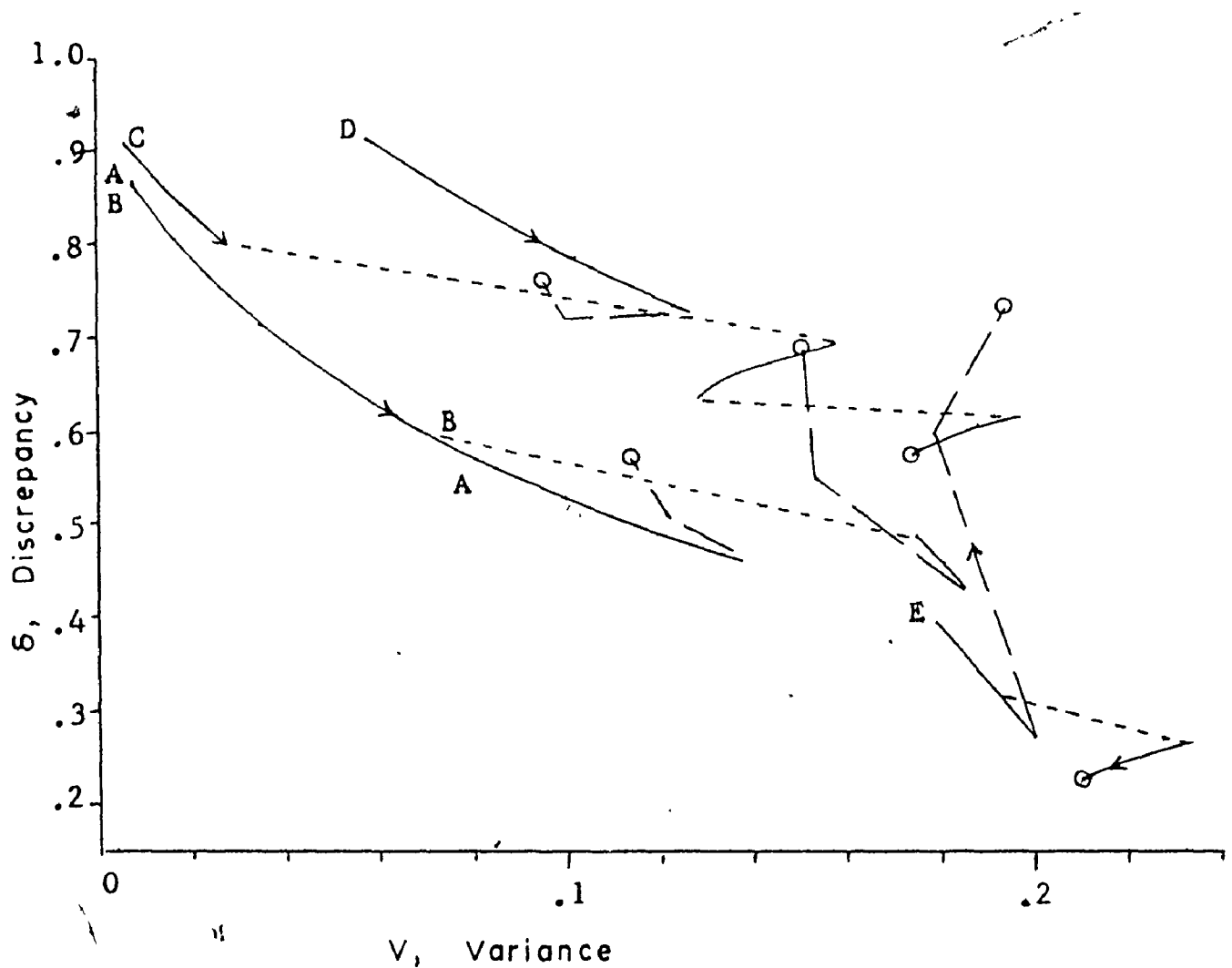


Fig. II.12 Effect of SMOOTH and FORCE on a discrepancy-variance plot.

—— course of iteration
 ——— SMOOTH step
 - - - - - FORCE step

- A. SIRT, $B_{INC}=1, B_W=4, M=10$
- B. Mult. SIRT, $B_{INC}=1, B_W=4, M=10$
- C. ART2, $B_{INC}=2.5, B_W=12.5, M=10$
- D. SIRT, $B_{INC}=2.5, B_W=12.5, M=15$
- E. ART2, $B_{INC}=1, B_W=4, M=10$

SMOOTH to a coarse increment SIRT reconstruction is illustrated in Figure II.13 . It can be observed in this figure, that while noise in the large regions is cleared up, it is at the expense of loss of fine detail. Visual evidence of the effectiveness of FORCE is found in Fig. II.14 which uses the same conditions as Fig. II.13 . Thus a direct comparison with the unaltered reconstruction process, Fig. II.13A, is possible.

We consider now the results of the REAL model tests. In the pre-run tests the removal cross-section for lucite with this apparatus was determined to be 4.08 cm^{-1} . In addition, it was found that the build-up data was almost linear when displayed on a semi-logarithmic plot. This led to the following representation by least squares fit

$$B(X) = 1.0 + \exp(-9.116 + 10.472 X - 3.882 X^2 + 0.679 X^3) , \quad (\text{II},21)$$

for X in the range 0.08 to 2.50 cm.

Prior to presenting the actual results for the REAL tests, the method used to compile the individual ray sums should be reviewed. For the PSEUDO tests, back substitution was suitable as in Gaussian elimination. The following forms are applicable for overlapping measurements with the beam width an integer multiple of the beam increment

$$S_k = T_k - \sum_{i=1}^{e_{o,r}} S_{k+i} , \quad (\text{II.22 a})$$

or

$$S_k = T_k - T_k + S_k . \quad (\text{II.22 b})$$

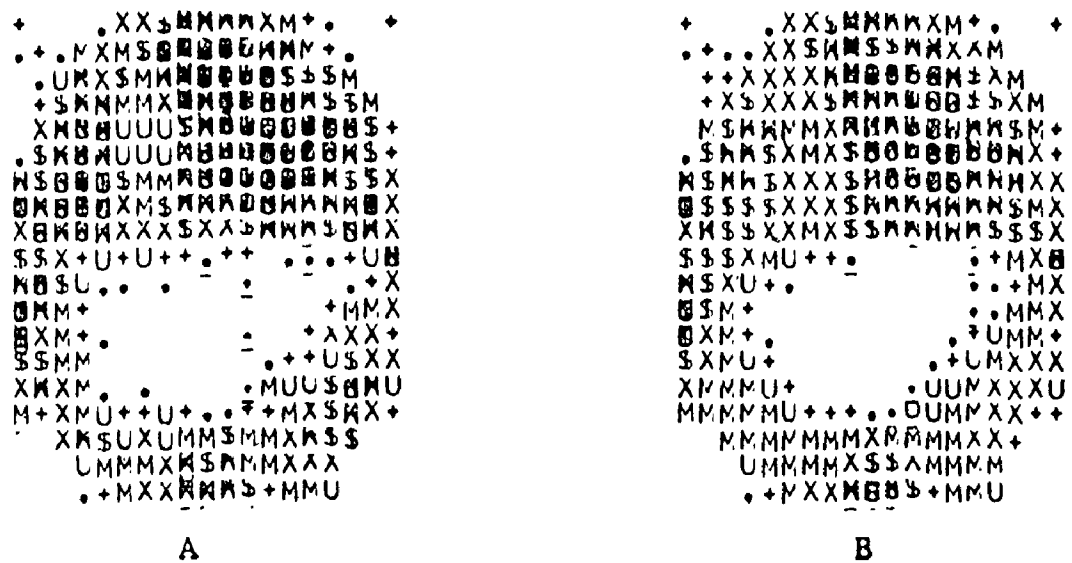


Figure II.13 Effect of SMOOTH on a coarse increment SIRT reconstruction ($B_{INC}=2.5$, $M=15$)

- A. unaltered reconstruction after 15 iterations
- B. reconstruction after SMOOTH applied twice

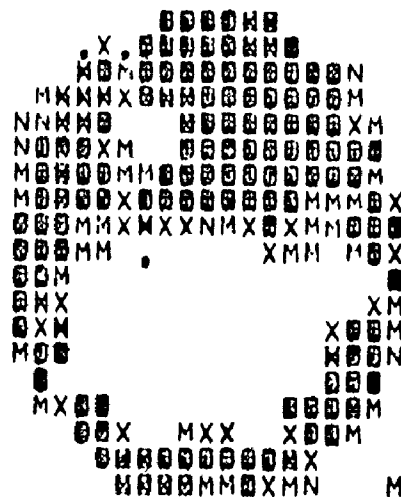


Figure II.14 Effect of FORCE on reconstruction of Fig. II.13A. FORCE technique applied at iterations 5 and 10 of the total 15 iterations used.

Alternatively, the form which incorporates all measurements contributing to S_k is

$$S_k = \frac{1}{B_R} \left[\sum_{i=k}^{k+B_{Dir}} T_i - \sum_{j=1}^{B_{Dir}} j(S_{k-B_R+j} + S_{k+B_R-j}) \right] \quad . \quad (II.23)$$

The PSEUDO program employed Eq. II.22a and the only error introduced in solving Eq. II.9 was computer round-off error. The result of applying Eq. II.22a to REAL data is shown in Figure II.15 which is a 40 x 40 ART2 reconstruction using coarse increment data ($B_{INC}=2.5$) for 15 projection angles. The effect of adding geometry constraints (Sec. II.3) to the same reconstruction is shown in part B of this figure. Figure II.16 is the SIRT reconstruction for identical conditions. A number of different methods to compute the individual ray sums for the real projection data were tried since direct substitution was found to yield negative density sums for some rays. Other methods include iterative application of Eqs. II.22 and II.23, use of relaxation parameters, and weighted least squares solution of the system. None of these yielded improvements over Fig. II.15 . Calculating the differences in the transmitted count rates was also tried. The result of this investigation is indicated in Fig. II.17 which again uses the ART2 algorithm. The result providing the best overall definition is shown in Fig. II.18 . For these ART reconstructions, the individual ray sums were calculated by direct substitution starting from opposite directions and overlapping the results. In Fig. II.18A, the overlap was near the middle of the reconstruc-

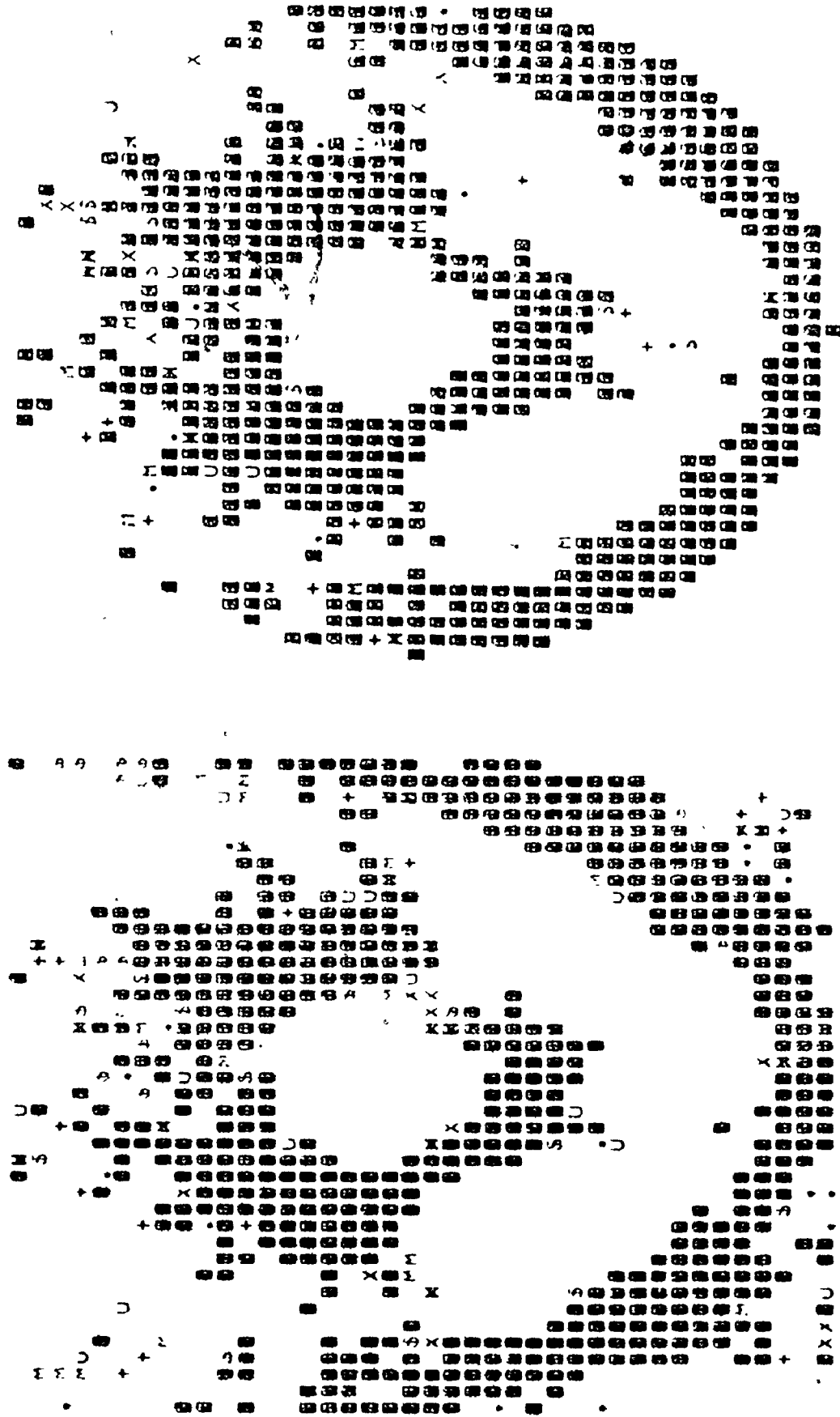


Figure II.15 ART2 reconstruction of REAL model. $B_{INC}=2.5$ $B_W=12.5$ $M=15$ $\Delta C=20.8$

A. without geometry constraints. $V=.243$ @ $IT=5$

B. with geometry constraints. $V=.237$ @ $IT=5$

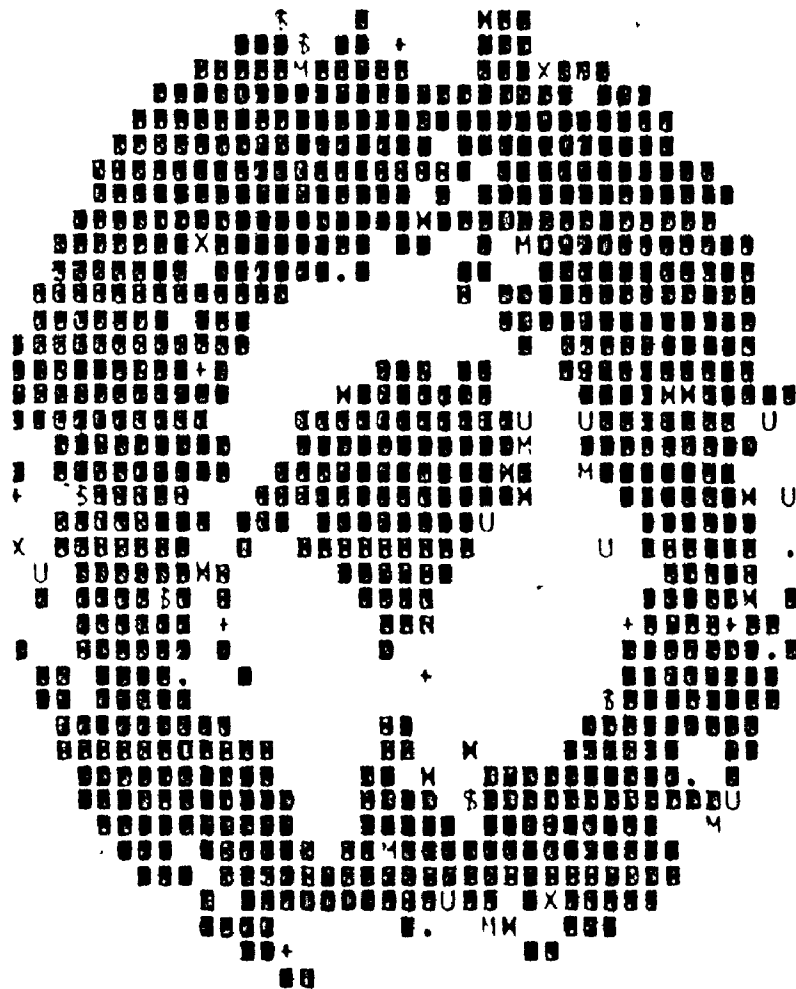


Figure II.17 ART2 reconstruction of REAL model using
transmitted count rate differencing to
determine ray sums. $V=.241$ @ $IT=5$
 $B_{INC}=2.5$ $B_W=12.5$ $M=15$ $\Delta T=20. s$

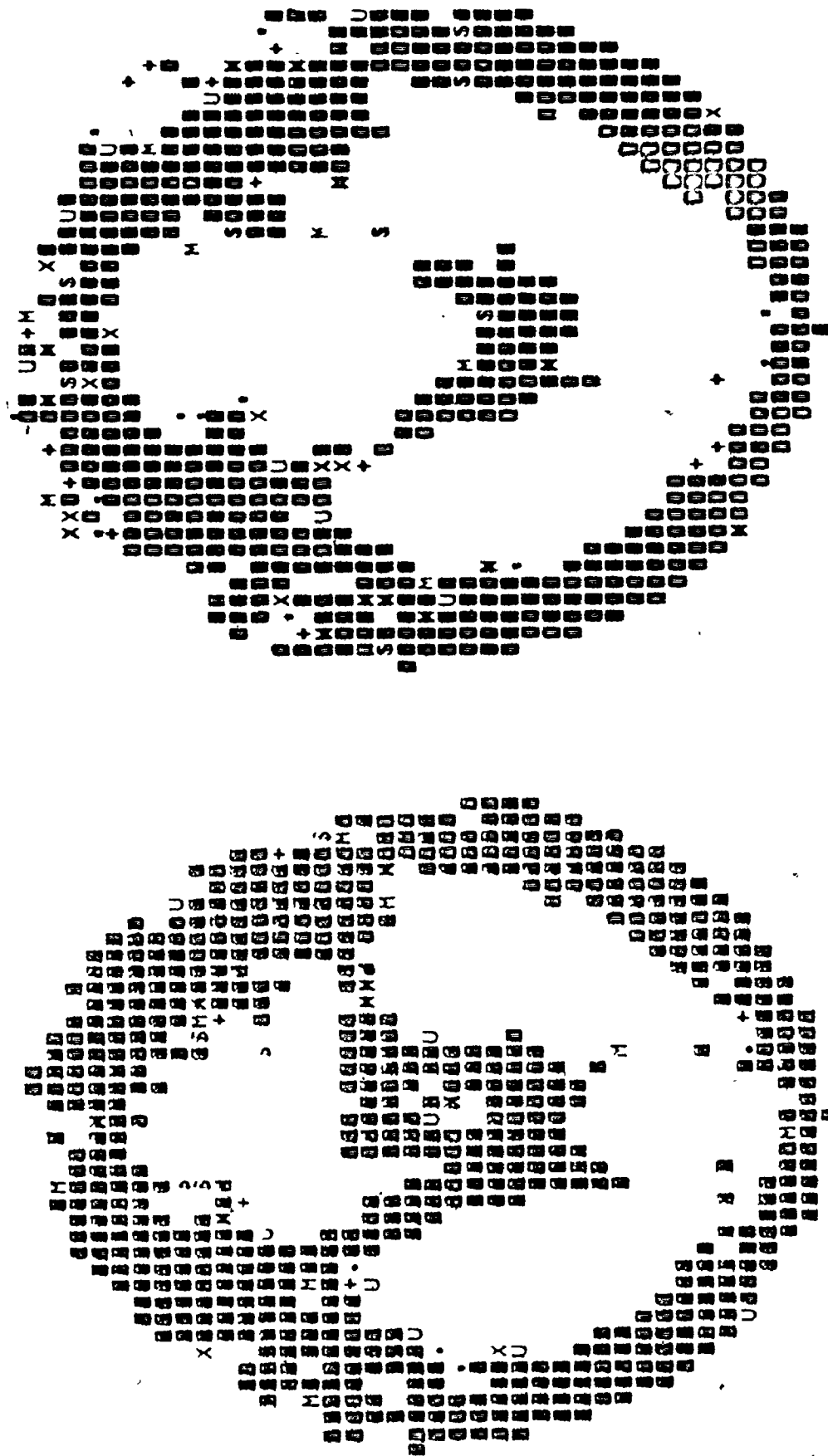


Figure II.18 ART2 reconstruction of REAL model using ray sums calculated by

back substitution from different directions. $BINC=2.5$ $BW=12.5$

$M=15$ $\Delta C=20. s$

A. overlapping at middle. $V=.252$ @ $IT=3$

B. overlapping $BPIF (=4)$ ray sums from top. $V=.282$ @ $IT=3$

tion, while for Fig. II.18B it was B_{DIF} ray sums ($=10$ u in this case) from the top. For the same algorithm and differencing procedure as Fig. II.18B, the second set of REAL data ($\Delta T=2.0$ s, $B_{INC}=1.25$) results in the reconstruction of Fig. II.19 . Implications of all these results are discussed in the next section.

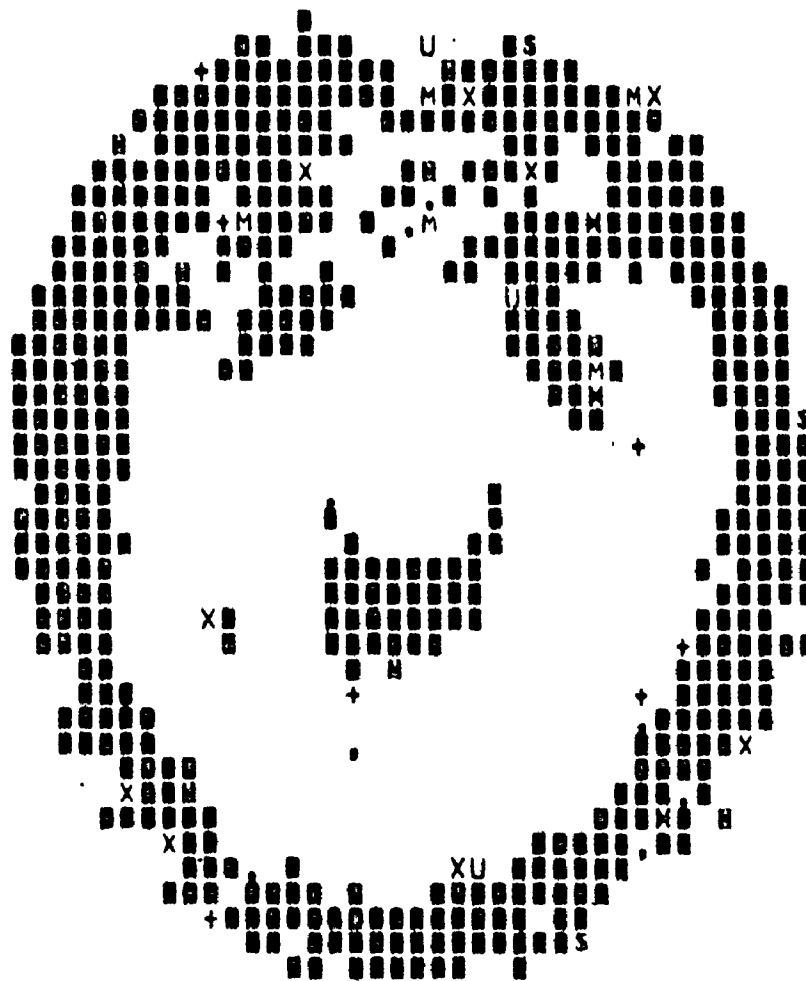


Figure II.19 ART2 reconstruction of REAL model with
smaller beam increment and gating period.

$B_{INC}=1.25$ $B_W=12.5$ $M=15$ $\Delta T=2.0$ s

$V=.243$ @ $IT=5$

II.7 DISCUSSION

II.7.1 General

Figure II.7 is a useful method of rapidly evaluating the various algorithms and conditions. This type of plot is identical to those found in the literature (Gordon et al, 1970) and shows similar trends. However, it should be remembered that the actual value of δ reported here and in Table II.1 is dependent on the complexity of the model used under given conditions. Curves A to D of Fig. II.7 provide a ready comparison of the effect of beam width. The curves however are all inferior to the cases where the overlapping ray sums are decoupled. The ART algorithm appears to easily give the best results on pseudo-projection data. This is exhibited in the reconstruction of Fig. II.8 as well as Fig. II.7. SIRT is not quite as effective and the results of LESQ, although better than SIRT, are disappointing for the effort required. From Table II.1, note that the iterative least squares algorithm can require 5 to 13 times the computer time compared to the others! A significant portion of this time was required to compute, d , the damping factor of Eq. II.18. A simpler formulization for d should be possible to reduce this time, even at the expense of requiring a greater number of iterations. Thus although not used again in this investigation, LESQ still merits future consideration since it is expected to be the algorithm least sensitive to noise in the input data.

The effect of the number of projections, M , is perhaps

best described in the literature. However, it appears from the current series of tests on both pseudo- and real-projection data that 5 or less projections may be considered hardly worth while. Compared to the 180 used in the EMI scanner, the 10 or 15 projections used here can surprisingly provide adequate results. A larger number of projection angles does not necessarily imply a corresponding improvement in the reconstruction since beyond a certain number, the improvement becomes marginal and may not be worth the extra effort. It seems that approximately $M = N/2$ would be a good first guess for the number of projections required to obtain an "adequate" reconstruction.

Figure II.11 is useful in obtaining a feel for how much confidence one should have in the reconstructions. It compares one of the better reconstructions, an ART2 with $\delta=0.23$, region by region with the digital model. In real circumstances of course, there is no model to compare against but the trends may be expected to be the same. As an example, consider each point individually, $N=1$. Fig. II.11 tells us that for this reconstruction we expect that on the average, $\bar{\rho}(i,j)$ can be considered accurate to within ± 0.05 . As we increase the size of the region considered, this discrepancy drops dramatically until about $N=4$ where the curve begins to level off. This result can provide guidance for the selection of the reconstruction mesh size. If a value of ρ is desired for a region of known size, then that region should be preferably 4 u or more in size. The relative price one pays for a coarser or finer

mesh is indicated in Fig. II.11 and must be weighed against the computer cost of reconstructing the N^2 points. The upper curve, with the ordinate scale on the right, is an estimate of the variation of the $\bar{\rho}$ discrepancy from region to region. Thus, for each point individually, $N=1$, the discrepancy can vary considerably from instance to instance. This curve falls even more rapidly and indicates that for larger region sizes, the expected average discrepancy is fairly uniform over the entire reconstruction. The behaviour of this curve at high N is due to the low number of degrees of freedom available.

Figure II.12 provides a means of evaluating the effect of the SMOOTH and FORCE techniques. In general, SMOOTH does increase the uniformity of the reconstruction. However, as seen in curve E, it can ruin a good reconstruction by smoothing over detailed features. This is to be expected in this case however, because some of the features are not large compared to the mesh size. Thus one of the main assumptions of SMOOTH was violated. Conversely the large internal void feature, as seen in Fig. II.13, is not adversely affected by SMOOTH. It may be concluded that although application of a technique such as SMOOTH increases ones confidence in individual ρ values, it is not to be recommended for highly detailed reconstructions. On the other hand, FORCE is a helpful step as indicated by the negative slope of the dotted lines in Fig. II.12. Its utility was also demonstrated in curve F of Fig. II.7 where in one FORCE step the same effect is achieved as six normal iterations. The visual effect as observed from Fig. II.14 is to clear up

the noise at low and high values while leaving intermediate values unchanged. In general, these results imply that the FORCE step should be used as follows:

1. in cases where ρ values near 0 or 1 are expected to be prevalent; however, when evaluating the success of the results just presented, it should be kept in mind that the digital model is largely 0 or 1 valued,
2. for coarse increment data to help clean up noise that may obscure features,
3. to save computer time for costly algorithms by reducing the number of iterations required to reach the same δ .

The real projection data tests appear much poorer in comparison. This is to be expected to some extent in accordance with the findings in the literature. However, even Fig. II.15 shows considerable detail. Considering the circular region near the centre of the reconstruction, its dimensions appear about 11 u wide by 12.5 u high. Since a 0.25 inch (0.635 cm) drill was used to form this feature, and 1 u = 0.02 inches according to the reconstruction scale, these values agree well with the known dimensions of 12.5 u by 12.5 u.

The real problem appears to be in the first few rays at the top of the reconstruction. This is in fact, the region where the substitutions of Eq. I.22 started, and thus the propagation of experimental error can not be the problem at this point. One possibility is our attempt to use void measurements

outside the known accurate range of neutron diagnosis (Harms et al, 1971). The problem may also be due to the initial analysis defining ρ or α from transmission data (Harms and Laratta, 1973), where a narrow beam is assumed and thus spatial effects due to beam area are not incorporated. Clearly, the edge of the object is the place where the non-uniformity across the beam width is most pronounced.

Also investigated was calculating differences in the transmitted count rate, although this would nullify the advantage gained by using a large beam. However the resulting reconstruction shown in Fig. II.17 is also unsatisfactory. This is due to the data being inconsistent beyond the noise present. A possible explanation for this inconsistency would be that the source strength was not uniform over the entire beam width. This should be checked prior to any investigation employing a subdivision of the beam and if true could be compensated for by using weighting factors in Eq. II.22 .

Fig. II.18A is the result of overlapping ray sums from the last half of the substitutions in opposite directions. The roughness at the edge of the object is now no longer a problem, however the middle of the reconstruction, where the overlap took place, is distorted. A similar effect is noted in Fig. II.18B at its overlap point. Thus, one should be wary of the overlap region when using this temporarily expedient method to compile ray sums.

The above discussion indicates the need for further work to determine a reliable and consistent method to solve a

II.7.2 Extension to the Dynamic Case

Although there remains room for further improvements, the reconstruction of a static voided system from neutron transmission data has been demonstrated. The only difficulties which may be encountered in applying these techniques to a dynamic two-phase flow situation are : 1) Validity of the steady-state assumption. This problem of maintaining steady conditions over the total measurement interval is common to many experimental techniques. It may be minimized however, if measurement techniques are used that record the data from a number of projections simultaneously. One very costly way that this could be accomplished, is in a polygonal array of opposing X-ray sources and sensing banks. 2) A significant bias may be introduced into the calculated void fraction when employing the constant void assumption over the total measurement interval τ . This error may be ascribed to the non-equality of

$$\frac{1}{\tau} \int_0^{\tau} e^{\lambda \alpha(t)} dt \neq e^{\frac{1}{\tau} \int_0^{\tau} \lambda \alpha(t) dt} , \quad (II.24)$$

or more compactly

$$\overline{e^{\lambda \alpha}} \neq e^{\lambda \bar{\alpha}} , \quad \text{where } \bar{\alpha} = \frac{1}{\tau} \int_0^{\tau} \alpha(t) dt .$$

In the past, the error has either been tolerated or minimized by a suitable choice of experimental conditions. However the fact that the bias is always positive (Harms and Forrest, 1971) suggests the possibility of its prediction as described below.

The general time-varying void fraction may be expressed as

$$\alpha(t) = \bar{\alpha} + \alpha' \quad , \quad (II.25)$$

where α' is the term incorporating all the time variations of α , for which the variance is given by

$$\overline{\alpha'^2} = \frac{1}{\mathcal{T}} \int_0^{\mathcal{T}} \alpha'^2 dt \quad , \quad (II.26)$$

where \mathcal{T} is the measurement interval. To describe the bias effects, Harms and Forrest (1971) have derived the following approximate relations retaining the first three terms of a series expansion. For the bias in transmission measurements

$$\frac{TR_{\alpha(t)}}{TR_{\alpha_r}} \simeq 1 + \lambda^2 \overline{\alpha'^2} \quad , \quad (II.27)$$

and for the void fraction bias

$$\Delta\alpha = \bar{\alpha}_r - \bar{\alpha} \simeq \frac{\lambda \overline{\alpha'^2}}{2} \quad , \quad (II.28)$$

where α_r is the void value determined when the static reference void assumption is employed and $\lambda(=\mu X)$ is known. Thus from Eq. II.27 it is possible to estimate the actual TR corresponding to the true time-averaged void fraction if Eq. II.26 can be evaluated. This variance, $\overline{\alpha'^2}$, can in fact be estimated using discrete time interval interrogation. If the total mea-

surement interval τ , is subdivided into N intervals $\Delta\tau$, then

$$\tau \approx N \cdot \Delta\tau \quad . \quad (II.29)$$

For example, instead of taking one 20-second measurement at each position, one should take 20 one-second measurements or 100 0.2-second measurements. Then the integral of Eq. II.26 can be given by

$$\int_0^{\tau} \alpha(t) dt \approx \sum_{i=1}^N \alpha_i \Delta\tau \quad . \quad (II.30)$$

Substitution Eq. II.25 into Eq. II.26 and applying Eqs. II.29 and II.30, the variance expression then becomes

$$\begin{aligned} \overline{\alpha'^2} &= \frac{1}{\tau} \int_0^{\tau} (\alpha(t) - \bar{\alpha})^2 dt \quad , \\ &\approx \frac{1}{N\Delta\tau} \sum_{i=1}^N (\alpha_i - \bar{\alpha})^2 \Delta\tau \quad , \\ &\approx \frac{1}{N-1} \sum_{i=1}^N (\alpha_i - \bar{\alpha})^2 \quad , \\ &= \sigma_{\alpha}^2 \quad , \end{aligned} \quad (II.31)$$

as given previously in Eq. I.3 . Thus if the approximations of Eqs. II.29 and II.30 are valid, the measured variance of N subintervals can be applied to compensating for the dynamic bias by correcting the measured TR. Once the bias is determined, the transmitted count rates over the N subintervals can be summed to yield $T\alpha$ for an effective gating interval of $N \cdot \Delta\tau$.

However, our bias prediction is only correct provided that the measured variance, σ_x^2 , is largely or entirely due to the temporal fluctuations of the voids. At low gating periods, ΔT , the source variance may make up a significant fraction of the total variance. In these cases, the variance due to other than void fluctuations must be subtracted out in order to predict the dynamic bias. This may be accomplished statistically according to the method of Barrett (1974) as described now.

It is first necessary to determine if the counting errors due to source statistics are significant. The criterion for negligible counting errors, adapted from Eq. 41 of Barrett, is

$$\Delta T \gg (e^{2\lambda(1-\alpha)})^{\frac{1}{2}} / \bar{T}_0 \quad , \quad (II.32)$$

where \bar{T}_0 is the expected reference count rate (s^{-1}) in the empty channel and $\lambda = \mu_{\text{medium}} X$. Selecting the minimum expected α and the maximum X possible will yield the limiting case. If Eq. II.32 is not satisfied, then the variance due to the statistical behaviour of the source must be predicted. Barrett (1974, Eq. 54) supplies us with the following expression

$$\sigma_x^2(\text{source stats.}) = \frac{1}{N} \sum_{n=1}^N \left(\frac{\sigma_{I_n}^2}{I_n} - \frac{2\sigma_{I_n}^2}{\bar{C}_n I_n} + \frac{\sigma_{C_n}^2}{\bar{C}_n} \right) + \frac{1}{N-1} \sum_{n=1}^N \frac{\sigma_{C_n}^2}{\bar{C}_n^2} \left[\ln\left(\frac{I_n}{\bar{C}_n}\right) - \frac{1}{N} \sum_{n=1}^N \ln\left(\frac{I_n}{\bar{C}_n}\right) \right] \quad , \quad (II.33)$$

where for the n^{th} measurement interval we have

\bar{C}_n = expected count rate for the system measurement,
= T_o

\bar{I}_n = expected source strength, = T_o/Q where Q accounts
for detector efficiency and wall attenuation.

If the statistical behaviour of the source is known or pre-determined by experiment, then the values of \bar{I}_n , \bar{C}_n , $\sigma_{I_n}^2$, $\sigma_{C_n}^2$, and $\sigma_{I_n C_n}^2$ may be predicted. Thus the result of Eq. II.33, when subtracted from the experimentally measured variance, gives the dynamic variance estimate we require for the bias prediction.

It can now be recognized that the importance of the void variance is common to both parts of the thesis. In the initial analysis, the effect of the gating period and the flow regime on the sample variance has been studied. Bearing these results in mind and incorporating the above analysis should lead to more reliable void measurements in two-phase flow systems.

II.8 CONCLUSION

Algebraic reconstruction methods have been proposed to ascertain the radial density distribution in a two-phase system. The methods considered can digitally reconstruct a two-dimensional image of a dual density object from projection measurements and thus overcome the 1-D limitation of previous investigations by radiation attenuation. Direct digital methods were selected over other reconstruction techniques primarily because of their greater flexibility which was exhibited throughout the investigation. Noisy input data, validity of the steady state assumption, and reliability of the void measurements were anticipated limitations but did not prove insurmountable.

In the first set of tests, the performance of the algorithms was investigated on pseudo-projection data from a digitized model. The algorithms were modified to an area basis so that beam widths greater than unity could be employed. It was found that beam widths significantly larger than the reconstruction mesh unit resulted in unsatisfactory reconstructions and that for our purposes, a practical range for the number of projection required is 5 to N , where N is the size of the reconstruction matrix. The overlapping of measurements and dissociation of individual ray sums was used in order to solve the problem of a fixed beam width too large for the required resolution. However, some additional work is indicated in interpreting overlapping real projection measurements before full

success can be claimed. Also, the addition of constraints due to known geometry and a FORCE step were found to improve the performance of the established reconstruction algorithms. A region by region comparison of the confidence in the average density value has resulted in a rough guideline for selecting the reconstruction mesh size in a given situation. Of all algorithms tested, ART2 consistently gave the most accurate reconstructions although LESQ and SIRT show promise for noisy data. Problems associated with the extension to the dynamic case were also considered. By subdividing the measurement period, it was found that the resulting void variance could be used to compensate for the dynamic bias effect arising from the fluctuations of the voids.

The fundamentals of computer science, radiation physics, and two-phase thermohydraulics underlying the current study indicate the need for a multidiscipline approach to explore the full potential of this subject. It is expected that the information arising from the successful reconstruction of a two-phase system in two or three dimensions will be useful in future void-reactivity models and subchannel codes. These techniques should not be limited only to two-phase flow situations, but may also be useful to 3-D radiography of solid objects. In summary, it has been demonstrated that when compared to conventional radiation scan studies, these methods should permit a modest increase in experimental effort to enhance substantially our understanding of internal two-phase conditions.

II.9 RECOMMENDATIONS

In light of what is now known, the following list indicates some possible directions for further progress and future applications.

1. There still remains the need to perfect the application to REAL data through re-evaluation of the neutron transmission method and/or performing experiments to evaluate the uniformity of the beam.
2. If more accurate reconstructions are required, the following ideas should be tried; i) calculating the area that the beam intercepts the matrix more accurately (see Sec. C of Appendix A.2), ii) calculate and apply weighting factors for each square, iii) use a variable size collimator to eliminate the "streaking" effect described by Herman et al (1973).
3. As an alternative to the methods discussed here, a slow continuous scan across the object might be employed as input for the Fourier transform method.
4. Rapidity of the ART algorithm indicates the possibility of on-line updating of CRT displayed images for time-varying conditions. This would become more viable, though more costly, if simultaneous ray measurements were taken from a number of different angles at the same time.
5. The methods are extensible to three dimensions by stacking

the planar representations. One area where 3-D effects are important is in the study of the Critical Heat Flux (CHF) phenomena. Film flow measurements have confirmed that CHF corresponds to a smooth approach to zero liquid film flow. This led Tong and Hewitt (1972) to conclude that an inventory of the integral entrainment and deposition effects causing saturated CHF was needed in CHF models. A knowledge of cross-sectional density patterns along the test channel should permit monitoring of the time-averaged conditions leading up to dryout and identification of the region(s) affected. It should at least provide an additional means of visualizing the occurrence of CHF in complicated geometries without the need of providing windows and correct illumination.

6. The future promises special purpose computers which will enable larger or more detailed systems to be reconstructed. However, there is still the need for more advanced algorithms that would make the most effective use of the data available. This is particularly important in medical X-ray applications.

NOTATION

Symbols

$A(i,j)$	reconstruction matrix of point values of ρ
$\tilde{A}(i,j)$	auxiliary estimator for $A(i,j)$
$B(x)$	representation of build-up equation
B_{DIF}	difference in B_W and B_{INC} in units of B_{INC} , $= (B_W - B_{INC}) / B_{INC} = B_R - 1$
B_{INC}	beam incremental distance, units of u
B_R	ratio of beam width to beam increment
B_W	beam width, units of u
d	damping factor in LESQ algorithm
k	ray number; $k=1, k_{max}(\theta)$
M	number of projections
$N_k(\theta)$	number of points in A belonging in the k^{th} ray at angle θ .
N	size of $N \times N$ reconstruction array. total number of measurements in interval \mathcal{T} .
$P_k(\theta)$	sum of ρ values from points in k^{th} ray, angle θ , from digitized model (pseudo-projection data)
$R_k^q(\theta)$	ray sum from the reconstruction matrix A at the q^{th} iteration
$S_k(\theta)$	ray sum of effective width B_{INC} calculated from $T_k(\theta)$
$T_k(\theta)$	experimentally determined ray sum of width B_W
$T\alpha$	transmitted count rate measured after passing through system, s^{-1}
T_0	reference count rate in empty channel or for completely voided condition, s^{-1}
TR	transmission ratio, $= T\alpha / T_0$

u	reconstruction grid unit
V	variance parameter, Eq. II.18
$X_k(\theta)$	effective linear distance that beam penetrates reconstruction matrix, units of u or cm as appropriate

Greek

α	void fraction, dimensionless
$\alpha(t)$	general time-varying void fraction
α_R	reference void calculated using static assumption
α'	term of $\alpha(t)$ incorporating all time variations with zero mean and variance α'^2
δ	discrepancy parameter, Eq. II.17
e	sensitivity parameter in ART3 algorithm
ρ	two-phase density parameter, = $1-\alpha$ in this study
μ	linear attenuation parameter, total cross-section, cm^{-1} thickness of liquid medium in units of mean free path, $= \mu X$
σ_k^2	variance of measured ray sum in LESQ algorithm
σ_α^2	void variance from experimentally determined probability density distribution
ΔT	gating period, s
τ	total measurement interval, s
θ	projection angle, degrees or radians

Superscripts

-	(overbar) time-averaged value
q	value at q^{th} iteration

ϕ

Subscripts

k	value for k^{th} ray
θ	value for projection angle θ

LITERATURE CITATIONS (Part II)

1. Barrett, P.R., "Systematic Errors in Discrete Time-Interval Transmission Method for the Estimation of Void Statistics in Boiling Channels", Nucl. Eng. Des., 30, 316 (1974).
2. Budinger, T.F., and Gullberg, G.T., "Three-Dimensional Reconstruction in Nuclear Medicine Emission Imaging", IEEE Trans. on Nucl. Sci., NS-21, 2 (1974).
3. Davis, M.R., "The Determination of Wall Friction for Vertical and Horizontal Two-Phase Bubbly Flows", J. Fluid Eng., P.174, June 1974.
4. Evangelisti, R., and Lupoli, P., "The Void Fraction in an Annular Channel at Atmospheric Pressure", Int. J. Heat Mass Transfer, 12, 699 (1969).
5. Garland, W.J., "Void-Reactivity Effects in Neutron Multiplying Media", Ph.D. dissertation, Dept. Chem. Eng., McMaster Univ., Hamilton, Ont., Oct. 1975.
6. Gilbert, P., "Iterative Methods for Three Dimensional Reconstruction of an Object from Projections", J. Theor. Biol., 36, 105 (1972).
7. Goiten, M., "Three-Dimensional Density Reconstruction from a Series of Two-Dimensional Projections", Nucl. Instr. Meth., 101, 509 (1972).
8. Gordon, R., et al, "Algebraic Reconstruction Techniques (ART) for Three-Dimensional Electron Microscopy and X-ray Photography", J. Theor. Biol., 29, 471 (1970).
9. Gordon, R., "A Tutorial on ART", IEEE Trans. on Nucl. Sci., NS-21, 78 (1974).
10. Gordon, R., and Herman, G.T., "Three-dimensional Reconstruction from Projections : A Review of Algorithms", Int. Rev. Cytology, 38, 111 (1974).
11. Gordon, R., et al, "Image Reconstruction from Projections", Scientific American, P.56, Oct. 1975.

12. Harms, A. A., et al, "Measurement of Time-Averaged Voids by Neutron Diagnosis", J. Appl. Phys., 42, #10, 4080 (1971).
13. Harms, A. A., and Forrest, C. F., "Dynamic Effects in Radiation Diagnosis of Fluctuating Voids", Nucl. Sci. Eng., 46, 408 (1971).
14. Harms, A. A., and Laratta, F., "The Dynamic Bias in Radiation Interrogation of Two-Phase Flow", Int. J. Heat Mass Transfer, 16, 1459 (1973).
15. Herman, G. T., et al, "ART: Mathematics and Applications", J. Theor. Biol., 42, 1 (1973).
16. Kjaerheim, G., "Heat Transfer a Limiting Factor in Water Cooled Nuclear Reactors", Nucl. Eng. Des., 21, 279 (1972).
17. Lahey, R. T., and Schraub, F. A., "Mixing, Flow Regimes and Void Fraction for Two-Phase Flow in Rod Bundles", Two-Phase Flow and Heat Transfer in Rod Bundles, Winter Ann. Meeting, ASME, Los Angeles, Calif., P. 1, Nov. 18, 1969.
18. Tong, L. S., and Hewitt, G. F., "Overall Viewpoint of Flow Boiling CHF Mechanisms", ASME Heat Transfer Conference, Paper No. 72-HT-54, Denver, Colo., Aug. 1972.
19. Zielke, L. A., et al, "Bundle Subchannel Void Fraction by Gamma Scattering", ANS Winter Ann. Meeting, New Orleans, Louisiana, 21, 412 (1975).
20. Zuber, N., and Findlay, J. A. "Average Volumetric Concentrations in Two-Phase Flow Systems", J. Heat Transfer, Nov. 1965.

PART II
APPENDICES

- A.1 Photographs of REAL test model and positioning stand.
- A.2 Description of program listings.
- A.3 Main programs.
- A.4 Additional program segments.
- A.5 Subroutines.

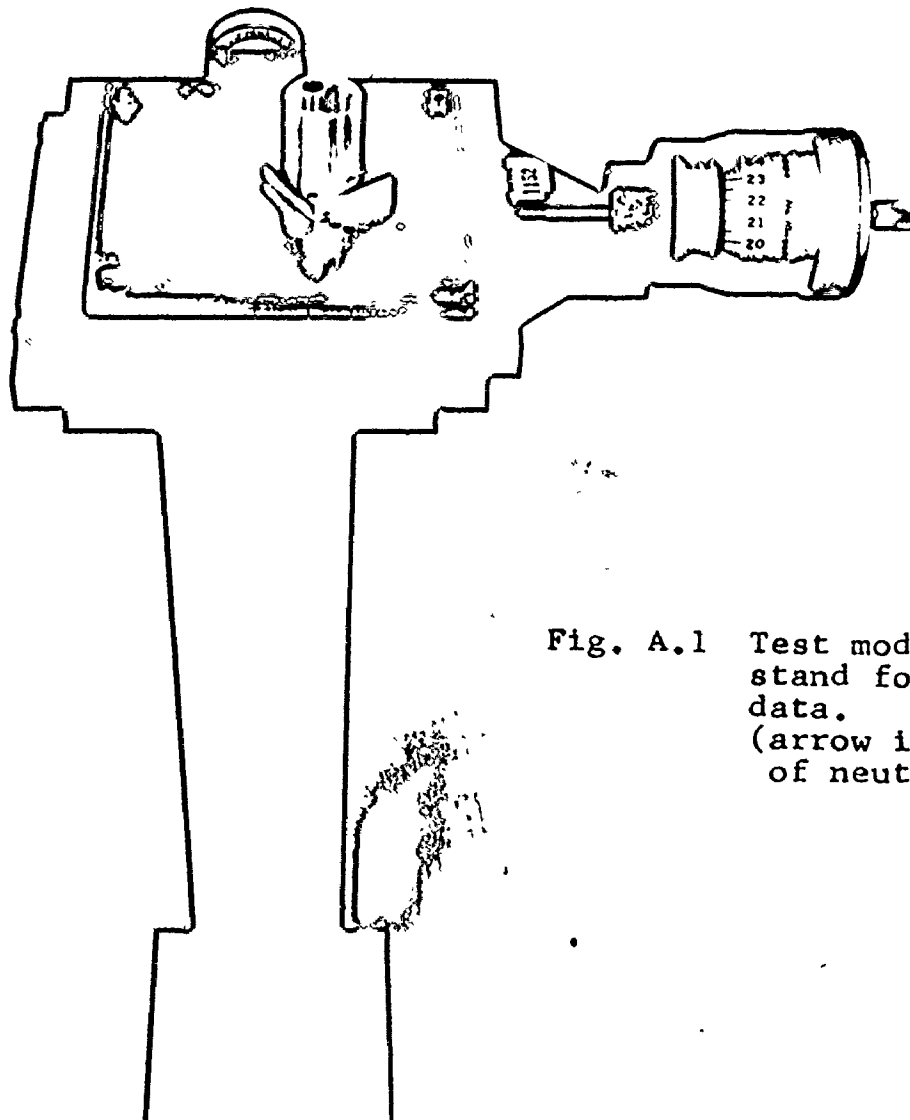
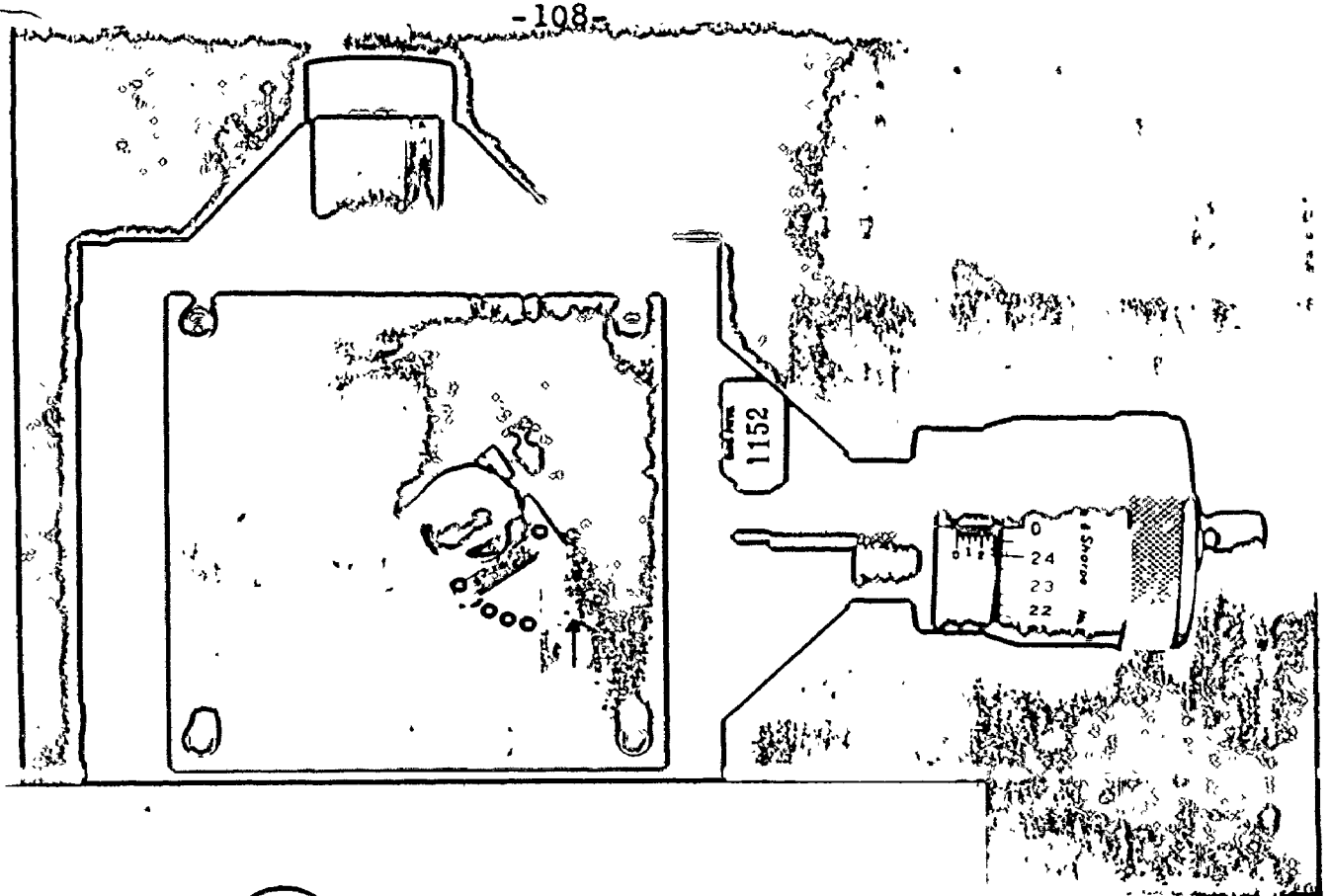


Fig. A.1 Test model and positioning stand for real projection data.
(arrow indicates direction of neutron current)

A.2 DESCRIPTION OF PROGRAM LISTINGS

A.2.1 Program Variables

Much of the notation employed in the text is carried into the programs. Where the similarity is not obvious, the following list will relate program variables with ones used in the text. Refer to NOTATION for definitions.

Text	Program
$B(x)$	BUILD(X) (function subroutine)
$N_k(\theta)$	NKT(K,M)
$P_k(\theta)$	SUMT(K,M)
q	IT
$R_k^q(\theta)$	SUMAT(K,M)
$S_k(\theta)$	SUMRT(K,M)
$T_k(\theta)$	TR(K,M) only in subroutine RAYSUM
$T\alpha$	TA
V	VAR
δ	DELTA
ρ	RHO
μ	SIGMA (I know it's really mu!)
$\sigma_k^2(\theta)$	SPE
θ	THETA

A.2.2 Program Segment Description

To clarify the layout of the programs and permit easy interchange of algorithms, the programs have been divided alphabetically into nine blocks or segments. The general function

of each segment is common to both the PSEUDO and REAL programs and is described below. Features distinctive to each program are explained further.

A - PROGRAM DESCRIPTION, variable definitions, dimension statements.

PSEUDO- N=19 in this case. XL is not required but is approximated by NKT here. Equivalence statements are used to save time in DO loops.

REAL - N=40 in this case. Dimension statements SUM1, SUM2, etc are needed only for SIRT. Array AA is not needed for SIRT.

B - READ IN INITIAL DATA. Define matrix size, beam increment and beam width and read in projection angles.

PSEUDO- Array T is the digitized model. $1-T$ was performed to obtain ρ values instead of α (See Fig. II.3). AVG and D2 are constants that were determined from earlier runs. $D2 = \sum_i \sum_j (T(i,j) - \text{AVG})^2$ and is used in segment G. Initialize the reconstruction matrix to the average at this point.

REAL - Input raw count rates, TA, and compute transmission ratios, TR.

C - GEOMETRY SECTION. Defines the ray positions on the reconstruction matrix. In these programs, required values are stored in arrays for later use in the algorithms. However, because of the rapidity of these calculations, the values may be computed as required in the algorithm and not stored.

This would save a considerable amount of memory space at the expense of more computation time.

PSEUDO- SUMT is the model ray sums. KX stores the ray value for each co-ordinate. It should be eliminated by direct computation as mentioned above if memory space is not available. However, since KX, NKT, and X are fixed for a given matrix size and projection angles, they can be computed only once and stored. This is useful if many runs under identical conditions are to be performed.

REAL - X is the area of each ray and is calculated crudely here from NK (the no. of points). LC corrects for points on the edge of the matrix since $\frac{1}{2}$ of their area lies outside the object. A more accurate determination of X (from geometry) is recommended.

D - CALC. INDIVIDUAL RAY SUMS (array SUMRT) from computed or measured ray sums of width B_w .

PSEUDO- Calculated by direct back substitution starting at ray KMAX.

REAL - Computed by subroutine RAYSUM (See I)

E - UPDATE RECONSTRUCTION RAY SUMS (array SUMAT)

REAL - Initialize matrix to AVG using ray sums from first projection.

F - ALGORITHMS

PSEUDO- Uses the fully constrained additive ART2 algorithm in this case.

REAL - Uses the additive SIRT algorithm. The sums over all angles are stored for convenience in this version. This may be circumvented in more space efficient versions. Note that geometry constraints (object has radius of 20 units) are applied at this point.

A.4.1 - Lists the unique portions of the LESQ algorithm for pseudo-projection data. Dimension statements are excessive in this version. A more efficient implementation (saving both time and memory) should be possible.

A.4.2 - Lists the additive SIRT algorithm for program PSEUDO.

A.4.3 - Lists the fully constrained additive ART2 algorithm for use in program REAL.

A.4.4 - Simply illustrates an example of how the FORCE technique might be employed (within the framework of SIRT in this case). It is assumed here that all values of the matrix were initially set to 0.5. The FORCE step is applied only once at IT #5.

G - EVALUATE PROGRESS, use variance as criteria to terminate iterations. The first iteration is used to accumulate the ray sums and it is not until IT=2 that the effective $B_W=B_{INC}$ and the algorithms are implemented.

PSEUDO- DELTA and VAR are the δ and V parameters described in the text. EUCL is the "Euclidean distance" of Gordon, et al (1970). DMAX represents the

maximum difference between model and reconstruction of all points.

REAL - Since T matrix is unknown only variance may be determined.

H - OUTPUT RESULTS. Output the entire NxN matrix point by point and/or use subroutine PIX (See I).

I - SUBROUTINES

ALPHA - Called to convert transmission ratio measurements to density parameter RHO. This subroutine is simply a slightly altered version of the one used in Part I of this thesis.

BUILD - A polynomial function by least squares fit to represent the build-up factor in lucite.

RAYSUM- Used in REAL to determine individual ray sums (SUMRT) of width B_{INC} from experimental data. The array TR is now used to store the experimental ray sums (width B_W). This particular subroutine uses back substitution from both directions and overlaps the results at L. It is one example of many attempts used (others include weighted least squares and transmission data differencing).

A.5.1 - This form of overprinting routine PIX is dimensioned for PSEUDO but is easily altered for REAL. Uses ten gray-level code of Fig. II.5.

A.5.2 - Implementation of subroutine SMOOTH averages ρ values over consistent regions (See Sec. II.3). Again can be readily altered for use in REAL.

A.3 MAIN PROGRAMS

A.3.1 Listing of PSEUDO Program (for pseudo-projection data)

```

PROGRAM TST (INPUT,TAPE5=INPUT,OUTPUT,TAPE6=OUTPUT,PUNCH,
7 TAPE7=PUNCH,TAPE1)
*****
ALGEBRAIC RECONSTRUCTION TECHNIQUES APPLIED TO IDEALIZED
TWO PHASE FLOW PROBLEM.
*****
A(I,J)= MATRIX OF POINT VALUES OF 2 PHASE DENSITY.
      = 1. - TIME AVERAGED VOID FRACTION.
T(I,J)= MODEL 2 PHASE ARRAY USED IN PLACE OF EXPTL. DATA.
N=      SIZE OF N X N DIGITIZED MATRIX
NKT=    NO. OF POINTS IN K TH RAY FOR ANGLE THETA
THETA(M)=ARRAY OF MP PROJECTION ANGLES,ADS(90 DEG.) MAX
IT=     ITERATION NUMBER.
BINC=   INCREMENTAL DISTANCE THE BEAM IS MOVED EACH TIME.
BW=     BEAM WIDTH USED EACH TIME, UNITS OF SPACING MESH.
XL=     LENGTH OF KTH RAY.
*****
DIMENSION A(19,19),AA(19,19),T(19,19),THETA(30),RAD(30)
2,VAR(50),KMAX(30),KX(19,19),NKT(35,15),KXE(361),
3SUMRT(35,15),SUMAT(35,15),SUMT(35,15)
DIMENSION EA(361),ET(361),EAA(361)
EQUIVALENCE (EA,A),(ET,T),(EAA,AA),(KXE,KX)
COMMON /AREA2/ A,N
REWIND 1
READ *,N,MP
PRINT *,N,MP
N2=N*N
DO 1 I=1,MP
  READ *,THETA(I)
1 RAD(I)=THETA(I)/57.29578
  PRINT *,(THETA(I),I=1,MP)
  AVG=.464265928
C READ IN DIGITIZED MODEL.
  DO 7 JJ=1,N
    J=N-JJ+1
    DO 7 I=1,N
      READ*,T(I,J)
7 T(I,J)=1.-T(I,J)
    DO 2 I=1,N2
      EA(I)=EAA(I)=AVG
2 D2=87.92903
C THE BEAM WIDTH MUST BE AN INTEGER MULTIPLE OF THE INCREMENT.
  BINC=1.
  BW=4.
  IBDIF=BW/BINC-1
  PRINT*,BW,BINC,IBDIF
  IT=1
12 M=1
11 K=1
  TN=TAN(RAD(M))
  CS=COS(RAD(M))
9 NKT(K,M)=0
  IF(IT.GT.1) GO TO 25.
  SUMRT(K,M)=0.0
  SUMT(K,M)=0.0

```

```

25  CONTINUE
C  CALCULATE MAX AND MIN VALUES OF J IN THE KTH RAY.
   JMAX=YTOP=1.+((K-1)*BINC+BW)/CS
   IF(YTOP.EQ.FLOAT(JMAX)) JMAX=JMAX-1
   IF(JMAX.GT.N) JMAX=N
   JMIN=YBOT=(N-1)*TN+1.+((K-1)*BINC/CS
   IF(THETA(M).GT.0.0) JMIN=YBOT=((1-N)*TN+1.+((K-1)*BINC/CS
   IF(JMIN.LT.1) JMIN=1
   IF(JMIN.GE.N) JMIN=N
   DO 3 J=JMIN,JMAX,1
   FOR EACH VALUE OF J IN KTH RAY, CALC. MIN AND MAX VALUES OF I.
   IF(PAD(M).GT.0.0) GO TO 4
   IMAX=XTOP=(J-1)/TN+1.-(((K-1)*BINC+BW)/CS)/TN
   IMIN=XBOT=(J-1)/TN+1.-((K-1)*BINC/CS)/TN
   IF(FLOAT(IMIN).NE.XBOT) IMIN=XBOT+1.
   IF(XTOP.EQ.FLOAT(IMAX)) IMAX = IMAX- 1
   GO TO 5
4  IMAX=(J-1)/TN+N-(((K-1)*BINC)/CS)/TN
5  IMIN=XTOP=(J-1)/TN+N-((K-1)*BINC+BW)/CS/TN+1.
   IF(IMAX.GT.N) IMAX=N
   IF(IMAX.LT.1) IMAX=1
   IF(IMIN.LT.1) IMIN=1
   IF(IMIN.GT.N) IMIN=N
   DO 6 I=IMIN,IMAX,1
   IF(IT.GE.2) GO TO 28
   SUMT(K,M)=SUMT(K,M)+T(I,J)
   THE POINT (I,J) IN THE ANGLE M, IS IN THE KX RAY.
28  KX(I,J)=K
   NKT(K,M)=NKT(K,M)+1
6  CONTINUE
3  CONTINUE
   IF(NKT(K,M).LE.1) GO TO 8

   K=K+1
   GO TO 3
8  CONTINUE
   KMAX(M)=K
   IF(IT.EQ.2) WRITE(1) KX
   IF(M.GE.MP) GO TO 10
   M=M+1
   GO TO 11
10  CONTINUE
   IF(IT.GT.1) GO TO 23

C  THE FOLLOWING PORTION CALCS. RAY SUMS OF EFFECTIVE WIDTH
C  = BINC, BY USING DIFFERENCES IN OBSERVED SUMS.
   DO 20 M=1,MP
   K20=KMAX(M)
   DO 20 K=1,K20
   KM=KMAX(M)-K+1
   SUMLES=0.0
   DO 22 LX=1,IBDIF
   IF( (KM+LX).GT.KMAX(M) ) SUMRT ((KM+LX),M)=0.0
22  SUMLES=SUMLES+SUMRT((KM+LX),M)
20  SUMRT(KM,M)=SUMT(KM,M)-SUMLES

23  CONTINUE
   IF(IT.EQ.1) GO TO 17

C  UPDATE THE RAY SUMS.
   REWIND 1
   DO 27 M=1,MP
   READ(1) KX
   K6=KMAX(M)
   DO 29 K5=1,K6
29  SUMAT(K5,M)=0.0
   DO 26 I=1,N2
   K=KXE(I)
   SUMAT(K,M)=SUMAT(K,M)+EA(I)
26  CONTINUE

```

```

C   PERFORM THE ART2 ALGORITHM FROM STORED ARPAYS.
DO 24 J=1,N
DO 24 I=1,N
K=KX(I,J)
AA(I,J)=AA(I,J)+(SUMRT(K,M)-SUMAT(K,M))/NKT(K,M)
A(I,J)=AA(I,J)
IF(AA(I,J).GT.1.0) A(I,J)=1.0
IF(AA(I,J).LT.0.0) A(I,J)=0.0
24 CONTINUE
27 CONTINUE
F

C   LETS SEE HOW WELL WERE DOING AFTER EACH ITERATION.
O1=O3=DMAX=0.0
OO 55 I=1,N2
O3=O3+(EA(I)-AVG)**2
O4=ABS(ET(I)-EA(I))
O1=O1+O4**2
IF(O4.GT.DMAX) DMAX=O4
55 CONTINUE
DELTA=(O1/O2)**.5
EUCL=(O1/N**2)**.5
VAR(IT)=O3/N**2
WRITE(6,63) IT,DELTA,EUCL,VAR(IT),DMAX
IF(IT.LE.2) GO TO 17
IF(ABS(VAR(IT)-VAR(IT-1)).LT.(VAR(IT-1)/100.)) GO TO 13
17 IF(IT.GE.15) GO TO 13
IT=IT+1
IF(IT.GT.2) GO TO 23
BW=BINC
GO TO 12
G

13 WRITE(6,60) IT
DO 30 JJ=1,N
J=N-JJ+1
WRITE(6,61) (A(I,J),I=1,N)
30 CONTINUE
CALL PIX
60 FORMAT(1H1,20X,*MATRIX AFTER*,I3,* ITERATIONS*///)
61 FORMAT(1H ,5X,19F5.2,/)
63 FORMAT(1H ,I10,3F20.8,F10.4)
99 STOP
END
H

```

Initial output:

3.188 CP SECONDS COMPILATION TIME
4.718 CP SECONDS EXECUTION TIME

19 10
-80. -60. -40. -20. -2. 10. 25. 45. 70. 88.
4. 1. 3

2
3
4
5
6
7
8
9

.41425535	.20444697	.18073736	.7344
.34387404	.16971176	.18610001	.7453
.31582631	.15586940	.19099516	.7593
.29826728	.14720351	.19442793	.7580
.28483236	.14057299	.19738277	.7469
.27404590	.13524955	.19988041	.7329
.26541614	.13099052	.20191921	.7191
.25851756	.12758587	.20355398	.7062

A.3.2 Listing of REAL Program (for real projection data)

```

PROGRAM TST (INPUT,TAPE5=INPUT,OUTPUT,TAPE6=OUTPUT,PUNCH,
7 TAPE7=PUNCH,TAPE1)

*****
TWO DIMENSIONAL IMAGE RECONSTRUCTION BY ALGEBRAIC METHODS.
      GARY ZAKATB                      FALL 1975.
THIS PROGRAM DETERMINES THE TWO PHASE DENSITY DISTRIBUTION
FROM TRANSMISSION MEASUREMENTS OF A STATIC MODEL TAKEN AT A
NUMBER OF DIFFERENT PROJECTION ANGLES.

AA(I,J) =AUXILLARY ESTIMATOR.
N=      SIZE OF N X N DIGITIZED MATRIX
NKT=    NO. OF POINTS IN K TH RAY FOR ANGLE THETA
THETA(M)=ARRAY OF MP PROJECTION ANGLES.
A(I,J)= MATRIX OF POINT VALUES OF 2 PHASE DENSITY.
      = 1. - TIME AVERAGED VOID FRACTION.
      (0.0.LT. ABS(THETA) .LT. (90.0 DEG.))
IT=     ITERATION NUMBER.
BINC=   INCREMENTAL DISTANCE THE BEAM IS MOVED EACH TIME.
BW=     BEAM WIDTH USED EACH TIME, UNITS OF SPACING MESH.
TC,TA=  REFERENCE AND INPUT TRANSMITTANCE READINGS.
X(K,M)= EFFECTIVE LENGTH OF KTH RAY AT ANGLE M.
SUMAT=  EFFECTIVE RAY SUM'S OF WIDTH = BINC.
SUMAT=  CORRESP. RAY SUM OF RECONSTRN.
*****

DIMENSION A(40,40),AA(40,40),THETA(30),RAD(30),VAR(50),
1 KMAX(15),KX(40,40),NKT(65,15),SUMRT(65,15),
2 SUMAT(65,15),EA(1600),KXE(1600),X(65,15),EAA(1600),
4 TA(65),TF(65,15),TQ(15)
DIMENSION SUM1(40,40),SUM2(40,40),SUM3(40,40),SUM4(40,40)
EQUIVALENCE (EA,A),(EAA,AA),(KXE,KX)
COMMON MP,IBR,BW,IBDIF,KMAX,TR,X,SUMRT
REWIND 1
READ *,N,MP
PRINT *,I,MP
N2=N*N
THE BEAM WIDTH MUST BE AN INTEGER MULTIPLE OF THE INCREMENT.
BINC=1.25
BW=12.5
IBR=BW/BINC
IBDIF=IBR-1
PRINT*, BW,BINC,IBDIF
C READ IN MEASUREMENT ANGLES USED AND MAX. NO. OF RAYS AT EACH.
DO 1 I=1,MP
  READ*, THETA(I)
  RAD(I)=THETA(I)/57.29578
  1 KMAX(I)=IFIX((N-1)/BINC*(SIN(ABS(RAD(I)))+COS(RAD(I)))) +2
  PRINT*, (THETA(I),I=1,MP)
  PRINT*, (KMAX(I),I=1,MP)
  READ*, (TC(M),M=1,MP)
  DO 14 M=1,MP
    KPLUS=KMAX(I)+IBDIF
    READ*, (TA(I),I=1,KPLUS)
    DO 14 K=1,KPLUS
      TR(K,M)=TA(K)/TC(M)
    14
  C THIS PORTION OF THE PROGRAM DETERMINES THE RAY POSITIONS.
  IT=1
  12 M=1
  11 K=1
  TH=TAN(RAD(M))
  CS=COS(RAD(M))
  9 NK=LC=0

```

```

C      CALCULATE MAX AND MIN VALUES OF J IN THE KTH RAY.
      JMAX=YTOP=1.+((K-1)*BINC+BW)/CS
      IF(YTOP.EQ.FLOAT(JMAX))JMAX=JMAX-1
      IF(JMAX.GT.N)JMAX=N
      JMIN=YBOT=(N-1)*TN+1.+ (K-1)*BINC/CS
      IF(THETA(M).GT.2.0)JMIN=YBOT=(1-N)*TN+1.+ (K-1)*BINC/CS
      IF(JMIN.LT.1)JMIN=1
      IF(JMIN.GE.N)JMIN=N
      DO 6 J=JMIN,JMAX,1
C      FOR EACH VALUE OF J IN KTH RAY, CALC. MIN AND MAX VALUES OF I.
      IF(PAD(M).GT.0.3)GO TO 4
      IMAX=XTOP=(J-1)/TN+1.-(((K-1)*BINC+BW)/CS)/TN
      IMIN=XBOT=(J-1)/TN+1.-((K-1)*BINC/CS)/TN
      IF(FLOAT(IMIN).NE.XBOT)IMIN=XBOT+1.
      IF(XTOP.EQ.FLOAT(IMAX))IMAX=IMAX-1
      GO TO 5
4      IMAX=(J-1)/TN+N-(((K-1)*BINC)/CS)/TN
      IMIN=XTOP=(J-1)/TN+N-((K-1)*BINC+BW)/CS/TN+1.
5      IF(IMAX.GT.N)IMAX=N
      IF(IMAX.LT.1)IMAX=1
      IF(IMIN.LT.1)IMIN=1
      IF(IMIN.GT.N)IMIN=N
      DO 6 I=IMIN,IMAX,1
      NK=NK+1
      IF(I.EQ.1.OR.I.EQ.N.OR.J.EQ.1.OR.J.EQ.N)LC=LC+1
      KX(I,J)=K
6      CONTINUE
      X(K,M)=K/BW-LC/(BW*2)
      IF(IT.EQ.2)NKT(K,M)=NK
      IF(NK.LE.1)GO TO 8
      K=K+1
      GO TO 9
C
C
8      CONTINUE
      KMAX(M)=K
C      THE ARRAY KX(I,J) DESCRIBES WHICH RAY EACH POINT IS IN.
      IF(IT.EQ.2)WRITE(1) KX
      IF(M.GE.MP)GO TO 10
      N=N+1
      GO TO 11
10     CONTINUE
C
C
      IF(IT.GT.2)GO TO 3
      CALL RAYSUM(IT)
      IF(IT.EQ.1)GO TO 3
C      CALC. AVG 2 PHASE DENSITY FOR MODEL FROM FIRST PROJ. DATA.
      KM=KMAX(1)
      SUMAV=0.
      DO 31 K=1,KM
31     SUMAV=SUMAV+SUMRT(K,1)/X(K,1)/BW
      AVG=SUMAV/KM
      PRINT*,AVG
C      INITIALIZE MATRIX TO AVG.
      DO 2 I=1,N2
2      EA(I)=EAA(I)=AVG
C
3      CONTINUE
      IF(IT.EQ.1)GO TO 17
C
C      CALCULATE THE LATEST RAY SUMS.
      REWIND1
      DO 40 M=1,MP
      KE=KMAX(M)
      DO 40 K=1,KE
40     SUMAT(K,M)=0.0
      DO 41 M=1,MP
      READ(1) KX
      DO 41 I=1,N2
      K=KX(I)
      SUMAT(K,M)=SUMAT(K,M)+EA(I)
41     CONTINUE
C

```



```

C      INTRODUCE THE SIRT ALGORITHM.
DO 76 I=1,N
DO 76 J=1,N
SUM1(I,J)=SUM2(I,J)=SUM3(I,J)=SUM4(I,J)=0.0
76 CONTINUE
REWIND1
DO 70 M=1,MP
PEAK(1) KX
DO 70 I=1,N
DO 70 J=1,N
K=KX(I,J)
SUM1(I,J)=SUM1(I,J)+SUMRT(K,N)
SUM2(I,J)=SUM2(I,J)+SUMAT(K,N)
SUM3(I,J)=SUM3(I,J)+X(K,M)*B
70 SUM4(I,J)=SUM4(I,J)+NKT(K,M)
DO 71 I=1,N
DO 71 J=1,N
A(I,J)=A(I,J)+(SUM1(I,J)/SUM4(I,J)-SUM2(I,J)/SUM3(I,J))
IF(A(I,J).LE.0.0) A(I,J)=0.0
C      ADD CONSTRAINTS OF KNOWN GEOMETRY.
IF(((I-21)**2+(J-21)**2).GT.400) A(I,J)=0.0
71 CONTINUE
C      TO EVALUATE PROGRESS, COMPUTE VARIANCE AFTER EACH ITERATION.
D1=0.0
DO 55 I=1,N2
55 D1=D1+(EA(I)-AVG)**2
VAR(IT)=D1/N2
PRINT*,IT,VAR(IT)
IF(IT.LE.2) GO TO 17
IF(ABS(VAR(IT)-VAR(IT-1)).LT.(VAR(IT-1)/100.)) GO TO 13
17 IF(IT.GE.15) GO TO 13
IT=IT+1
IF(IT.GT.2) GO TO 3.
BW=9INC
GO TO 12

C      OUTPUT RESULTS.
13 WRITE(6,60)
DO 30 JJ=1,N
J=N-JJ+1
WRITE(6,61) (A(I,J),I=1,N)
30 CONTINUE
IF(VAR(IT).GE.0.05) CALL PIX
60 FORMAT(1H1,25X,*RESULTANT MATRIX IN DIGITIZED FORM*,//)
61 FORMAT(1H,5X,40F3.1,//)
99 STOP
END

```

```

C      SUBROUTINE ALPHA (X,TR,RHO)
C      THIS SUBROUTINE CONVERTS THE TRANSMITTANCE RATIO,TR, TO
C      THE TWO PHASE DENSITY PARAMETER (=1- VOID FFACTION, A).
C      INPUT PARAMETERS ALSO REQUIRED =
C      -EFFECTIVE LINEAR THICKNESS, X, IN CM.
C      -TRANSMITTANCE RATIO, TR=TA/T0
IF(TR.GT.0.99999) GO TO 2
SIGMA=4.075
IF( TR.LE.(BUILD(X)*EXP(-SIGMA*X))) GO TO 4
N=1
A=A2=0.0
1  XA=X*(1.0-A)
F=TP-BUILD(XA)*EXP(-SIGMA*XA)
IF(ABS(F).LE.0.00005) GO TO 6
IF (F) 5,6,7
7  A2=A
GO TO 8
5  N=N+1
8  A=A2+ 1.0/10.**N
GO TO 1
6  CONTINUE
RHO=1.-A
GO TO 3
2  RHO=0.0
GO TO 3
4  RHO=1.0
3  RETURN

```

FUNCTION BU1D(X)

```

BU1D=EXP(-9.1162+10.4715*X-3.8921*X**2+.67355*X**3)+1.0
IF(X.LT. 0.16) BU1D=1.0
RETURN
END

```

SUBROUTINE RAYSUM(IT)

THIS SUBROUTINE COMPUTES RAYSUMS OF WIDTH RING, FROM EXPTL. RAYSUMS OF WIDTH BW.

```

DIMENSION KMAX(15),TR(65,15),X(65,15),SUMRT(65,15)
DIMENSION S(65)
COMMON MP,IBR,94,IBDIF,KMAX,TR,X,SUMRT
IF(IT.EQ.2) GO TO 1
DO 15 M=1,MP
  KM=KMAX(M)
  DO 15 K=1,KM
    CALL ALPHA(X(K,M)*.0508,TR(K+IBDIF,M),RHO)
15  TR(K+IBDIF,M)=RHO*X(K,M)*BW
    GO TO 2
1  CONTINUE
  DO 3 M=1,MP
    X1=0.0
    DO 3 K=1,IBDIF
      X1=X1+X(K,M)/IBR
      CALL ALPHA((X1*.0508),TR(K,M),RHO)
3  TR(K,M)=X1*BW*RHO
401 CONTINUE

```

ALL RAY SUMS OF WIDTH BW ARE NOW STORED IN ARRAY TR.

```

DO 4 M=1,MP
  KPLUS=KMAX(M)+IBDIF
  KHALF=KPLUS/2
  IST=IBR
  IEN=KPLUS
C  IST AND IEN ARE 1ST NON-ZERO RAY SUMS IN BOTH DIRECTIONS.
DO 120 I=1,KHALF
  J=KPLUS-I+1
  IF(TR(I,M).LE.0.0) IST=I+IBR
120 IF(TR(J,M).LE.0.0) IEN=J-1
DO 60 K=1,65
  SET ENTIRE SUMRT ARRAY TO ZERO.
60 SUMRT(K,M)=S(K)=0.0
DO 18 K=IST,IEN
  SUM=0.
DO 23 L=1,IBDIF
  SUM=SUM+S(K-L)
  S(K)=TR(K-IBDIF,M)-SUM
18 CONTINUE
DO 19 KM=IST,IEN
  K=IEN-KM+IST
  SUM=0.
DO 24 L=1,IBDIF
  SUM=SUM+SUMRT(K+L,M)
  SUMRT(K,M)=TR(K,M)-SUM
19 CONTINUE

```

OVERLAP THE BACK SUBSTITUTED RAY SUMS AT L.

```

L=IEN-IBDIF
DO 20 K=L,IEN
  SUMRT(K,M)=S(K)
  KM=KMAX(M)
DO 28 I=1,KM
  SUMRT(I,M)=SUMRT(I+IBDIF,M)
  PRINT*,M
  PRINT*,(SUMRT(K,M),K=1,KM)
4  CONTINUE
2  RETURN
END

```

40 15
-4. -16. -28. -40. -52. -64. -76. -88.5 79.5 67.4 55.3 43. 31.5 19.5 7.5

A.4 ADDITIONAL PROGRAM SEGMENTS

A.4.1 Listing of LESQ Algorithm (for pseudo-projection data)

```

DIMENSION A(50,50), T(50,50), THETA(30), RAD(30)
2, VAR(50), KMAX(50), KX(20,20,10), NKT(50,50),
3, SUMRT(50,50), SUMAT(50,50), SUMT(50,50)
COMMON /AREA/ KX, SUMRT, SUMAT, MP, N
C   SPE= EXPERIMENTAL PURE ERROR VARIANCE.
C   UPDATE THE RAY SUMS.
DO 26 M=1, MP
  K8=KMAX(M)
DO 29 K=1, K8
  SUMAT(K,M)=0.0
DO 26 I=1, N
DO 26 J=1, N
  K=KX(I,J,M)
  SUMAT(K,M)=SUMAT(K,M)+A(I,J)
26 CONTINUE
C   CALC. THE DAMPING FACTOR, D.
  SUM3=SUM4=0.0
DO 105 M=1, MP
  K8=KMAX(M)
DO 105 K=1, K8
  SPE=.0001*NKT(K,M)**2
  SUM3=SUM3+(SUMRT(K,M)-SUMAT(K,M))*DNASUM(K,M)/SPE
105 SUM4=SUM4+(DNASUM(K,M))**2/SPE
  D=SUM3/SUM4
C   PERFORM THE LEAST SQUARES ITERATIVE PROCEDURE.
DO 150 I=1, N
DO 150 J=1, N
  A(I,J)=A(I,J)+D*DNA(I,J)
  IF(A(I,J).GT.1.0) A(I,J)=1.0
  IF(A(I,J).LT.0.0) A(I,J)=0.0
150 CONTINUE

FUNCTION DNA(I,J)
  DIMENSION KX(20,20,10), SUMRT(50,50), SUMAT(50,50)
2, NKT(50,50)
COMMON /AREA/ KX, SUMRT, SUMAT, MP, N
  SUM1=SUM2=0.0
DO 102 M=1, MP
  K=KX(I,J,M)
  SPE=.0001*NKT(K,M)**2
  SUM1=SUM1+(SUMRT(K,M)-SUMAT(K,M))/SPE
102 SUM2=SUM2+1./SPE
  DNA=SUM1/SUM2
  RETURN
END

FUNCTION DNASUM(K,M)
  DIMENSION KX(20,20,10), SUMRT(50,50), SUMAT(50,50)
2, II(50), JJ(50)
3, NKT(50,50)
COMMON /AREA/ KX, SUMRT, SUMAT, MP, N
  NK=0
DO 45 J1=1, N
DO 45 I1=1, N
  IF(KX(I1,J1,M).EQ.K) GO TO 44
  GO TO 45
44 NK=NK+1
  II(NK)=I1
  JJ(NK)=J1
45 CONTINUE
  DNASUM=0.0
DO 104 L=1, NK
104 DNASUM=DNASUM+DNA(II(L),JJ(L))
  RETURN
END

```

A.4.2 Listing of SIRT Algorithm (for pseudo-projection data)

```

C      CALCULATE THE LATEST RAY SUMS.
DO 26 M=1,MP
KM=KMAX(M)
DO 29 K=1,KM
29  SUMAT(K,M)=0.0
DO 26 I=1,N
DO 26 J=1,N
K=KX(I,J,M)
26  SUMAT(K,M)=SUMAT(K,M)+A(I,J)
C
C      INTRODUCE THE ADDITIVE SIRT ALGORITHM.
DO 71 I=1,N
DO 71 J=1,N
SUM1=SUM2=SUM3=0.0
DO 70 M=1,MP
K=KX(I,J,M)
SUM1=SUM1+SUMRT(K,M)
SUM2=SUM2+SUMAT(K,M)
70  SUM3=SUM3+NKT(K,M)
A(I,J)=A(I,J)+(SUM1-SUM2)/SUM3
IF(A(I,J).LT.0.0) A(I,J)=0.0
71  CONTINUE

```

A.4.3 Listing of ART2 Algorithm (for real projection data)

```

C      UPDATE THE RAY SUMS.
REWIND 1
DO 27 M=1,MP
REAC(1)KX
K6=KMAX(M)
DO 29 K5=1,K6
29  SUMAT(K5,M)=0.0
DO 26 I=1,N2
K=KXE(I)
SUMAT(K,M)=SUMAT(K,M)+EA(I)
26  CCNTINUE
C      PERFORM THE ART2 ALGORITHM FROM STORED ARRAYS.
DO 24 J=1,N
DO 24 I=1,N
K=KX(I,J)
AA(I,J)=AA(I,J)+SUMRT(K,M)/(X(K,M)*BW) -SUMAT(K,M)/NKT(K,M)
A(I,J)=AA(I,J)
IF(AA(I,J).LT.0.0) A(I,J)=0.0
IF(AA(I,J).GT.1.0) A(I,J)=1.0
C      ACC CONSTRAINT OF KNOWN GEOMETRY.
IF(((I-21)**2+(J-21)**2).GT.400) A(I,J)=0.0
24  CONTINUE
27  CONTINUE

```

A.4.4 Application of FORCE Technique (at iteration No.5)

```

DO 71 I=1,N
DO 71 J=1,N
A(I,J)=A(I,J)+(SUM1(I,J)-SUM2(I,J))/SUM3(I,J)
IF(A(I,J).LE.0.0) A(I,J)=0.0
IF(IT.NE.5) GO TO 71
IF(A(I,J).LE.0.4) A(I,J)=0.0
IF(A(I,J).GE.0.6) A(I,J)=1.0
71  CONTINUE

```

A.5 SUBROUTINES

A.5.1 Listing of Subroutine PIX

```

SUBROUTINE PIX
  DIMENSION A(19,19) ,IP(10,19),IPA(19)
  COMMON /AREA2/ A,N
  WRITE(6,60)
  DO 1 J1=1,N
  JJ=N-J1+1
  DO 2 II=1,N
  IF(A(II,JJ).GT.0.9)IPA(II)=10
  IF(A(II,JJ).LE.0.1)IPA(II)=1
  IF(A(II,JJ).LE.0.1 .OR. A(II,JJ).GT.0.9) GO TO 2
  IF(A(II,JJ).GT.0.1.AND.A(II,JJ).LE.0.2)IPA(II)=2
  IF(A(II,JJ).GT.0.2.AND.A(II,JJ).LE.0.3)IPA(II)=3
  IF(A(II,JJ).GT.0.3.AND.A(II,JJ).LE.0.4)IPA(II)=4
  IF(A(II,JJ).GT.0.4.AND.A(II,JJ).LE.0.5)IPA(II)=5
  IF(A(II,JJ).GT.0.5.AND.A(II,JJ).LE.0.6)IPA(II)=6
  IF(A(II,JJ).GT.0.6.AND.A(II,JJ).LE.0.7)IPA(II)=7
  IF(A(II,JJ).GT.0.7.AND.A(II,JJ).LE.0.8)IPA(II)=8
  IF(A(II,JJ).GT.0.8.AND.A(II,JJ).LE.0.9)IPA(II)=9
2  CONTINUE
  DO 9 I=1,10
  DO 9 J=1,N
9  IP(I,J)=1H
  DO 19 I=1,N
  IF(IPA(I).EQ.1) GO TO 19
  IF(IPA(I).GE.10)IP(10,I)=1HI
  IF(IPA(I).GE.9)IP(9,I)=1HO
  IF(IPA(I).GE.8)IP(8,I)=1HH
  IF(IPA(I).EQ.7)IP(7,I)=1H$
  IF(IPA(I).EQ.6 .OR. IPA(I).GE.8)IP(6,I)=1HX
  IF(IPA(I).EQ.5)IP(5,I)=1HM
  IF(IPA(I).EQ.4)IP(4,I)=1HU
  IF(IPA(I).EQ.3)IP(3,I)=1H+
  IF(IPA(I).EQ.2)IP(2,I)=1H.
19 CONTINUE
  DO 29 I=1,10
  WRITE(6,61)(IP(I,J),J=1,N)
29 CONTINUE
  WRITE(6,64)
  CONTINUE
  WRITE(6,65)
  FORMAT(1H1,/,41X,*RESULTANT MATRIX IN PICTORIAL FORM*,////////)
  FORMAT(1H+,40X,19(A1))
  FORMAT(1H)
  FORMAT(1H,8(//))
  RETURN
END

```

I,
H

A.5.2 Listing of Subroutine SMOOTH

```

C      SUBROUTINE SMOOTH (K3)
        REGION AVERAGING SUBPROGRAM.
        REAL MAX,Q(10),DEV(10),T(19,19),A(19,19)
        COMMON A,N,T,AVR
        DO 39 IY=1,K3
          NM1=N-1
          DO 37 J=2,NM1
            DO 37 I=2,NM1
              IF(A(I,J).EQ.0.0 .OR. A(I,J).EQ.1.0) GO TO 37
              IM1=I-1
              IP1=I+1
              JM1=J-1
              JP1=J+1
              IC=1
              DO 30 IZ=IM1,IP1
                DO 30 JZ=JM1,JP1
                  Q(IC)=A(IZ,JZ)
30             IC=IC+1
                DO 35 IX=1,4
                  SUM=0.0
                  DO 38 IC=1,9
                    SUM=SUM+Q(IC)
38             IF(IX.GT.1) GO TO 36
                  AVG=SUM/9.
                  DO 31 IC=1,9
                    DEV(IC)=ABS(Q(IC)-AVG)
36             MAX=DEV(1)
                  DO 32 IC=2,9
                    IF(IC.EQ.5) GO TO 32
                    IF(DEV(IC).GT.MAX) MAX=DEV(IC)
32             CONTINUE
                  DO 33 IC=1,9
                    IF(MAX.EQ.DEV(IC)) GO TO 34
                    GO TO 33
34             SUM=SUM-Q(IC)
                  Q(IC)=0.0
                  DEV(IC)=0.0
33             CONTINUE
35             CONTINUE
                  A(I,J)=SUM/5.
                  IF(A(I,J).LT. 0.01) A(I,J)=0.0
                  IF(A(I,J).GT. 0.99) A(I,J)=1.0
37             CONTINUE
          WRITE(5,69) IY,((A(L,M),L=1,N),M=1,N)
C      LETS SEE HOW WELL WERE DOING AFTER EACH ITERATION.
          D1=D2=D3=0.0
          DO 55 L=1,N
            DO 55 M=1,N
              D1=D1+(T(L,M)-A(L,M))**2
              D2=D2+(T(L,M)-AVR)**2
              D3=D3+(A(L,M)-AVR)**2
          55 CONTINUE
          DELTA=(D1/D2)**.5
          EUCL=(D1/N**2)**.5
          VAP=D3/4**2
          WRITE(5,53) IY,DELTA,EUCL,VAR
          CALL PIX
          39 CONTINUE
          63 FORMAT(1H ,I10,3F20.8)
          59 FORMAT(1H1,2CX,*REGION SMOOTHED MATRIX BY COMPUTER,*,I3,
            2 * TIMES*,///, 19(5X,19F5.2//))
          99 RETURN
        END

```